

AN ABSTRACT OF THE THESIS OF

Andrew John Cihonski for the degree of Master of Science in
Mechanical Engineering presented on October 15, 2010.

Title: Investigation of volumetric coupling effects on particle-laden
turbulent flows at dilute to moderate loadings

Abstract approved: _____

Sourabh V. Apte

Particle-laden turbulent flows are of great importance in many industrial applications and are sufficiently complex to require multiple methods of study to provide a better understanding of the dominant physical mechanisms present in these processes. This work on large-eddy simulation of particle-laden flows seeks to help provide the building blocks for larger scale models to be used in design scale analysis of industrial processes such as oxy-coal combustion power plants. Presented in this work are a series of studies related to real world particle-laden turbulent flows of practical importance, such as a particle-laden slot nozzle jet and a particle-laden channel flow at various mass loadings. The features of the particle-laden turbulent channel flow and an in depth analysis of the effects of accounting for the finite-volume of the particles is presented. Finite-volume effects are analyzed for changes in turbulent statistics as well as particle

structuring. General agreement with previously published results is found and expounded upon.

©Copyright by Andrew John Cihonski
October 15, 2010
All Rights Reserved

Investigation of volumetric coupling effects on particle-laden
turbulent flows at dilute to moderate loadings

by

Andrew John Cihonski

A THESIS

submitted to

Oregon State University

in partial fulfillment of
the requirements for the
degree of

Master of Science

Presented October 15, 2010

Commencement June 2011

Master of Science thesis of Andrew John Cihonski presented on October 15, 2010.

APPROVED:

Major Professor, representing Mechanical Engineering

Head of the School of Mechanical, Industrial and Manufacturing Engineering

Dean of the Graduate School

I understand that my thesis will become part of the permanent collection of Oregon State University libraries. My signature below authorizes release of my thesis to any reader upon request.

Andrew John Cihonski, Author

ACKNOWLEDGEMENTS

The author would like to thank the National Energy Technology Laboratory (contract number 41817M4077) for project guidance and funding for this work. Dr. Sourabh Apte for his help and guidance in promoting a positive learning environment and many hours spent working together since my arrival at Oregon State University. Also, I would like to thank the thermal fluid sciences group and, in particular, the colleagues I have had the pleasure of sharing an office with since coming to Oregon State: Ehsan Shams, Mathieu Martin, Justin Finn, Daniel Peterson and Benn Eilers. I would also like to thank my parents for always being so supportive, regardless of how much sense my plans ever really make.

TABLE OF CONTENTS

	<u>Page</u>
1 Introduction	2
2 Literature review	7
2.1 Modeling Methods	8
2.2 Flow Regimes and Coupling Methods	12
2.2.1 One-Way Coupling	13
2.2.2 Two-Way Coupling	14
2.2.3 Four-Way Coupling	15
2.2.4 Volumetric Coupling	16
2.3 Effects of Varying Particle Size	18
2.4 Particle Clustering in Turbulence	22
2.5 Direct Numerical Simulation and Large Eddy Simulation	24
2.6 Outline of Present Work	25
3 Mathematical Formulation	28
4 Particle-laden Slot Nozzle Jet	37
5 Preliminary Test Cases Using Volumetric Coupling	45
5.1 Bubble-Vortex Interaction	48
5.2 Jet Fluidization	50
5.3 Slurry Flow	54
5.4 Rayleigh-Taylor Instability	56
5.5 Gravitational Settling	57
6 Particle-laden Channel Flow	60
6.1 Problem Description and Setup	61
6.2 Validation of Work	63
6.3 Forcing Method	68
6.4 Mass Loading	73
6.5 Statistics	77

TABLE OF CONTENTS (Continued)

	<u>Page</u>
6.6 Near Wall Structures	84
6.7 Channel Centerline Particle Structures	91
6.8 Particle Clustering	94
6.9 Analysis of Coupling Sources	107
6.10 Summary of Channel Flow Cases	113
7 Conclusions and Outlook	115
Appendices	118
A Numerical Formulation	119
B Taylor-Vortex Case	123
C Turbulent Channel Flow	127
D Variation of Reynolds Number	130
E Crossing Particle Jets	133

LIST OF FIGURES

Figure	Page	
1.1	<i>Example of a possible near wall region snapshot. The particle volume may be a significant portion of the near wall grid cell volume and the particle diameter can be much larger than the wall-normal grid spacing.</i>	4
4.1	<i>A cross section of the grid used for the short domain case. There is no jet inlet or dump region to distance the convective outlet from the region of interest in the flow.</i>	38
4.2	<i>A cross section of the grid used for the extended domain case. The slot provides a true inlet condition and the dump region separates the region where measurements occur from the outlet boundary.</i>	38
4.3	<i>Mean streamwise gas velocity versus downstream distance along the centerline of the jet.</i>	39
4.4	<i>Mean streamwise gas velocity vs lateral distance from the centerline of the jet.</i>	39
4.5	<i>Mean streamwise particle velocity vs downstream distance along the centerline of the jet.</i>	40
4.6	<i>Mean streamwise particle velocity vs lateral distance from the centerline of the jet.</i>	40
4.7	<i>Streamwise gas RMS velocity vs downstream distance along the centerline of the jet.</i>	41
4.8	<i>Lateral gas RMS velocity vs downstream distance along the centerline of the jet.</i>	41
4.9	<i>Vertical gas RMS velocity vs downstream distance along the centerline of the jet.</i>	42
4.10	<i>Streamwise gas RMS velocity vs lateral distance from the centerline of the jet.</i>	42
4.11	<i>Lateral gas RMS velocity vs lateral distance from the centerline of the jet.</i>	43
4.12	<i>Vertical gas RMS velocity vs lateral distance from the centerline of the jet.</i>	43
4.13	<i>Reynolds stress distribution vs lateral distance from the centerline of the jet.</i>	44

LIST OF FIGURES (Continued)

Figure	Page
4.14 <i>Streamwise particle RMS velocity vs downstream distance along the centerline of the jet.</i>	44
5.1 <i>The non-dimensional settling location of the bubbles. • experimental data from Sridhar & Katz, □ one-way and two-way coupling, △ volumetric coupling.</i>	48
5.2 <i>Radial vorticity distribution as a function of distance from the centerline. The solid line is the distribution for the volumetric coupling approximation and the dashed line is from the two-way coupling approximation.</i>	49
5.3 <i>Snapshots in time of particle locations under the two-way coupling approximation.</i>	50
5.4 <i>Snapshots of velocity vectors in time using the two-way coupling approximation.</i>	51
5.5 <i>Snapshots in time of particle locations under the volumetric coupling approximation.</i>	51
5.6 <i>Snapshots of velocity vectors in time using the volumetric coupling approximation.</i>	52
5.7 <i>Normalized axial pressure gradient along the centerline of the jet. The solid line represents the results from volumetric coupling approximation and the dashed line the two-way coupling results.</i>	53
5.8 <i>Normalized kinetic energy along the centerline of the jet. The solid line represents the results from volumetric coupling approximation and the dashed line the two-way coupling results.</i>	53
5.9 <i>Figures (a-d) show the particle locations and contours of volume fraction. Figures (e-h) show gas phase velocity vectors and contours of streamwise velocity.</i>	54
5.10 <i>Particle volume fraction using the finite volume approach.</i>	55
5.11 <i>(a) Streamwise gas rms velocity. (b) Wall-normal gas rms velocity.</i>	56
5.12 <i>Time progression of falling particle locations.</i>	57
5.13 <i>Progressive Falling Particle Images</i>	58

LIST OF FIGURES (Continued)

Figure	Page
5.14 <i>Particle pile height as a function of time.</i>	59
6.1 <i>Cross section of the turbulent channel flow mesh used in this work.</i> 61	
6.2 <i>Instantaneous snapshot of a vertical gas phase velocity from a case in this work.</i>	61
6.3 <i>Case 1: Mean Streamwise Gas and Particle Velocities</i>	64
6.4 <i>Case 1: RMS Streamwise Gas and Particle Velocities</i>	64
6.5 <i>Case 2: Mean Streamwise Gas and Particle Velocities</i>	65
6.6 <i>Case 2: RMS Streamwise Gas and Particle Velocities</i>	65
6.7 <i>Case 3: Mean Streamwise Gas and Particle Velocities</i>	66
6.8 <i>Case 3: RMS Streamwise Gas and Particle Velocities</i>	66
6.9 <i>Streamwise Mean Velocity for the case when $m = 1$ and $St = 70$.</i>	67
6.10 <i>Normalized Particle Volume Fraction vs Wall Normal Distance.</i>	68
6.11 <i>CPG vs. CMF Forcing, Mean Flow Velocity for the case when $m = 0.01$ and $St = 0.89$</i>	69
6.12 <i>CPG vs CMF Forcing, RMS Velocity for the case when $m = 0.01$ and $St = 0.89$</i>	69
6.13 <i>Mass Loading Effect on Mean Velocity Profile (CPG) for the case when $m = 1$ and $St = 70$</i>	70
6.14 <i>Mass Loading Effect on RMS Velocity Profile (CPG) for the case when $m = 1$ and $St = 70$</i>	70
6.15 <i>Mean streamwise gas velocity for varying mass loadings ran with two-way coupling and neglecting the effect of collisions.</i>	73
6.16 <i>Streamwise RMS gas velocity for varying mass loadings ran with two-way coupling and neglecting the effect of collisions.</i>	73

LIST OF FIGURES (Continued)

Figure	Page
6.17 <i>Wall-normal RMS gas velocity for varying mass loadings ran with two-way coupling and neglecting the effect of collisions.</i>	74
6.18 <i>Lateral RMS gas velocity for varying mass loadings ran with two-way coupling and neglecting the effect of collisions.</i>	74
6.19 <i>Mean streamwise particle velocity for varying mass loadings ran with two-way coupling and neglecting the effect of collisions.</i>	75
6.20 <i>Streamwise RMS particle velocity for varying mass loadings ran with two-way coupling and neglecting the effect of collisions.</i>	75
6.21 <i>Wall-normal RMS particle velocity for varying mass loadings ran with two-way coupling and neglecting the effect of collisions.</i>	75
6.22 <i>Lateral RMS particle velocity for varying mass loadings ran with two-way coupling and neglecting the effect of collisions.</i>	75
6.23 <i>Wall-normal volume fraction profile for varying mass loadings ran with two-way coupling and neglecting the effect of collisions.</i>	76
6.24 <i>Mean streamwise gas velocity for $m = 0.01$, with the coupling and collision method indicated in the legend.</i>	77
6.25 <i>Streamwise RMS gas velocity for $m = 0.01$, with the coupling and collision method indicated in the legend.</i>	77
6.26 <i>Wall-normal RMS gas velocity for $m = 0.01$, with the coupling and collision method indicated in the legend.</i>	77
6.27 <i>Lateral RMS gas velocity for $m = 0.01$, with the coupling and collision method indicated in the legend.</i>	77
6.28 <i>Streamwise RMS particle velocity for $m = 0.01$, with the coupling and collision method indicated in the legend.</i>	78
6.29 <i>Wall-normal RMS particle velocity for $m = 0.01$, with the coupling and collision method indicated in the legend.</i>	78
6.30 <i>Lateral RMS particle velocity for $m = 0.01$, with the coupling and collision method indicated in the legend.</i>	79

LIST OF FIGURES (Continued)

Figure	Page
6.31 <i>Wall-normal volume fraction profile for $m = 0.01$, with the coupling and collision method indicated in the legend.</i>	79
6.32 <i>Streamwise energy spectra versus wave number for the case when $m = 0.01$ and $St = 0.89$.</i>	80
6.33 <i>Streamwise mean gas velocity for $m = 1$, with the coupling and collision method indicated in the legend.</i>	80
6.34 <i>Streamwise RMS gas velocity for $m = 1$, with the coupling and collision method indicated in the legend.</i>	80
6.35 <i>Wall-normal RMS gas velocity for $m = 1$, with the coupling and collision method indicated in the legend.</i>	81
6.36 <i>Lateral RMS gas velocity for $m = 1$, with the coupling and collision method indicated in the legend.</i>	81
6.37 <i>Streamwise RMS particle velocity for $m = 1$, with the coupling and collision method indicated in the legend.</i>	81
6.38 <i>Wall-normal RMS particle velocity for $m = 1$, with the coupling and collision method indicated in the legend.</i>	81
6.39 <i>Lateral RMS particle velocity for $m = 1$, with the coupling and collision method indicated in the legend.</i>	82
6.40 <i>Wall-normal volume fraction profile for $m = 1$, with the coupling and collision method indicated in the legend.</i>	82
6.41 <i>Streamwise energy spectra versus wave number for the case when $m = 1$ and $St = 70$.</i>	83
6.42 <i>Instantaneous gas velocity profile at a near wall plane corresponding to $y^+ = 4$ for the clean gas case ($m = 0$).</i>	84
6.43 <i>Instantaneous particle structures in the near wall region ($0 < y^+ < 4$) for the $m = 0.01$ case using volumetric coupling and neglecting the effects of collisions, with $St = 0.89$.</i>	85

LIST OF FIGURES (Continued)

Figure	Page
6.44 <i>Instantaneous gas velocity profile at a near wall plane corresponding to $y^+ = 4$ for the $m = 0.01$ case using volumetric coupling and neglecting the effects of collisions, with $St = 0.89$.</i>	85
6.45 <i>Instantaneous particle structures in the near wall region ($0 < y^+ < 4$) for the $m = 0.2$ case using two-way coupling and neglecting the effects of collisions, with $St = 10$.</i>	86
6.46 <i>Instantaneous gas velocity profile at a near wall plane corresponding to $y^+ = 4$ for the $m = 0.2$ case with two-way coupling and neglecting the effects of collisions, with $St = 10$.</i>	86
6.47 <i>Instantaneous particle structures in the near wall region ($0 < y^+ < 4$) for the $m = 0.2$ case using two-way coupling and neglecting the effects of collisions, with $St = 70$.</i>	86
6.48 <i>Instantaneous gas velocity profile at a near wall plane corresponding to $y^+ = 4$ for the $m = 0.2$ case using two-way coupling and neglecting the effects of collisions, with $St = 70$.</i>	86
6.49 <i>Instantaneous particle structures in the near wall region ($0 < y^+ < 4$) for the $m = 1$ case using two-way coupling and neglecting the effects of collisions, with $St = 70$.</i>	87
6.50 <i>Instantaneous gas velocity profile at a near wall plane corresponding to $y^+ = 4$ for the $m = 1$ case with two-way coupling and neglecting the effects of collisions, with $St = 70$.</i>	87
6.51 <i>Instantaneous particle structures in the near wall region ($0 < y^+ < 4$) for the $m = 1$ case using volumetric coupling and neglecting the effects of collisions, with $St = 70$.</i>	88
6.52 <i>Instantaneous gas velocity profile at a near wall plane corresponding to $y^+ = 4$ for the $m = 1$ case with volumetric coupling and neglecting the effects of collisions, with $St = 70$.</i>	88
6.53 <i>Instantaneous particle structures in the near wall region ($0 < y^+ < 4$) for the $m = 0.01$ case using volumetric coupling and including the effects of collisions, with $St = 0.89$.</i>	89

LIST OF FIGURES (Continued)

Figure	Page
6.54 <i>Instantaneous gas velocity profile at a near wall plane corresponding to $y^+ = 4$ for the $m = 0.01$ case with volumetric coupling and including the effects of collisions, with $St = 0.89$.</i>	89
6.55 <i>Instantaneous particle structures in the near wall region ($0 < y^+ < 4$) for the $m = 1$ case using volumetric coupling and including the effects of collisions, with $St = 70$.</i>	90
6.56 <i>Instantaneous gas velocity profile at a near wall plane corresponding to $y^+ = 4$ for the $m = 1$ case with volumetric coupling and including the effects of collisions, with $St = 70$.</i>	90
6.57 <i>Instantaneous particle structures in the near wall region ($0 < y^+ < 4$) for the $m = 1$ case using two-way coupling and including the effects of collisions, with $St = 70$.</i>	90
6.58 <i>Instantaneous gas velocity profile at a near wall plane corresponding to $y^+ = 4$ for the $m = 1$ case with two-way coupling and including the effects of collisions, with $St = 70$.</i>	90
6.59 <i>Case 1: Wall Normal Streamwise Particle Structures $m = 0.01$, $d_p = 28\mu m$ - Volumetric Coupling</i>	91
6.60 <i>Case 2: Wall Normal Streamwise Particle Structures</i>	92
6.61 <i>Case 3: Wall Normal Streamwise Particle Structures</i>	92
6.62 <i>Case 4: Wall Normal Streamwise Particle Structures - Two Way coupling</i>	92
6.63 <i>Case 4: Wall Normal Streamwise Particle Structures - Volumetric coupling</i>	92
6.64 <i>PDF of particle distribution over the entire domain for the case with $m = 0.01$ and $St = 0.89$. The coupling method and inclusion of collisions are indicated in the legend.</i>	95
6.65 <i>The difference of the actual distribution and the Poisson distribution over the entire domain for the case with $m = 0.01$ and $St = 0.89$. The coupling method and inclusion of collisions are indicated in the legend.</i>	95

LIST OF FIGURES (Continued)

Figure	Page
6.66 <i>The difference of the actual distribution and the Poisson distribution in a slice 1/20th the thickness of the domain next to the wall for the case with $m = 0.01$ and $St = 0.89$. The coupling method and inclusion of collisions are indicated in the legend.</i>	
6.67 <i>The difference of the actual distribution and the Poisson distribution in a slice 1/20th the thickness of the domain taken halfway between the wall and the channel centerline for the case with $m = 0.01$ and $St = 0.89$. The coupling method and inclusion of collisions are indicated in the legend.</i>	96
6.68 <i>The difference of the actual distribution and the Poisson distribution in a slice 1/20th the thickness of the domain in the channel centerline for the case with $m = 0.01$ and $St = 0.89$. The coupling method and inclusion of collisions are indicated in the legend.</i>	97
6.69 <i>The average difference of the actual distribution and the Poisson distribution in each of the 20 slices of the domain for the case with $m = 0.01$ and $St = 0.89$. The coupling method and inclusion of collisions are indicated in the legend.</i>	97
6.70 <i>The average difference of the actual distribution and the Poisson distribution averaged over 16 slices in the lateral direction for the case with $m = 0.01$ and $St = 0.89$. The coupling method and inclusion of collisions are indicated in the legend.</i>	98
6.71 <i>Particle radial distribution functions for the indicated coupling method and collision effect for the case where $m = 0.01$ and $St = 0.89$.</i>	99
6.72 <i>PDF of particle number density over the entire domain plotted against the Poisson distribution for the case when $m = 1$ and $St = 70$. The inclusion of collisions and the coupling method are indicated in the legend.</i>	101
6.73 <i>Difference between Poisson distribution and actual distribution of particle number density over the entire domain for the case when $m = 1$ and $St = 70$. The inclusion of collisions and the coupling method are indicated in the legend.</i>	101

LIST OF FIGURES (Continued)

Figure	Page
6.74 <i>Average difference between Poisson distribution and actual distribution of particle number density in a near wall slice with a thickness of one twentieth of the channel width for the case when $m = 1$ and $St = 70$. The inclusion of collisions and the coupling method are indicated in the legend.</i>	102
6.75 <i>Average difference between Poisson distribution and actual distribution of particle number density in a slice taken halfway between the wall and the channel centerplane for the case when $m = 1$ and $St = 70$. The inclusion of collisions and the coupling method are indicated in the legend.</i>	102
6.76 <i>Average difference between Poisson distribution and actual distribution of particle number density in a slice at the centerline of the channel for the case when $m = 1$ and $St = 70$. The inclusion of collisions and the coupling method are indicated in the legend.</i>	103
6.77 <i>Average difference between Poisson distribution and actual distribution of particle number density averaged over ten wall normal slices for the case when $m = 1$ and $St = 70$. The inclusion of collisions and the coupling method are indicated in the legend.</i>	103
6.78 <i>Average difference between Poisson distribution and actual distribution of particle number density averaged over 16 lateral slices for the case when $m = 1$ and $St = 70$. The inclusion of collisions and the coupling method are indicated in the legend.</i>	104
6.79 <i>Particle radial distribution functions for the indicated coupling method and collision effect for the case where $m = 1$ and $St = 70$.</i>	105
6.80 <i>Average difference between Poisson distribution and actual distribution of particle number density over the entire domain for the case when $m = 5$ and $St = 70$. The inclusion of collisions and the coupling method are indicated in the legend.</i>	106
6.81 <i>Average difference between Poisson distribution and actual distribution of particle number density averaged over 16 wall normal slices for the case when $m = 5$ and $St = 70$. The inclusion of collisions and the coupling method are indicated in the legend.</i>	106

LIST OF FIGURES (Continued)

<u>Figure</u>	<u>Page</u>
6.82 <i>Wall-normal particle volume fraction for the case where $m = 1$ and $St = 70$.</i>	108
6.83 <i>Wall-normal average profile of fluid divergence. The wall is at $0.02m$ and the channel centerline is at $0.0m$.</i>	110
6.84 <i>Wall-normal average profile of the ratio of two-way coupling forces to volumetric coupling forces. The wall is at $0.02m$ and the channel centerline is at $0.0m$.</i>	110

LIST OF TABLES

<u>Table</u>		<u>Page</u>
4.1	Particle-laden Jet Case - Computational Parameters	38
5.1	Motivational Cases	46
6.1	Particle-laden Channel - Computational Parameters	62
6.2	Clustering Measurements ($m = 0.01$, $St = 0.89$)	94
6.3	Clustering Measurements ($m = 1.0$, $St = 70$)	100
6.4	Clustering Measurements ($m = 5.0$, $St = 70$)	105
6.5	Two-Way to Volumetric Coupling Force Ratios	111

LIST OF APPENDIX FIGURES

Figure	Page
B.1 <i>Mesh for the coarse grid Taylor-Vortex case.</i>	123
B.2 <i>Mesh for the resolved grid Taylor-Vortex case.</i>	123
B.3 <i>Coarse Grid - \hat{x} Velocity.</i>	124
B.4 <i>Resolved Grid - \hat{x} Velocity.</i>	124
B.5 <i>L_∞ norm error. Lines indicate 1st and 2nd order error for reference.</i> . .	125
C.1 <i>Mean Streamwise Gas Velocity for the turbulent channel flow case, $Re_\tau = 180$.</i>	128
C.2 <i>Streamwise RMS Velocity for the turbulent channel flow case, $Re_\tau = 180$.</i>	128
C.3 <i>Wall Normal RMS Velocity for the turbulent channel flow case, $Re_\tau = 180$</i>	129
C.4 <i>Lateral RMS Velocity for the turbulent channel flow case, $Re_\tau = 180$</i> . .	129
D.1 <i>Mean Streamwise Velocity for the varying Reynolds number case, $Re_\tau = 180$</i>	130
D.2 <i>Streamwise RMS Velocity for the varying Reynolds number case, $Re_\tau = 180$</i>	130
D.3 <i>Mean Streamwise Velocity for the varying Reynolds number case, $Re_\tau = 395$</i>	131
D.4 <i>Streamwise RMS Velocity for the varying Reynolds number case, $Re_\tau = 395$</i>	131
D.5 <i>Mean Streamwise Velocity for the varying Reynolds number case, $Re_\tau = 590$</i>	132
D.6 <i>Streamwise RMS Velocity for the varying Reynolds number case, $Re_\tau = 590$</i>	132
E.1 <i>Dilute jet case: Particle volume fraction contours</i>	134
E.2 <i>Dilute jet case: Particle volume fraction contour flood map</i> . . .	134
E.3 <i>Dense jet case: Particle volume fraction contours</i>	135

LIST OF APPENDIX FIGURES (Continued)

<u>Figure</u>	<u>Page</u>
E.4 <i>Dense jet case: Particle volume fraction contour flood map</i>	135

LIST OF APPENDIX TABLES

<u>Table</u>	<u>Page</u>
C.1 Turbulent Channel Flow - Computational Parameters	127
E.1 Crossing Particle Jets - Computational Parameters	134

DEDICATION

To Bill Sullivan, Terry Kiser, Tom McCready, Yongmei Jin and Ivan Christov...

Investigation of volumetric coupling effects on particle-laden
turbulent flows at dilute to moderate loadings

Chapter 1 – Introduction

Particle-laden turbulent flows are found in a wide variety of engineering applications. From electrostatic precipitation, riser and downer flows in production processes, engines and furnaces to contaminant transport and pollution control. One application of particular interest is particle transport in oxy-coal combustion processes. In this process an accurate understanding of particle dispersion and turbulent flow fields is important to be able to adequately model and assess performance of these power plants. Improving our understanding of particle dispersion modeling is key because the efficiency of these burners is intimately related to the particle spacing within the reactor.

The majority of previous work on particle-laden flows has utilized direct numerical simulation (DNS), large-eddy simulation (LES) and Reynolds averaged Navier-Stokes (RANS) methods to simulate particle-laden turbulent flows. Studies such as Vreman (2007) used direct numerical simulation to study particle-laden flows in a pipe by approximating particles as point sources of momentum [1]. Yamamoto et al. (2001) used this same approximation utilizing large-eddy simulation while Lain and Sommerfeld (2007) used Reynolds averaged Navier-Stokes simulation [2] [3]. A review of some basic findings and conclusions is presented in chapter 2, including discussions of the general methods for modeling particle-laden flows, the various common coupling approximations, particle size effects, the displacement of fluid by particles, particle clustering and the differences between direct numerical simulation and large eddy simulation. Most of the literature focuses on the “point-particle” approach to modeling particle-laden turbulent flows; wherein, the disperse particles are treated as point-sources of momentum coupling.

For many flows this is an excellent approximation, this work compares the results from a series of simulations using both the point particle approach and a “volumetric coupling” approach, wherein the volume displaced by the particles is accounted for. Previous work taking into account the fluid displacement by particles in turbulent flows has concluded that for moderate Stokes number particles at low mass loading, there is little difference [1].

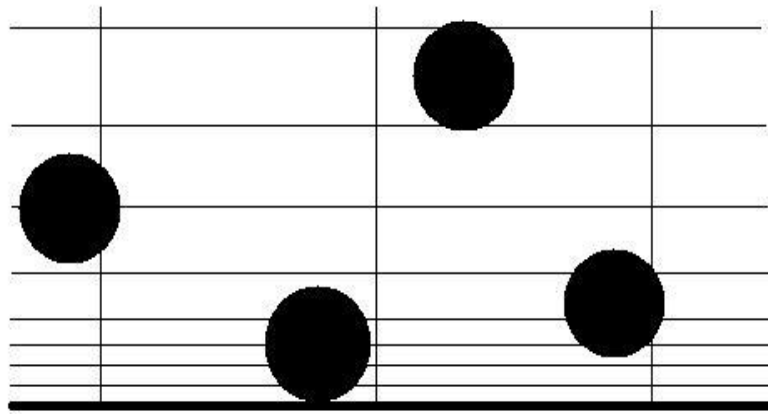


Figure 1.1: *Example of a possible near wall region snapshot. The particle volume may be a significant portion of the near wall grid cell volume and the particle diameter can be much larger than the wall-normal grid spacing.*

Figure 1.1 shows an example of a close up of the near wall section of a channel flow. While the volume of the individual grid cells is larger than the volume of a particle, the wall normal grid cell length is less than the particle diameter for the near wall cells. Even though the volume is larger, the ratio of the cell volume to

the particle volume will not necessarily be high, just greater than one. Thus the flux into and out of grid cells due to particle motion could be quite large when accounting for the fluid displaced by the particles. This work studies how this feature affects a particle-laden channel flow at low to moderate mass loadings.

In this work large-eddy simulation of particle-laden turbulent flows is performed. A fractional step solver is utilized to solve the fluid phase equations while the particles are tracked in a Lagrangian manner. Particle motion is determined by modeling the various forces acting on the particle such as gravity, drag, lift, etc. while the motion is coupled explicitly to the fluid phase. Particular attention is paid to the coupling method between the fluid and particle phases. Many studies have utilized the “two-way coupling” approach to study the dynamics of particle-laden flows and their dispersion properties. Significantly less work has been done using volumetric coupling to study these same properties. In this work two-way and volumetric coupling results are compared to determine what effect the choice of method has on the particle dispersion properties and the flow statistics. Several methods of determining these effects are used. Traditional statistics such as mean gas and particle velocities are calculated. The root mean square velocities in all three Cartesian coordinates for both particle and gas phases are compared as well. The volume fraction profile is important as it provides a measure of the wall normal distribution of particles. Energy spectra give an idea as to how the various coupling method’s affect the turbulent flow structure. Near wall and channel centerline gas and particle phase images are used for visual validation of results. The last type of analysis performed is finding probability density functions and radial

distribution functions of particle distributions within the flow domain.

Chapter 2 – Literature review

A few issues pertinent to this work will now be discussed. This overview will be split into sections on numerical modeling methods, large-eddy simulation of turbulent flows, mechanics of two-way coupling, four-way coupling influence and the effect of the finite-volume of the particles on the structure of turbulence. These topics are of direct importance to the work presented, so a comprehensive understanding of these mechanisms is key to effective multiphase flow modeling. These sections will simply present a broad view of these topics, more concrete information can be found in sources such as [8] [9] [10] [11] [13].

2.1 Modeling Methods

As mentioned previously, there are several options available for modeling multiphase flows, the method of choice is completely dependent upon the application. Several common methods for this will be discussed as well as mention given to their capabilities as predictive tools for the current set up.

The first method is a Lagrangian-Lagrangian technique known as a molecular dynamics modeling, in which both the carrier fluid phase and the dispersed particle phase are treated in a Lagrangian manner, which in this case refers to the treatment of particles individually. Each particle is tracked separately and its motion governed by Newton's Laws of motion. Interphase effects are based on the collisions of carrier phase molecules with particles. These types of models can be very accurate but are extremely limited in scope due to the computational cost of simulating a significant domain. Essentially these models are only viable for

extremely small scale domains. Higher level models would be more appropriate for handling the current work [10].

The next method utilized is an Eulerian-Lagrangian construct known as fully resolved simulation. The carrier phase is treated as an Eulerian quantity in which the motion is calculated using direct numerical simulation for the fluid equations of motion, thus resolving all the scales of motion from the integral scale down to the Kolmogorov scale. This yields a high degree of accuracy for pure fluid motion, the interaction with the particle phase is the next concern. Particles are fully resolved and thus their motion requires no modeling. Another method utilizes direct numerical simulation for the fluid phase, but the particles are not fully resolved, thus modeling is required. Particles are handled in a Lagrangian sense with the motion of the particles determined by a set of equations, for example the equations of motion developed by Maxey and Riley [18], which describes the rigid body motion of a sphere. The velocity field around the particles is well resolved yielding accurate trajectories for particles. This method is quite expensive because the grid scales must be small everywhere to resolve the no-slip condition around the particle, not just at the wall. Direct numerical simulation provides a great tool for building sub-grid scale models for use in large-eddy simulation [7] [10] .

Similar to the previous method, another example of an Eulerian-Lagrangian method is unresolved simulation, the prime example of which is large-eddy simulation. In large-eddy simulation, the carrier phase motion is solved on a relatively coarse grid compared to direct numerical simulation, thus where the name large-eddy simulation comes from. The smallest eddies are not resolved with the grid,

only the motion of the largest eddies is directly computed. The particle phase is handled in a similar manner to the resolved modeling efforts, the velocity field is however not resolved around the particle. Since the vast majority of the dissipation occurs at the smallest scales a model must be implemented in order to effectively have the energy balance within the flow. Large-eddy simulation is a logical choice for the types of flows being studied as the lower Reynolds numbers make it tractable for simulation unlike some high Reynolds number external flows [8] [19] [20]. It is also a good tool for building closure models and an understanding of particle behavior in complex systems in order to build two-fluid models [10].

The next larger level models are Eulerian-Eulerian, such as the two-fluid model in which both phases are treated as continuum quantities, thus individual particles are no longer being followed [10]. Conservation of mass and momentum equations must be solved for both phases [14] [15]. The interaction between the phases and between particles is handled using models based on spatial volume fraction gradients [14]. With accurate models for this behavior two-fluid models can be just as concise and considerably less computationally expensive than Euler-Lagrangian simulations. Studies show that even with the current underdeveloped two-fluid modeling closures good accuracy can be achieved with more than two orders of magnitude less effort than direct numerical simulation [7] [21]. The main downfalls of this method are its failures when high particle concentration gradients occur.

Another type of method that is often utilized for its computational efficiency is known as Reynolds averaged Navier-Stokes modeling. In this method the physical

parameters are split into a mean and fluctuating component and substituted into the equations of motion. The equations are then time averaged and rearranged into a final form. This process then relates mean properties of the flow with one unknown quantity. This quantity is known as the Reynolds stress tensor because it represents forces on the a local fluid volume due to turbulent stresses. Several attempts have been made to relate this unknown tensor to the current variables in order to close the system. These have been met with varying degrees of success. The two most common closure methods are the k - ϵ and k - ω models. In these models dimensional analysis yields a relationship for the various Reynolds Stress tensor quantities, then are provided by solving transport equations for say k and ϵ if the k - ϵ model is being used. These quantities are then used to solve the fluid momentum equation. Several models are used to include the effect of particles on the fluid phase, see Yu (2005) , Rizk (1993) , Lun (2000) , Zhou (2008) and Lain (2003) for examples [22] [23] [24] [25] [26]. These models seem to be effective for well understood systems where the needed relationships have been well established and tested. This is not ideal for true predictive capability in new flows and geometries. The common complaints about Reynolds averaged Navier-Stokes models (RANS models) are that in more complex geometries the inaccuracies in calculating fluid phase motion can be significant. When the fluid phase properties are not handled properly the motion of the particles is then not calculated properly as a result [20] [27] [28] [29]. When this happens the two-way coupling effect causes non-physical momentum transfer back to the carrier phase further eroding the accuracy. These inaccuracies yield both problematic fluid and gas phase

velocities but also improper particle dispersive behavior [27]. Also, in RANS simulations particles are often treated as parcels of particles. The implementation of this method has implications that are not always clearly understood with respect to handled phase-coupling and collisions [20].

The most popular methods of handling particle-laden flows have been discussed, however other techniques exist but are considerably less popular. One of these methods involves using finite elements [30] and this can be combined with Lagrangian particle tracking in a similar fashion to the work done here. Another method uses the integrated Boltzman equations with a variety of possibilities for handling the particle phase, such as Lagrangian particle tracking or stochastic motion modeling [31]. A more rare method uses Lagrangian eddy interaction models and Lagrangian particle tracking, but seems to be limited in its scope [32]. The last of the less common methods that will be mentioned is vortex simulation with Lagrangian particle tracking [33]. A more robust review of the common modeling methods can be found in the literature, such as Deen et al. (2007) and van der Hoef et al. (2008) [10] [34].

2.2 Flow Regimes and Coupling Methods

The assumption that the particle density is much higher than that of the carrier phase fluid, i.e. $\rho_p/\rho_f \gg 1$ is used here. With this assumption in mind it has been found that the dominant physical processes in determining the flow structure and particle dispersion still have a great deal of variation with flow properties.

There are two properties in particular which seem to determine the regime in which varying processes tend to dominate the characteristic behavior. The particle Stokes number, or the relative particle response time scale to the flow's small structure time scale is one, the other is the particle volume fraction. At low loading the particles tend to exert an extremely low level of influence on the flow structure, as such these low loadings are known as the one-way coupling regime where the fluid structure determines the particle phase motion, but the particle motion has a negligible effect on the flow structure. At higher loadings the particles become numerous enough that based on their size, their combined momentum coupling to the carrier phase becomes significant. At the higher end of the regime the dominant process is the momentum transfer between the phases, overshadowing the carrier phase flow field. This regime is known as the two-way coupling regime because the dominant physics is determined by the momentum transfer from the carrier phase to the particulate phase and vice versa. At even higher loadings the inter-particle collisions come to dominate the momentum transfer, this is termed four-way coupling, two for the coupling between the carrier and particulate phases and two for the coupling between colliding particles.

2.2.1 One-Way Coupling

When a method for simulation is chosen for a given flow configuration it is often beneficial to make approximations. One of the most rudimentary approximations we can make for such flows is known as the one-way coupling approximation. In

this approximation the fluid phase motions are used to push the particles, thus particle motion is determined through this fluid phase motion and a basic drag law, such as that of flow over a sphere. In some studies additional forces can be considered on the particle such as lift, added mass, etc. Physically it is understood that the particles can transfer momentum back to the fluid through the no-slip boundary condition. This is where the name of the approximation comes from, the momentum is only transferred in one way, from the fluid to the particles. As stated before, this is not a physical reality, this is an approximation meant to save time and/or effort for both the user and computer. This approximation is ideal for dilute flows containing particles of low Stokes number [35] [36] [37]. For flows with higher volume loadings a more involved approximation is used in order to achieve some reasonable measure of accuracy.

2.2.2 Two-Way Coupling

In studies involving so called two-way coupling an added level of complexity is seen. The two-way coupling is so named because momentum is transferred from the fluid to the particles and then echoed back from the particles to the fluid in differing quantities, thus the momentum is transferred in two ways. From this explicit fluid phase information several forces acting on the particle can be calculated. These forces can be drag, gravity, pressure, added mass, lift and others. When the explicit velocity field is known and the particle properties are known the second aspect of the two-way coupling force can be calculated. This is the momentum that

the particle imparts on the fluid through its relative motion within with carrier phase.

It is common practice in many heavy particle-laden flows to assume that the drag and gravity forces are the only ones acting on a particle. While this is, in general, a good approximation other authors have evaluated the importance of other forces. While the overall conclusion is the same, it is not entirely clear exactly when and to what degree these small forces could have a large affect [38] [39].

2.2.3 Four-Way Coupling

The so called four-way coupling approximation is named so because it uses the same two methods of transferring momentum as two-way coupling, as well as includes the ability for particles to transfer momentum among themselves. Thus particle A transferring momentum to particle B is the third way, and the reverse process constitutes the fourth method of coupling. The inclusion of these computations becomes important when inter-particle collisions begin to lead to preferential accumulation, thus the momentum transfer between particles and their then augmented momentum transfer to the fluid become the dominant factors in determining flow characteristics [21]. This behavioral regime tends to be dominant in flows with large volume fractions or more moderate volume fractions but consists of particles with larger Stokes numbers [37].

2.2.4 Volumetric Coupling

When Lagrangian particle tracking methods were first utilized they made what is commonly called the point-particle assumption. This just means that the carrier phase has no knowledge of particle volume, as such the particles displace no mass, much as a point source. The particles were tracked based on their center location and their motion was determined through the afore mentioned methodology. The only manner in which the mean flow knows of the particle existence is through a momentum source in the fluid momentum equations. For many types of flows this is a perfectly valid approximation because either the displaced mass is small due to a low particle volume fraction, or the dynamics of the flow are not strongly affected by more moderate amounts of displaced mass [40].

Volumetric coupling utilizes knowledge of particle locations within the carrier phase to determine local volume fractions. The in-cell density of the fluid is then augmented to reflect the local volume fraction. For example, if a fluid has a density of 1 kg/m^3 and is sitting in a control volume with a volume of 1 m^3 the local density would read 1 kg/m^3 . However, if half of this same control volume were occupied by particles the local density of the carrier phase would then be interpreted as $1/2 \text{ kg/m}^3$. This method creates a sort of path of least resistance for particle travel and appropriately lessens the effects of the fluid phase on neighboring control volumes. A side effect of this method is that the wake effect from particle travel is indirectly modeled. It is not entirely clear when volumetric coupling will result in drastic changes in flow structures. Relatively dense particle-laden flows seem like likely

candidates for this factor to have a significant effect, however, for particle-laden turbulent flows, such as wall bounded channel flows, its effects need to be studied even at moderate mass loadings.

Several studies have developed different methods for taking into account the fluid displaced by the presence of particles. The importance of this effect can vary drastically depending on the physical system being studied. In some systems, such a collection of particles under the influence of gravity settling into a pile, the inclusion of finite-sized effects is small since the dominant physics are the effects of gravity and inter-particle collisions [40]. Yu et al. used Reynolds averaged Navier-Stokes modeling with the inclusion of finite sized effects to model a particle-laden channel flow, they conclude that the inclusion of these effects leads to a more uniform concentration of particles within the domain [22]. Mizk (1993) and Lun (2000) used $k - \epsilon$ and $k - \omega$ Reynolds averaged Navier-Stokes models respectively to study particle-laden jet and particle-laden channel flows [23] [24]. It is difficult to interpret the results of their work and apply it to direct numerical simulation or large-eddy simulation methods. The reason for this is the large relative grid size differences between the methods. In DNS and LES, the grid cells are not large in the wall-normal direction in comparison with the particle diameter whereas, typically the cell size requirements are not as strict in RANS modeling. In Eulerian-Lagrangian modeling efforts such as DNS and LES, the assumption of having subgrid scale particles is an important one, but can break down in the near wall region [40]. Studies have shown that even for relatively dilute flows the local particle clustering properties can vary with the inclusion of finite sized effects [40].

2.3 Effects of Varying Particle Size

$$St = \frac{\tau_p}{\tau_k} = \frac{\rho_p d^2 / (18 \rho_f \nu)}{(\nu / \epsilon)^{1/2}} \quad (2.1)$$

Several attempts at classifying regimes of particle behavior based on volume loading and particle Stokes number have been performed. The majority of the research done towards constructing a well defined behavioral regime classification for particle-laden flows has focused on isotropic boundary free turbulence, such as the initial work of Elghobashi's group [11] [12]. The studies tend to focus on this specific set up because it tends to be relatively independent of the initial distributions of particles and is without the effects of geometry and Reynolds number. In a sense it is the best method for studying these effects as it avoids all sorts of only qualitatively understood effects and allows varying just one parameter to change the structures. The problem comes from the fact that these classifications do not generally lend well to any real flow geometry and are augmented by the effects of walls or gravity. Still, some important basic physical insight can be gained through this work. As their group has been at the center of this work, their classification for particle sizes will be utilized. While technically they classify particles by Stokes number, as is done here, the only parameter varied to achieve these Stokes numbers is the particle diameter. Equation 2.1 is the relation used for the Stokes number for work on isotropic turbulence. Equation 2.2 gives the relation used for the Stokes number in the later work, which is applicable for a wall bounded flow. In this definition τ_p is the particle time scale and τ_k is the fluid time scale. The particle time scale is meant to represent the time necessary for

a particle at rest to accelerate to the velocity of a surrounding flow. In defining these quantities ρ_p is the particle density, d is the particle diameter, ρ_f is the fluid density, ν is the kinematic viscosity of the fluid, δ is the channel half-width and U_c is the mean centerline fluid velocity. Changing the fluid time scale to the measure of the integral time scale for the fluid phase makes this definition more appropriate for isotropic turbulence in a periodic domain.

$$St = \frac{\tau_p}{\tau_k} = \frac{\rho_p d^2 / (18 \rho_f \nu)}{(\delta / U_c)} \quad (2.2)$$

Particles are split into four classifications, these classifications are based on their effects on the flow structure and named after their relative sizes. The largest particles are named large particles and have Stokes numbers greater than one. As mentioned before, the Stokes number is in a sense a measure of the relative response times of the particle and the flow. So a Stokes number of greater than one indicates that the particle will take longer to respond to changes in the surrounding flow conditions. This means that large particles do not follow the motions of the flow immediately, in general they will respond mainly to mean flow characteristics [37] [41]. It is found that these large particles tend to be ejected from strong vortices and insert themselves into others by crossing the shear region between them [42]. While it may seem that this means they are strongly coupled to local flow conditions against the previously presented logic, in reality their inertia allows them to overcome these local effects and pass through the shearing regions [37]. The large particle's ability to shred vortices is the physical mechanism by

which they lower both turbulent kinetic energy and dissipation. The dissipation is lowered because as a vortex is shredded, the local velocity gradients become weaker, thus lowering dissipation [37] [42] [43].

The next smaller classification of particle is referred to as critical particles, where the Stokes number is approximately one. Critical particles are so named for their property of preferential accumulation in high shear regions [37] [42]. These particles are ejected from the small scale vortex cores in the same manner as large particles, but do not have sufficient inertia to cross the high shear regions between. Thus the dissipation is reminiscent of single phase flow because of the particle-free nature of these cores. This is where the preferential accumulation is significant since the shear regions between eddies tend to be thin in comparison to the eddy size. The particles largely end up in these structures, resulting in a relatively high particle density, and thus accumulation in these small regions [37] [41] [42]. Thus a slightly lower carrier phase turbulent kinetic energy and a roughly unchanged dissipation rate are produced in comparison with single phase flow.

The third classification given in their work is that of the ghost particle. While it is of theoretical interest, the range in which this classification forms is quite small. These particles are called ghost particles because in looking at kinetic energy, it is difficult to see the presence of these particles in comparison with the spectra of a gas phase flow [37] [42]. Due to the particular nature of this particle behavior regime, the range of Stokes numbers which have this effect is not clear a priori. Depending on the situation, the relevant particle Stokes number is somewhere between 0.1 and 0.5 [37].

The last classification is known as the microparticle, where the Stokes number of these particles is much less than 1. These particles follow the flow changes extremely closely due to their small Stokes numbers [37]. This is seen because the Stokes number is much less than one, which indicates that the time needed for particles to respond to changes in the surrounding fluid environment is much less than the time needed for the flow characteristics themselves to change. Essentially these eddies have higher turbulent kinetic energy than a single phase flow because the largest eddies have a higher inertia due to their increased mass [21] [43]. This is offset by the fact that the smallest eddies also have higher inertia, which yields a larger dissipation [37] [42]. These mechanisms generally contribute, in boundary free isotropic turbulence, to microparticles being the most homogeneously dispersed of the particle size regimes [44]. There is one additional feature of varying particle size that should be briefly mentioned. It is not obvious how a flow will change if both the particle and volume mass loadings are kept constant, but particle size is varied. The previous paragraphs yield some insight, but as explained before these insights have limited functionality in real flows where walls are present and gravity is taken into account. One feature not taken into account in many computational techniques is the effect of the boundary layer that develops around a particle as it travels. These boundary layers are different than the surrounding flow structures and create a buffer zone between the particle and the outside area. When two low inertia particles are on a collision course they must overcome the forces presented by the overlap of these layers, as such in an unresolved flow, the odds of a collision happening when one is computed to occur,

are not necessarily 100%. On the other hand higher inertia particles will likely have little trouble crossing this buffer region [45]. There are two counter producing mechanisms that determine the likelihood of a collision occurring here, one is with many smaller particles there are many quasi-independent flight paths. On the other hand with a lower number of larger particles the odds of two nearby particles colliding is much larger. In general it was found that the effect of inter-particle collisions will be less with small particles than with large particles due to the aforementioned particle boundary layer effect [45]. As from before, it is important to mitigate this with the preferred natural locations for particles in regions of local vorticity [46]. This is something to keep in mind when choosing an appropriate collision method and gives credence to the idea of a hybrid collision model based on both an inter-particle repulsive force and a binary collision model.

2.4 Particle Clustering in Turbulence

A major characteristic of interest in particle-laden turbulent flows is the structure of particle clusters within the flow. Several methods of evaluating particle clustering have been utilized in the literature, many papers rely on visual observations while others use statistical approaches to obtain information about these clusters. The most commonly available information about particle concentrations is the local volume fraction. This does not allow much inference as to the structure of the clusters. There are two relatively common ways of quantitatively evaluating these particle structures. The first is the probability density function methods, or PDF

method, in which the domain is decomposed into smaller bins with which to count the local number of particles and build a distribution of particle number density within the overall domain. A comparison with the Poisson distribution, which is a good representation of a random distribution of particles, gives a measure of the clustering. The second method, called the radial distribution function method, or RDF method, attempts to find a length scale of preferential concentration by building a radially outward distance distribution between particles.

The PDF has been used to evaluate particle clustering in isotropic turbulence in several pieces of work [41] [67]. The comparison to the Poisson distribution is ideal for this case because there are no wall boundaries which cause preferential concentration, this means the only variations in particle concentration present are due to the turbulent fluid structures. In wall bounded flows the comparison becomes more complicated. The same information can be obtained but the cause of the changes in number density can not be determined without further work. The PDF concentration method in these wall bounded flows has been examined experimentally as well as computationally. Studies using isotropic turbulence suggest that the distribution is highly sensitive to particle Stokes number. It was found that in general the largest particles and smallest particles appeared nearly random when the bin size was small, but for larger bin sizes the degree of randomness was smaller for large Stokes number particles but still strong for small Stokes number particles [67]. Other studies indicate that when using one-way coupling the level of preferential concentration is much lower for large Stokes number particles in comparison with small Stokes number particles [41] [68].

Fessler et al. [64] experimentally studied particle clustering in a turbulent channel flow using the PDF method. It was found that the largest Stokes number particles were distributed nearly randomly due to their large inertia in comparison with the strength of the flow structures [64]. Computational studies indicate similar results [2] [69]. In addition it was found that including the effect of collisions increases the degree of randomness in the distribution of particles [2].

The RDF method is not often utilized in wall bounded flows, most likely due to the directional dependence created by the presence of walls. This dependence makes the RDF measurements less meaningful. The RDF has a heavy dependence of Stokes number for isotropic turbulence. The particles with the smallest Stokes number and largest Stokes numbers show the least deviation from a uniform distribution. Stokes numbers near 1 show the strongest clustering for this geometry [67]. It has also been shown that the RDF for a given Stokes number is dependent on the local flow Reynolds number [69].

2.5 Direct Numerical Simulation and Large Eddy Simulation

The relative accuracy of direct numerical simulation and large eddy simulation has been the focus of many studies. Of primary concern is the ability of large eddy simulation to accurately predict the features of both phases of a wall bounded turbulent flow. It has been shown that large eddy simulation does a good job of reproducing the basic turbulent statistics of mean and rms values for both carrier and dispersed phases [27] [50] [70]. It has been found that large eddy

simulation can have problem with predictive capability in the near wall region, which is generally attributed to problems with the models used for the particle equation of motion [28]. Large eddy simulation generally gives different particle dispersion results than experiments, partially due to the lack of including the effect of sub-grid scale fluctuations on the particle motion [50] [70]. The effect of sub-grid scale motion can be quite small or relatively large depending on the flow geometry, features, grid size, filter width and Reynolds number [27] [50] [70]. Essentially the effect of sub-grid scale stresses is tough to predict because of the numerous dependencies involved. A few attempts have been made to improve the accuracy of large eddy simulation by methods such as changing the particle equations of motion to account for inflated response times which yield more accurate particle clustering [70]. There is some evidence to suggest that near wall modeling deficiencies can be made up for by changing the particle-wall collision model used [28]. The effect of sub-grid scale fluctuations has been found to have the largest effect on particle motion for low Stokes number particles [27] [50]. This makes intuitive sense because of the relative time scales of particle and fluid motion, which for this would be the Stokes number using the Kolmogorov time scale as the fluid time scale. If this is small then even the smallest eddies have a significant effect on particle motion.

2.6 Outline of Present Work

This section gives an overview of the work presented. Chapter 3 outlines the mathematical formulation used in this work for the fluid phase motion, particle motion, coupling and inter-particle collisions. Chapter 4 presents some results from a jet case in which a slot nozzle releases particle-laden fluid into an ambient chamber. Chapter 5 presents a few motivational cases to give a better understanding of the relevancy of the work. Section 5.1 presents some results from a study of bubble-vortex interaction. Followed by section 5.2 presents a jet fluidization case and section 5.3 gives some results from a slurry flow case. In these three cases the effect of volumetric coupling is quite significant and shows the importance of the coupling technique on flow simulation. Sections 5.4 and 5.5 present results from the Rayleigh-Taylor instability case and a gravitational settling case. These sections show that for the Stokes numbers and mass loadings studied there was no sizable effect of accounting for the finite size of the particles. This properly motivates the work as specific scenarios in which the volumetric coupling approximation can improve prediction of particle-laden flows are not entirely clear and there is significant reason to believe that for moderate mass loadings this can influence the particle-laden channel flow.

Chapter 6 presents the main body of results. Section 6.1 that gives the problem description followed by 6.2 gives some basic results and makes comparisons to published data. Following this, section 6.3 discusses the forcing method and its effect on the flow. Section 6.4 gives some basic results on the effect of increased

mass loading on the turbulent statistics. The effects of varying the coupling method and changing collision models are presented in section 6.5. Near wall gas phase and particle phase features are discussed in section 6.6 with the channel centerline particle structures given in section 6.7. Particle clustering effects are presented in section 6.8. Section 6.9 details an analysis of the relative magnitude of the two-way and volumetric coupling effects. Chapter 7 provides an overview of the work and results presented here as well as discusses methods of improving the work for future studies.

Appendix A discusses the numerical methods used to implement the mathematical formulation. The methods for computing the fluid phase flow, particle motion, coupling forces and inter-particle collisions are presented within. A validation case of Taylor-Vortex flow is given in Appendix B. Turbulent channel flow results are presented in Appendix C at a Reynolds number of 180. The effect of varying the Reynolds number is shown in Appendix D. A collision model test case of crossing particle jets is shown in Appendix E.

Chapter 3 – Mathematical Formulation

A discussion of the mathematical methods utilized in the present work will be presented here. In the discrete element formulation, the goal is to calculate the carrier phase fluid motion while accounting for the presence of particle motion, inter-particle collisions as well as particle-wall collisions. This can be done using multiple methods, some of which were discussed previously. Direct numerical simulation has been shown to be able to handle computations of this nature. Large eddy simulation is chosen in this work for its applicability to larger domains while maintaining some of the accuracy necessary for providing the building blocks for higher level models, such as two-fluid models. Large eddy simulation provides an excellent tool with which to bridge the gap between direct numerical simulation and these larger scale models.

The methods chosen for carrier phase computations and particle tracking are presented here. This method is classified as an Eulerian-Lagrangian method after its treatment of each of the phases. The carrier phase is treated as an Eulerian quantity while the dispersed phase is treated in a Lagrangian fashion. In particular, the carrier phase is handled using large-eddy simulation employing the dynamic Smagorinsky model. The momentum coupling is taken into account through a source term in the momentum equations, while the particle motion is calculated using the system proposed by [18]. Interparticle collisions are handled using an inter-particle body force method [14] [15]. Particle-wall collisions are handled in the same manner.

The general single phase Navier-Stokes equations and the equation of continuity

are the starting points for the methods in use and are given here:

$$\frac{\partial \rho}{\partial t} + \nabla \cdot (\rho \mathbf{u}) = 0 \quad (3.1)$$

$$\frac{\partial(\rho \mathbf{u})}{\partial t} + \nabla \cdot (\rho \mathbf{u} \mathbf{u}) = -\nabla p + \nabla \cdot (\mu_f (\nabla \mathbf{u} + (\nabla \mathbf{u})^T)) + \rho \mathbf{g} + \mathbf{f} \quad (3.2)$$

where \mathbf{u} is the carrier phase velocity vector, \mathbf{g} represents gravity, ρ is the density, μ_f is the carrier phase dynamic viscosity and \mathbf{f} is a body force source term. ∇u and $(\nabla u)^T$ constitute the symmetric and anti-symmetric parts of the strain-rate tensor respectively. Now the existence of the particle phase and their finite-sizes is taken into account. To do so the local fluid density is obtained by computing the volume fraction of both fluid and particles. Here Θ_f is the carrier or fluid phase volume fraction, analogously the particle volume fraction $\Theta_p = 1 - \Theta_f$ can be defined. So the density of the fluid in any cell is given by $\rho = \Theta_f \rho_f$. Using these definitions the augmented equation of continuity becomes

$$\frac{\partial}{\partial t}(\rho_f \Theta_f) + \nabla \cdot (\rho_f \Theta_f \mathbf{u}_f) = 0 \quad (3.3)$$

which is not divergence free under the assumption of carrier phase incompressibility, as the traditional continuity equation is. This can be shown through a simple manipulation of the conservation of mass equation to show that the divergence of the velocity field is given by

$$\nabla \cdot \mathbf{u}_f = -\frac{1}{\Theta_f} \left(\frac{\partial}{\partial t}(\Theta_f) - \mathbf{u}_f \cdot \nabla(\Theta_f) \right) \quad (3.4)$$

Using the same alteration the momentum equation can be manipulated to reflect the system under study and is shown in equation 3.5

$$\frac{\partial}{\partial t}(\rho_f \Theta_f \mathbf{u}) + \nabla \cdot (\rho_f \Theta_f \mathbf{u} \mathbf{u}_f) = -\Theta_f \nabla p + \nabla \cdot (\mu_f (\nabla \mathbf{u}_c + (\nabla \mathbf{u}_c)^T)) + \mathbf{f} \quad (3.5)$$

yielding the equations of motion for these computations [16] [17] [42]. Here the two-way coupling source is modeled as seen in equation 3.6.

$$\mathbf{f} = (F_p + F_d + F_g + F_l + F_a)/m_a \quad (3.6)$$

Here m_a denotes the added mass correction factor, which represents the damping effect of the added mass on changes in particle motion.

This system of equations is solved directly using the fractional step method. In large eddy simulation, the equations of motion are filtered and density-weighted Favre averaged. This process leaves a subgrid scale stress term which must be handled, this stress term is given in equation 3.7

$$\tau_{ij} = \overline{\rho_f \Theta_f u_i u_j} - \overline{\rho_f \Theta_f u_i} \overline{\rho_f \Theta_f u_j} / \overline{\rho_f \Theta_f} \quad (3.7)$$

The subgrid scale stress term requires a closure model in order for the system to be tractable. The dynamic Smagorinsky model is used and the eddy viscosity is modeled as seen in equation 3.8.

$$\mu_t = -C_S \overline{\rho_f \Theta_f} \Delta^2 \left(\frac{1}{2} S_{ij} S_{ij} \right)^{1/2} \quad (3.8)$$

In the above equation $\Delta = \forall_{cv}^{1/3}$ where \forall_{cv} is the volume of one grid cell. The constant C_S in equation 3.8 is found using the dynamic model with the filter being double size of a control volume. Note in this model the particles affect the subgrid scales of motion directly through fluid void fraction.

Particle motion within the carrier phase field is modeled in the fashion of Darmana et al. [51]. The equations of motion for the particle phase are governed by Newton's second law. The system given here represents this fact.

$$\frac{d}{dt}(\mathbf{x}_p) = \mathbf{u}_p \quad (3.9)$$

$$m_p \frac{d}{dt}(\mathbf{u}_p) = \sum F_{particle} \quad (3.10)$$

where x_p is the particle location, m_p is the mass of an individual particle, \mathbf{u}_p is the particle velocity vector and $F_{particle}$ denotes a generic force acting on a particle. In this case $F_{particle}$ can be broken up into the pressure (F_p), drag (F_g), gravity (F_d), lift (F_ℓ), added mass (F_a) and collision forces (F_{coll}).

$$\sum F_{particle} = F_p + F_d + F_g + F_\ell + F_a + F_{coll} \quad (3.11)$$

Next each of the afore mentioned forces will be examined. First the gravitational force, in which the relative density difference of the particle and fluid yields a

buoyancy force on the particle as shown in equation 3.12.

$$\mathbf{F}_g = (\rho_p - \rho_f)\nabla_p \mathbf{g} \quad (3.12)$$

The volume of the individual particle is denoted as ∇_p , which is assumed to be perfectly spherical. The drag force on the particle is modeled using the standard drag equation for flow past a sphere.

$$\mathbf{F}_d = -(1/2)C_d\rho_f\pi r_p^2|\mathbf{u}_p - \mathbf{u}_f|(\mathbf{u}_p - \mathbf{u}_f) \quad (3.13)$$

where C_d is the drag coefficient, and r_p is the particle radius. There are several models available to select from for the drag coefficient, each model has particular strengths. For the Reynolds number ranges and particle mass loadings being studied here, the Clift model has been selected [52]. In this model the drag coefficient is modeled by equation 3.14.

$$C_d = \frac{24}{Re_p}(1 + 0.15Re_p^{0.687}) \quad (3.14)$$

in which Re_p is the particle Reynolds number, given by $Re_p = (\rho_p d_p |u_p - u_f|)/\mu_f$. The lift force is due to the relative velocity difference between the fluid and the particles, it results in lateral particle motion. This is modeled by equation 3.15.

$$\mathbf{F}_\ell = -C_\ell\rho_f\pi r_p^2(\mathbf{u}_p - \mathbf{u}_f) \times (\nabla \times \mathbf{u}_f) \quad (3.15)$$

The coefficient of proportionality, C_ℓ , is estimated as $C_\ell = 0.59\alpha^{0.25}$. The added

mass force (\mathbf{F}_a), also known as the virtual mass force, comes from the amount of mass in addition to that naturally belonging to the particle which is displaced due to the particles motion. This additional mass causes the particle to behave slightly heavier than its natural weight, as such the added mass tends to resist particle acceleration in any direction, essentially its a resistive force acting to dampen the particles motion. The added mass force is modeled as seen in equation 3.16.

$$\mathbf{F}_a = -(1/2)\rho_f \nabla_p \left(\frac{D\mathbf{u}_p}{Dt} - \frac{D\mathbf{u}_f}{Dt} \right) \quad (3.16)$$

The added mass force uses the standard added mass coefficient of 1/2 which has been experimentally determined. The pressure force is that on particles due to the localized pressure gradients.

$$\mathbf{F}_p = -\nabla_p \nabla p \quad (3.17)$$

These forces comprise those taken into account through two-way coupling, i.e. the momentum transfer between the fluid and particles. In some flows these will be the dominant factors in determining the flow characteristics, in other flows the collision forces can become the dominant characteristic facilitator.

As discussed in the literature review, the effect of particle-particle and particle-wall collisions on the carrier phase flow and particle dispersion depends greatly on the flow properties, in particular the mass loading within the domain and the Stokes numbers of the particles. The inter-particle collisions are taken into account using the method of Cundall and Strack (1979) [53]. The force exerted on a particle

due to a collision is given by:

$$\mathbf{F}_{jp}^{P-P} = (k_c \delta_{pj}^{3/2} - \eta_c (\mathbf{u}_p - \mathbf{u}_j) \cdot \mathbf{n}_{pj}) \mathbf{n}_{pj} \quad (3.18)$$

$$\text{where: } \delta_{pj} = (r_p + r_j + \alpha) - d_{pj} \quad (3.19)$$

where k_c is the stiffness parameter, η_c is the damping parameter, e is the coefficient of restitution and α is the force range. Here, \mathbf{n}_{pj} is the unit vector in the direction connecting the particle centers of particles p and j , r_p and r_j are the radius of particles p and j , d_{pj} is the distance between particle centers. $P - P$ denotes the particle to particle momentum transfer, pj denotes the momentum transfer from particle p to particle j , η_c and α are computed as follows:

$$\eta_c = 2\alpha \sqrt{\frac{m_p k_c}{1 + \alpha^2}} \quad (3.20)$$

$$\alpha = -\ln(e/\pi) \quad (3.21)$$

Collisions between particles and walls are taken into account in a similar manner to the inter-particle collisions as the dominant physics of the process are analogous.

$$\mathbf{F}_{jw}^{P-W} = (k_c \delta_{pw}^{3/2} - \eta_c (\mathbf{u}_p) \cdot \mathbf{n}_{pw}) \mathbf{n}_{pw} \quad (3.22)$$

$$\text{where: } \delta_{pw} = (r_p + r_j + 2\alpha) - d_{pw} \quad (3.23)$$

Following the inter-particle equations, F_{jw} denotes the force imparted on the particle by the wall and d_{pw} is the distance between the particle center and the wall.

Chapter 4 – Particle-laden Slot Nozzle Jet

This case gives the results of a two dimensional particle-laden jet issuing from a slot nozzle into an ambient fluid.

Table 4.1: Particle-laden Jet Case - Computational Parameters

Parameter	Value
Fluid Viscosity (μ)	$1.76 \times 10^{-5} \text{ kg/ms}$
Fluid Density (ρ_f)	1.0 kg/m^3
Particle Density (ρ_p)	2500 kg/m^3
Particle Diameter (d)	$65 \text{ }\mu\text{m}$
Outlet Width (w)	0.004 m

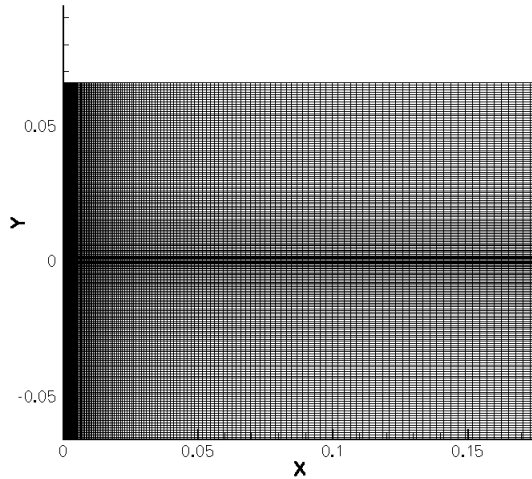


Figure 4.1: A cross section of the grid used for the short domain case. There is no jet inlet or dump region to distance the convective outlet from the region of interest in the flow.

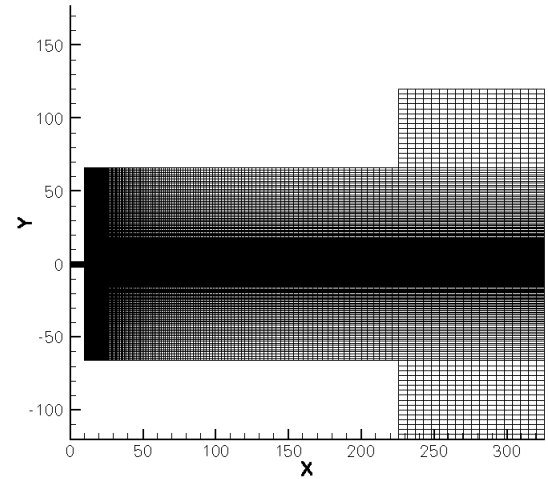


Figure 4.2: A cross section of the grid used for the extended domain case. The slot provides a true inlet condition and the dump region separates the region where measurements occur from the outlet boundary.

A two-way coupling simulation was ran to seek insight into the mechanics

of the flow. Properties of the both the gas and particle phases are examined and results are presented below. In figure 4.3, the gas phase mean centerline velocity as a function of downstream distance non-dimensionalized by the nozzle width is presented. The simulation results are in excellent agreement with both experimental data from two previous studies and computational work done by Yuu et al. (2001) [60]. The spread of the jet is the cause for the decrease in mean centerline streamwise velocity, this spread is presented in figure 4.4. The gas phase RMS velocities are intimately related to the spread of the particles from their initially unidirectional trajectory. The streamwise and lateral carrier phase RMS velocities are presented in figures 4.7 and 4.8.

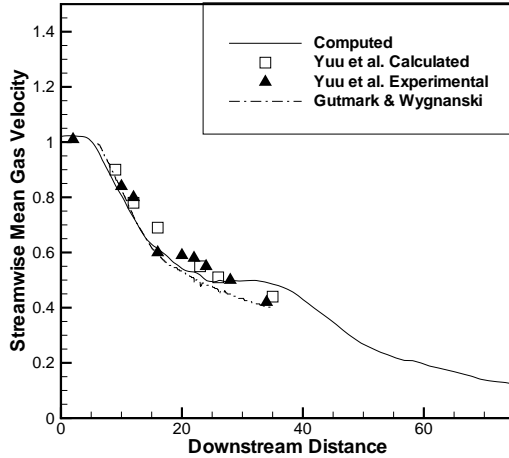


Figure 4.3: Mean streamwise gas velocity versus downstream distance along the centerline of the jet.

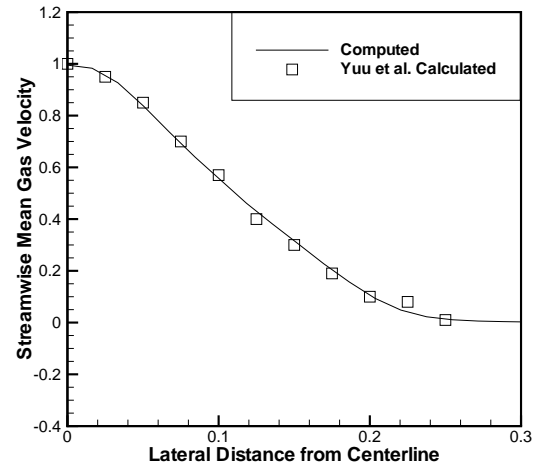


Figure 4.4: Mean streamwise gas velocity vs lateral distance from the centerline of the jet.

It seems that the reason for the discrepancy in computed RMS velocity values

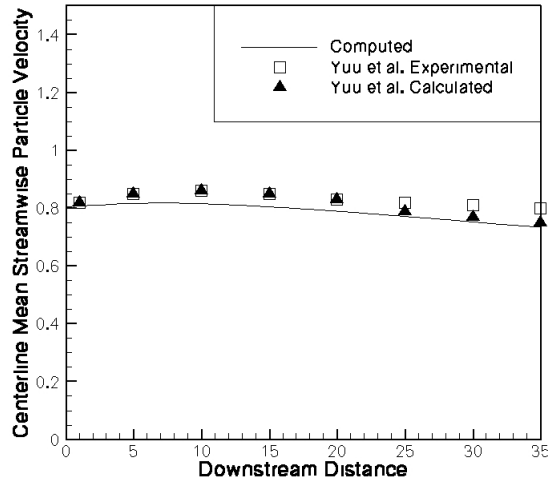


Figure 4.5: Mean streamwise particle velocity vs downstream distance along the centerline of the jet.

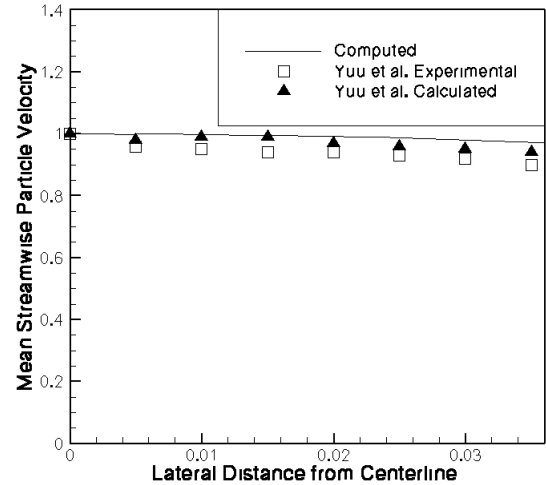


Figure 4.6: Mean streamwise particle velocity vs lateral distance from the centerline of the jet.

between this work and that of Yuu et al. is the difference in the domains used. In the study of Yuu et al. a short computational domain similar to that of figure 4.1 was used. The convective outlet boundary is adequate in a sense, but its proximity to the outlet is a likely source of error [60]. It was contended that the error is there, but relatively minimal, but when using essentially the same domain this study found significant issues propagating their way upstream. The convective outlet sparked a pressure head that slowly pushed its way back towards the jet outlet and caused artificially enhanced particle dispersion properties and enlarged RMS velocity values. A longer domain with a dump region was constructed and is shown in figure 4.2 to alleviate this problem. While marginally more computationally expensive, the result was significant. The convective outlet effects did not

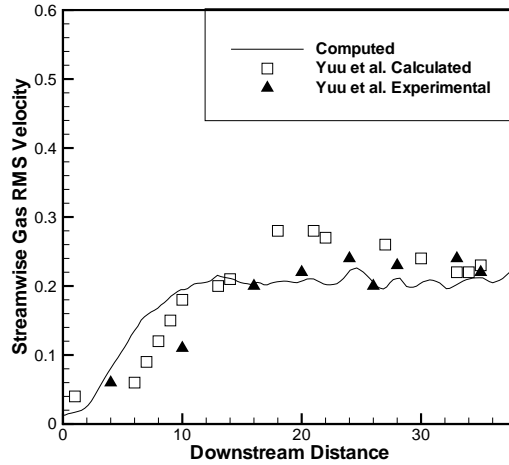


Figure 4.7: *Streamwise gas RMS velocity vs downstream distance along the centerline of the jet.*

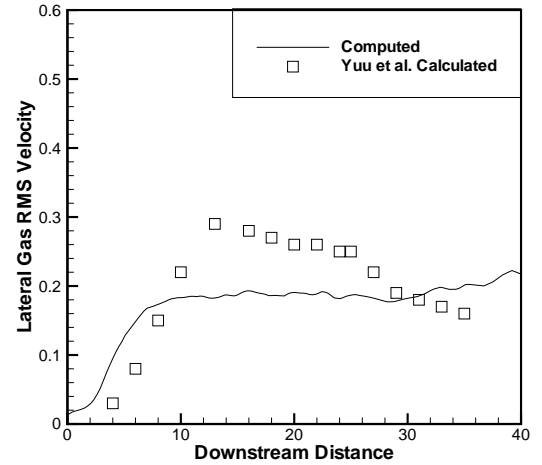


Figure 4.8: *Lateral gas RMS velocity vs downstream distance along the centerline of the jet.*

propagate to any reasonable proximity into the test section of the jet.

The convective outlet effects were largely seen in the RMS velocities of the jet centerline as seen in the afore-mentioned figures as well as figure 4.9. It is not entirely clear why these effects would be significant close to the jet centerline, but not as predominant at lateral distances away from the centerline.

Lateral profiles were difficult to match to the experimental data precisely because the downstream distance at which the measurements were taken was not provided. In general the similarity property of the jet would prevent such problems but it seems that the presence of particle causes enough of a disturbance that profiles only compare well at non-dimensional distances $X/D > 20$.

Additional experimental data is provided by the studies by Gutmark and Wyg-

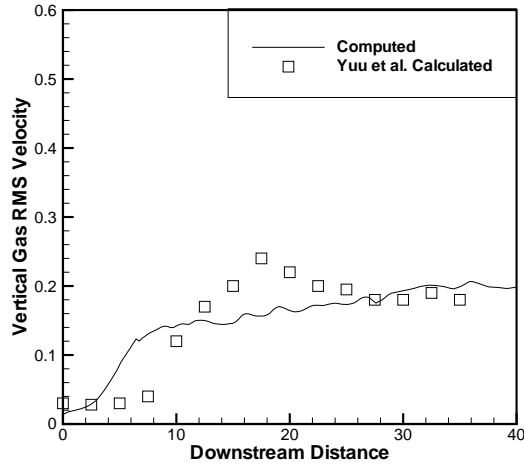


Figure 4.9: *Vertical gas RMS velocity vs downstream distance along the centerline of the jet.*

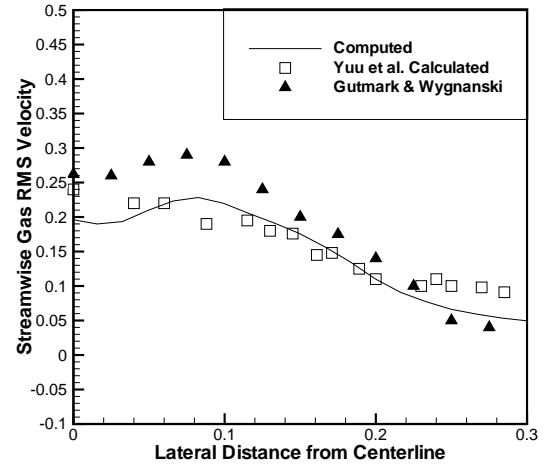


Figure 4.10: *Streamwise gas RMS velocity vs lateral distance from the centerline of the jet.*

nansky (1976) and (1978) with which to gain confidence in these results [61] [62]. One particularly beneficial property found was the ability of large-eddy simulation using two-way coupling to properly predict the Reynolds stresses as seen in figure 4.13. Accurate knowledge of the Reynolds stress tensor is a key component in future modeling efforts for larger scale projects, especially those using the Reynolds averaged Navier-Stokes type models which rely heavily on knowledge of the behavior of this tensor.

Particle statistics proved significantly more difficult to reproduce under the current conditions. It is conjectured that the difference in injection method between our computational methodology and their experimental method is the likely case. More accurate results would require more information about the initial distribu-

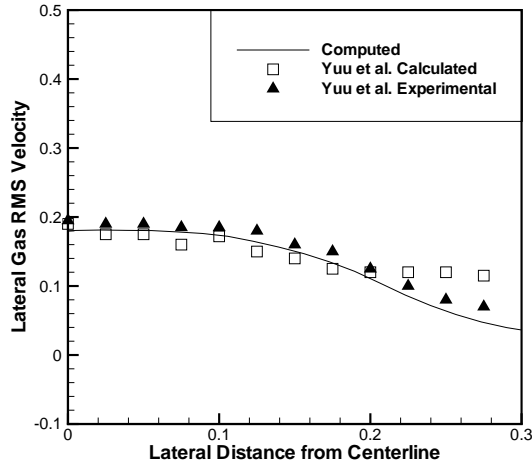


Figure 4.11: *Lateral gas RMS velocity vs lateral distance from the centerline of the jet.*

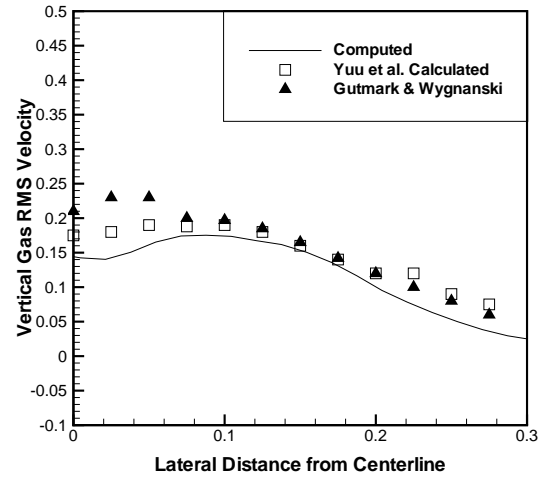


Figure 4.12: *Vertical gas RMS velocity vs lateral distance from the centerline of the jet.*

tion of the particle phase. In their experiment the nozzle is placed so it protrudes into the domain yielding different boundary conditions. The nozzle itself is also contracting which would add a lateral component to the particle velocity which is not present in the initial conditions for these computations. Lastly, the particles themselves are not as well behaved initially, or quite randomly placed due to the preferential injection. These factors make it very difficult to determine how well the model handles particle dispersion because it seems almost assuredly the case that the initial conditions will play a dominant factor in this behavior.

The conclusion from this study is that large-eddy simulation using the dynamic Smagorinsky model and two-way coupling was able to reproduce experimental results accurately. The use of the outlet dump region had an effect on the predicted

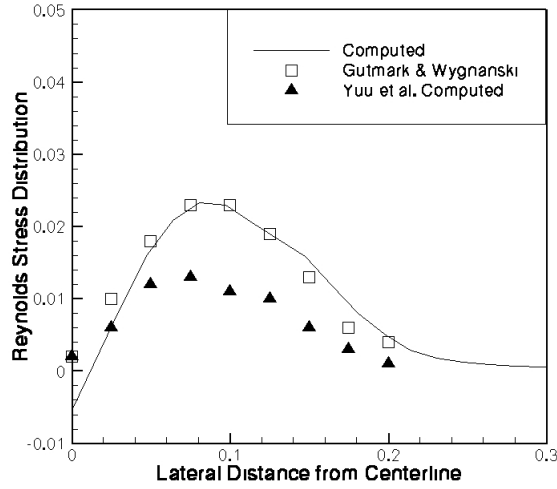


Figure 4.13: *Reynolds stress distribution vs lateral distance from the centerline of the jet.*

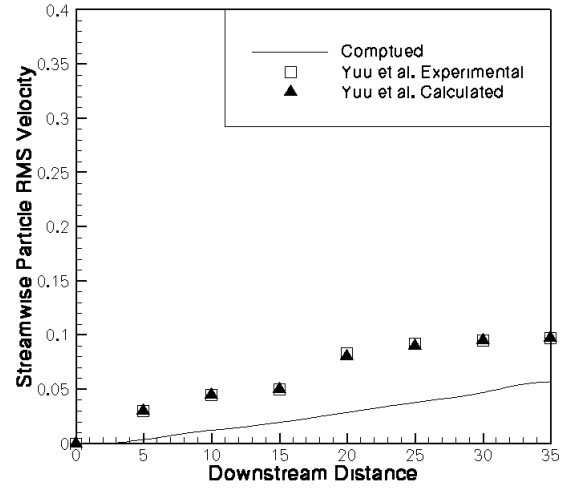


Figure 4.14: *Streamwise particle RMS velocity vs downstream distance along the centerline of the jet.*

flow field and allowed a full set of statistics to be collected, whereas in other work the simulation was stopped prematurely and had a short collection domain due to the outlet error propagation. The increased outlet region provides improved predictions of jet and particle statistics.

Chapter 5 – Preliminary Test Cases Using Volumetric Coupling

Table 5.1: Motivational Cases

Case:	Density Ratio (ρ_p/ρ_f)	Mass Loading (m)
Bubble-Vortex Interaction	0.001	< 0.001
Jet Fluidization	1993.6	797.4
Slurry Flow	10.0	1.59
Rayleigh-Taylor Instability	7.23	0.27
Gravitational Settling	1993.6	398.7

In this work a variety of scenarios are examined to see how volumetric coupling affects the carrier and particle phase properties compared to other modeling techniques. It is important to understand that the lowest Stokes number particles will exert a smaller reaction force on the fluid than a higher Stokes number particle. This gives an indication of how significant the effect of two-way coupling is as a function of Stokes number. In addition to this, it is intuitive that the effect of two-way coupling would scale with mass loading. Since this work focuses on a particle-laden channel flow it is important to discuss the motivation for this work, consider the continuity equation in the volumetric coupling model:

$$\frac{\partial}{\partial t}(\rho_f \Theta_f) + \nabla \cdot (\rho_f \Theta_f \mathbf{u}_f) = 0 \quad (5.1)$$

Using volumetric coupling, when a particle leaves a cell there is an influx of fluid to fill the void left by the particle. In addition to this, the new cell in which the particle is contained has an outflux of fluid in order to make room for the particle. What this means is that even for an incompressible fluid, the flow is

not locally divergence-free. The conservation of mass equation accounting for the presence of particles can be written as:

$$\nabla \cdot \mathbf{u}_f = -\frac{1}{\Theta_f} \left(\frac{\partial}{\partial t}(\Theta_f) - \mathbf{u}_f \cdot \nabla(\Theta_f) \right) \quad (5.2)$$

Equation 5.2 relates the divergence in the fluid flow field to the fluid volume fraction. It is not immediately clear exactly when the effect of having a local divergence in the flow field will have an effect on the fluid statistics or particle motion, or if an effect is present, just how significant it will be. It seems reasonable to expect that the effect of divergence on the fluid phase flow field will be significantly larger in the near wall region than near the channel centerline. The divergence within the flow field will be instantaneous with the motion of each particle, since this amounts to instantaneous fluctuations in the gas phase there would be some expected increase in near wall rms velocities. This may have an effect on particle motion and dispersion. A few cases are presented here to see how the volumetric coupling approximation can differ from the two-way coupling approximation and how in some circumstances, virtually no difference is found.

Table 5.1 shows the fluid to particle density ratios and mass loadings for the five systems that will be examined here. Particular attention should be paid to how the density ratio, mass loading and dominant flow forces change the variation due to volumetric coupling.

5.1 Bubble-Vortex Interaction

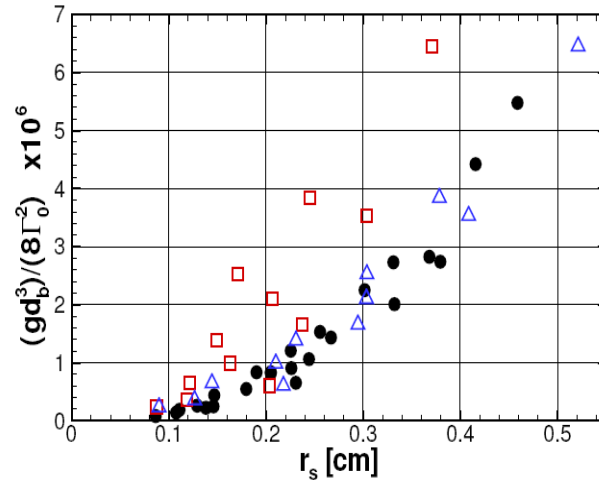


Figure 5.1: *The non-dimensional settling location of the bubbles. ● experimental data from Sridhar & Katz, □ one-way and two-way coupling, △ volumetric coupling.*

In the case of a bubble being released to interact with a traveling vortex studied by Finn et al. (2010), a significant difference was found when the volumetric coupling approximation was employed [71] [72]. Figure 5.1 shows a summary of some results from cases ran featuring bubble-vortex interaction. The settling location of the released bubbles is of primary concern in this study and the results show the significant differences that arise from implementing the different collision models. The volumetric coupling results are very well in line with the experimental results of Sridhar and Katz (1999) [73]. The two-way coupling approximation is

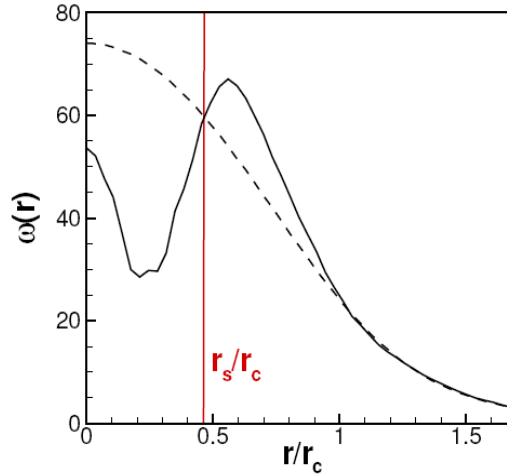


Figure 5.2: *Radial vorticity distribution as a function of distance from the centerline. The solid line is the distribution for the volumetric coupling approximation and the dashed line is from the two-way coupling approximation.*

not capable of reproducing these features.

Figure 5.2 shows the radial vorticity distributions as a function of distance from the core. The vertical line is the average bubble settling radius for the case. The vorticity near the center of the core is drastically reduced under the volumetric coupling approximation. As seen in figure 5.1 these effects are important to the prediction of settling location for this type of physical system. The two-way coupling effect was unable to predict the vortex distortion observed in the experiments by Sridhar & Katz. This effect was only captured by accounting for the volumetric coupling effect.

5.2 Jet Fluidization

In this case an array of particles are aligned in a rectangular box with a small jet centered on the bottom wall. This highlights how two-way and volumetric coupling can produce very different results. The inter-particle repulsion force collision model is applied for both the two-way and volumetric coupling cases. Figure 5.3 shows a series of snapshots of particle positions in time for the case when two-way coupling is used. Using two-way coupling the only interaction between the particle and the fluid phases is momentum transfer. Particle displacement propagates itself towards the top of the pile with time but no void is generated by the issuing jet. Figure 5.4 shows the velocity vector propagation in time. Note the nearly vertical direction of the velocity vectors when two-way coupling is used.

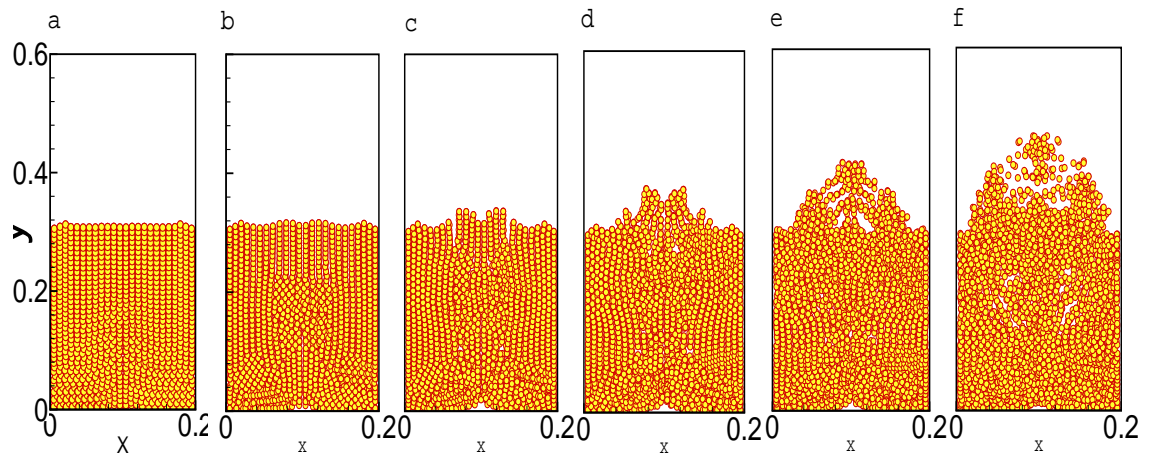


Figure 5.3: *Snapshots in time of particle locations under the two-way coupling approximation.*

Figure 5.5 shows a sampling of cross sectional images in time when volumetric

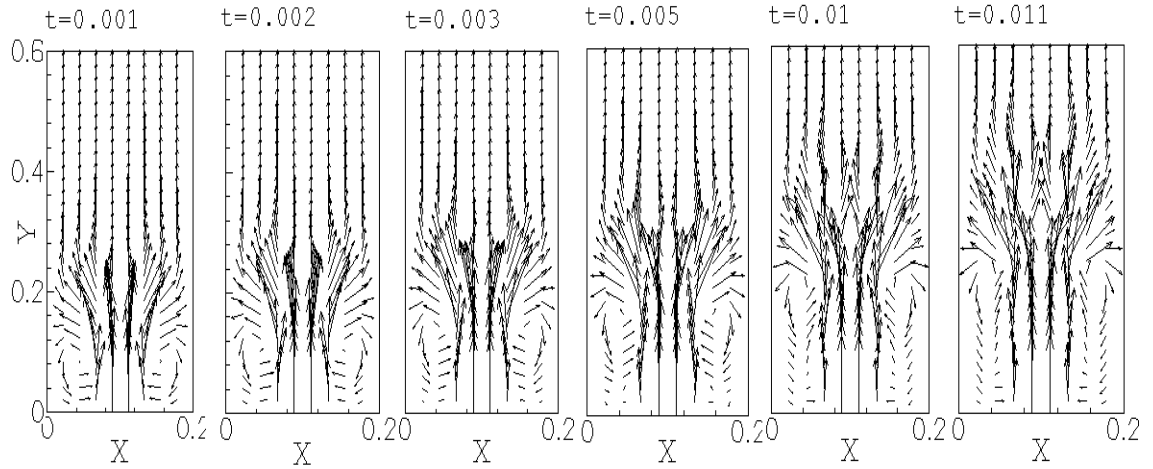


Figure 5.4: Snapshots of velocity vectors in time using the two-way coupling approximation.

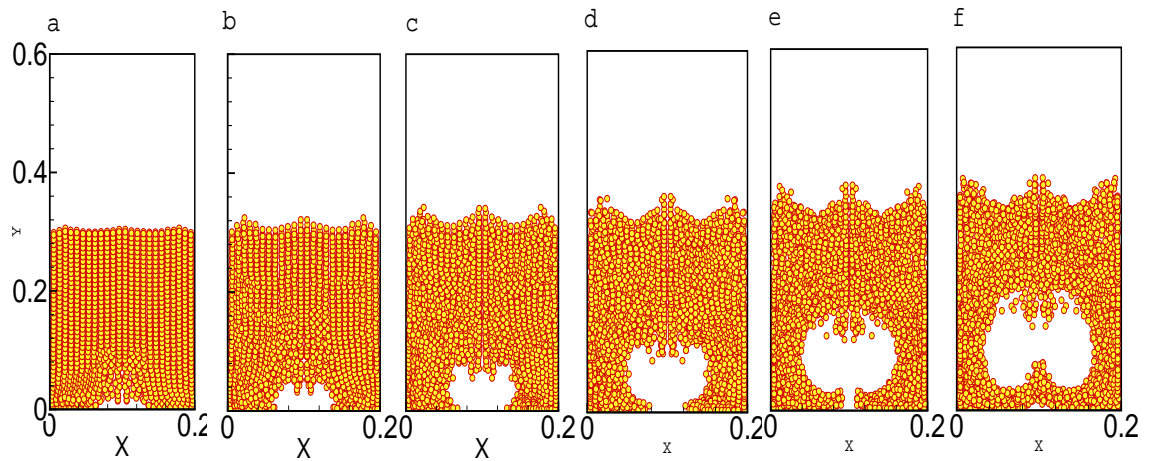


Figure 5.5: Snapshots in time of particle locations under the volumetric coupling approximation.

coupling is employed. Note the void that is created under this coupling approximation, which is not present under two-way coupling. The differences in the velocity

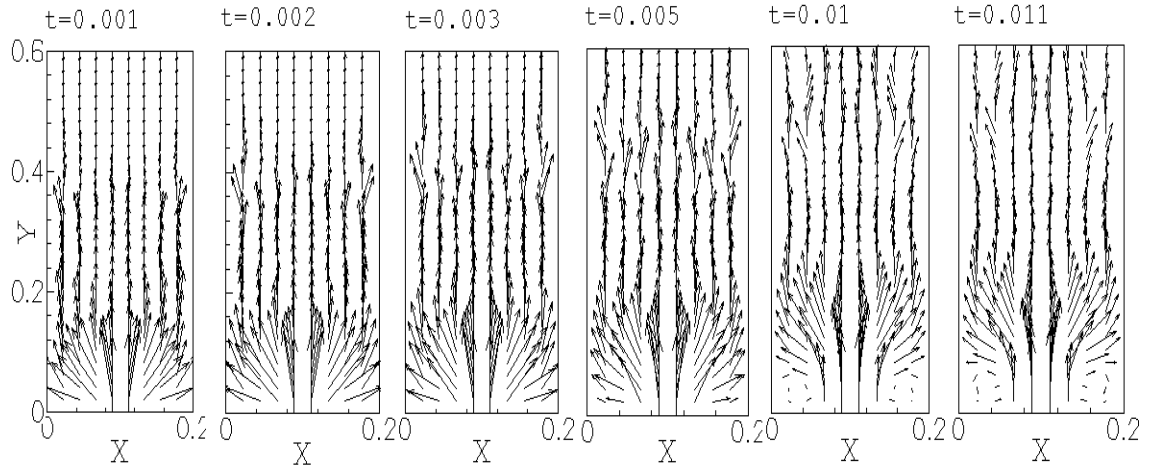


Figure 5.6: *Snapshots of velocity vectors in time using the volumetric coupling approximation.*

vectors are clear as seen in figure 5.6. The particles displace a significant enough amount of mass that the gas velocity is changed drastically.

Figures 5.7 and 5.8 show the axial pressure gradient and kinetic energy profiles as a function of distance from jet exit. Note the large difference in the axial pressure gradient. The differences in particle motion causes drastic differences in both the flow statistics and the visual features of the system. The deceleration of the flow by running into the collection of particles yields the change in axial pressure gradient, this does not occur under the two-way coupling approximation since the jet is not forced out away from the centerline in the same manner.

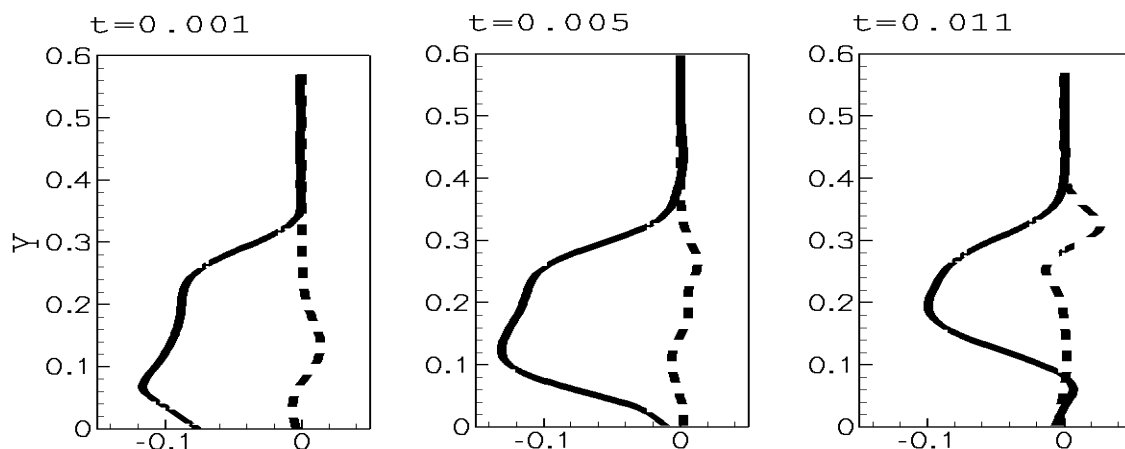


Figure 5.7: Normalized axial pressure gradient along the centerline of the jet. The solid line represents the results from volumetric coupling approximation and the dashed line the two-way coupling results.

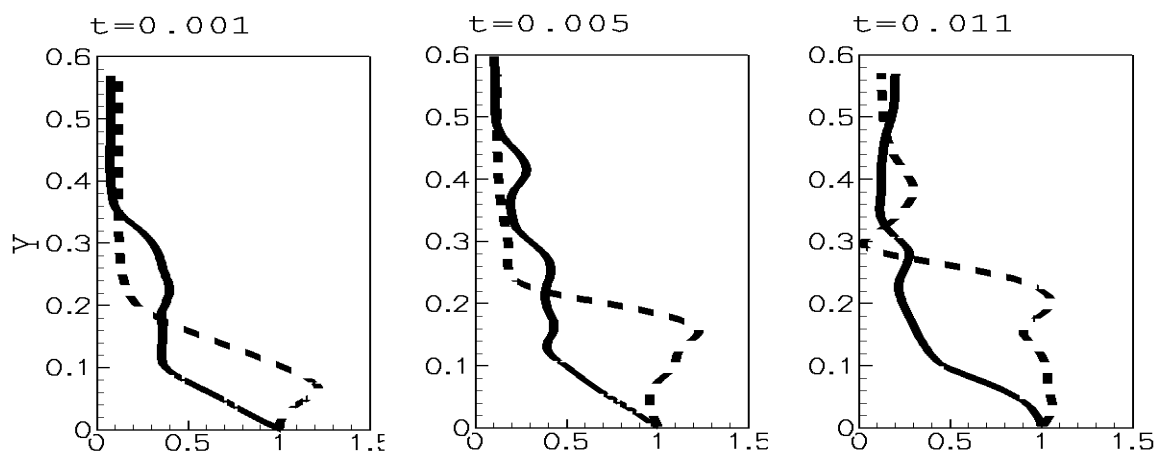


Figure 5.8: Normalized kinetic energy along the centerline of the jet. The solid line represents the results from volumetric coupling approximation and the dashed line the two-way coupling results.

5.3 Slurry Flow

One flow of particular interest is that of a coal slurry flow or transport of sedimentation on the bottom of a river bed. Previous studies have approached problems like this using direct numerical simulation [74]. A parabolic velocity profile is initiated in the channel with an array of particles aligned on the floor of the channel. Figure 5.9 shows the result of a combination of interphase momentum exchange and the effect of the displaced mass on the system.

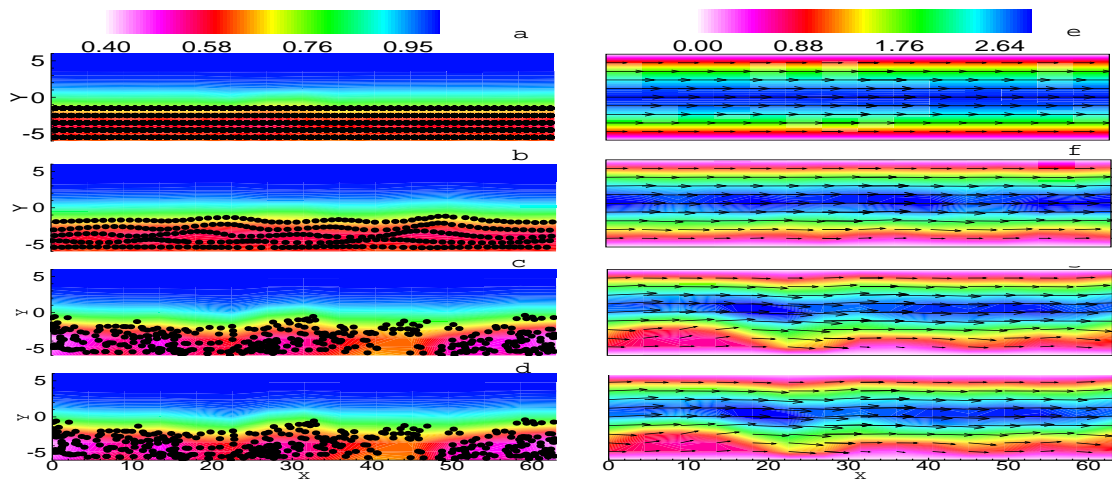


Figure 5.9: *Figures (a-d) show the particle locations and contours of volume fraction. Figures (e-h) show gas phase velocity vectors and contours of streamwise velocity.*

Figure 5.10 shows the mean particle volume fraction as a function of height within the channel as time develops. The lift on the particles is seen through the increasing volume fraction above the initial height. The continuous decrease in volume fraction is due to the interpolation scheme detailed in appendix A.

The gas phase rms velocities in the streamwise and wall-normal directions are

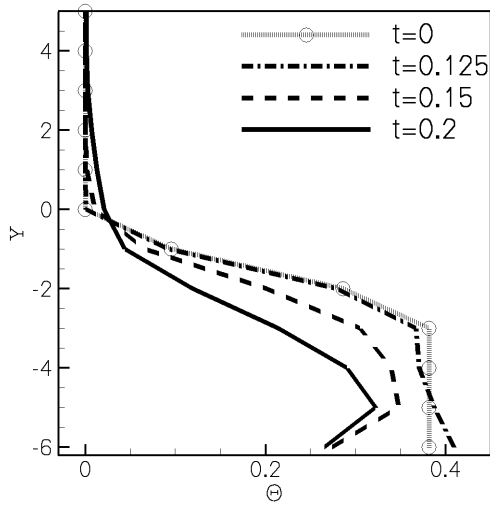


Figure 5.10: *Particle volume fraction using the finite volume approach.*

shown in figure 5.11. The finite-size formulation generates results which are in good agreement with previously published data, whereas two-way coupling does not accurately assess the lift due to fluidization within the channel.

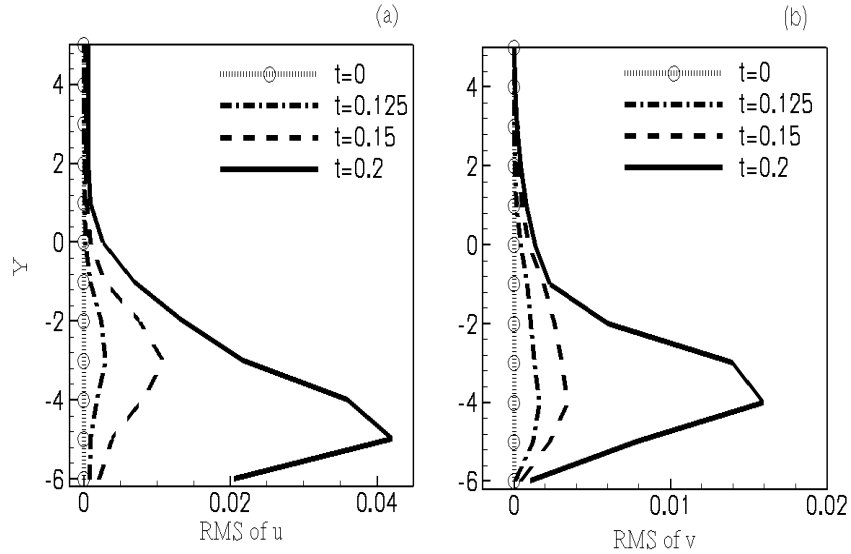


Figure 5.11: (a) *Streamwise gas rms velocity.* (b) *Wall-normal gas rms velocity.*

5.4 Rayleigh-Taylor Instability

In the case of a Rayleigh-Taylor instability studied by Shams & Apte (2007) [75], a collection of particles are initialized at the top of a rectangular box. The particle radius is $3250 \mu m$, $\rho_p = 1.225 kg/m^3$ and $\rho_f = 0.1694 kg/m^3$. A cosine wave is used to perturb the interface between the fluid and particle front. The domain is subject to the gravity force and the particles are then allowed free motion.

Figure 5.12 shows how a filtered particle volume fraction contour map evolves with time. The results from using the two-way coupling approximation and volumetric coupling approximation are nearly identical. At this mass loading and Stokes number the effect of accounting for the displaced fluid is negligible.

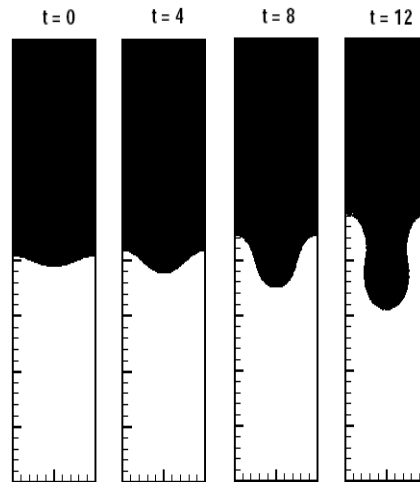


Figure 5.12: *Time progression of falling particle locations.*

5.5 Gravitational Settling

In this case a small rectangular box contains 1000 particles randomly distributed within it. The particles themselves are $500 \times 10^{-6} m$ in diameter, in this study however a feature of the code that allows one particle to represent many is utilized, each “particle” is really a parcel of 3375 particles of the same size. The parcel has an effective diameter of $7.5 \times 10^{-3} m$. The density ratio of the particle to the gas is about 2000 : 1. Gravity is the only force on the box, all original motion is due solely to this.

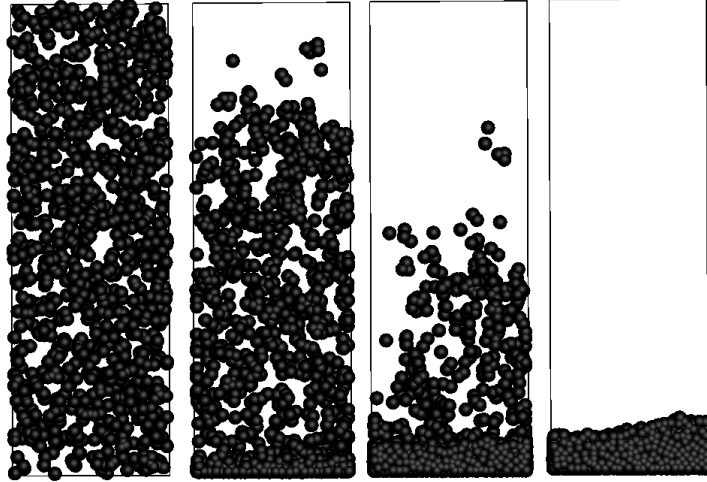


Figure 5.13: *Progressive Falling Particle Images*

Figure 5.14 shows the height of the particle pile as a function of time. The analytical solution given is the expected dropping time for an object released. It is found by using equation 5.3.

$$h = 0.6 - \frac{1}{2}gt^2 \quad (5.3)$$

This expected settling time is an excellent predictor for flows in which inter-particle collisions are not taken into account, however when considering collisions it takes longer as the bottom most particles hit the wall and bounce back up causing a chain reaction. The particles initially take up 20% of the volume of the domain. Once settled the pile has a volume fraction just over 0.6 which is physically desirable as it is near the close packing limit. Figure 5.13 depicts the

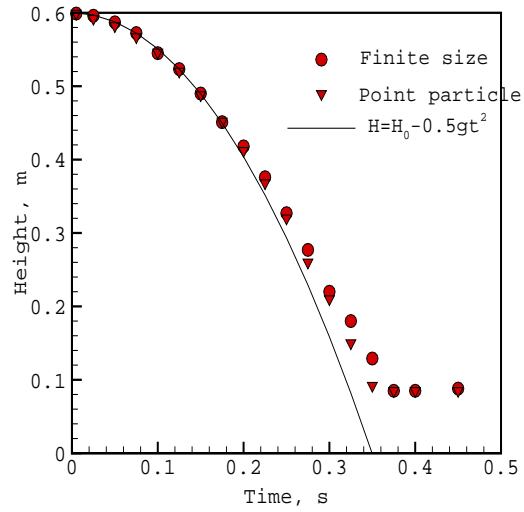


Figure 5.14: *Particle pile height as a function of time.*

process of particles falling and beginning to pile. It is clear that the inclusion of finite-size effects are not relevant to this scenario. The Stokes number and mass loading of the flow cause momentum transport and inter-particle collisions to be the dominant mechanisms in the flow.

Chapter 6 – Particle-laden Channel Flow

6.1 Problem Description and Setup

In this case a particle-laden channel flow is studied using large-eddy simulation. Designed after the work of Yamamoto et al. (2001) [2], this work investigates the effect of particle mass loadings and coupling method on this channel flow. In most particle-laden flow simulations the Reynolds number based on the wall slip velocity and the channel half width is around 180. In this case we are studying a much higher turbulent Reynolds number flow of 644. This yields a mean flow Reynolds number of approximately 13,000. Particle mass loadings for this study have a range varying from 0.01 to 5.

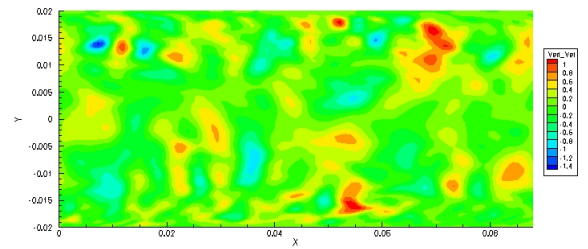
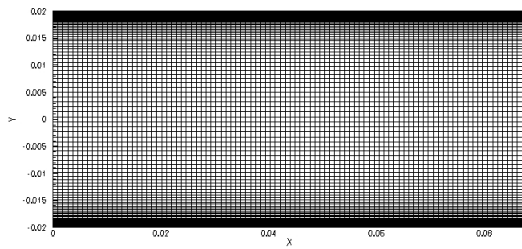


Figure 6.1: *Cross section of the turbulent channel flow mesh used in this work.*

Figure 6.2: *Instantaneous snapshot of a vertical gas phase velocity from a case in this work.*

The channel simulation domain has a streamwise length of 0.088 m with a gap of 0.04 m between the plates and a lateral length of 0.03 m . Periodic boundary conditions are placed on the streamwise boundaries to allow the flow to become fully developed without the use of an extensively large computational domain. Such a domain would result in protracted computational times. In general the fully developed profile is considered the major concern as the flow becomes fully

Table 6.1: Particle-laden Channel - Computational Parameters

Parameter	Value
Computational Domain	0.088 <i>m</i> x 0.04 <i>m</i> x 0.03 <i>m</i>
Fluid Viscosity (μ)	1.5 x 10 ⁻⁵ <i>kg/ms</i>
Fluid Density (ρ)	1.0 <i>kg/m³</i>
Reynolds Number (Re_τ)	644
Mass Loading (m)	0.01 - 5.0
Stokes Number (St)	0.89 - 70

developed within a rather short distance in comparison with the total channel length in most applications. Periodic boundaries are also utilized on the lateral boundaries to allow for wall-normal effects to be the predominant factors on the flow. A traditional no-slip boundary condition is applied for the gaseous phase at the wall and the particles are subjected to specular reflection.

In the studies of Yamamoto et al. [2] the channel is forced using a constant pressure gradient (CPG) forcing method. With some knowledge of the expected flow field, the expected wall shear stress τ_w for example, the wall-slip velocity u_τ can be calculated.

$$u_\tau = \left(\frac{\tau_w}{\rho} \right)^{1/2} \quad (6.1)$$

In order to determine the appropriate forcing for the flow, it is required that the shear stress at the walls balance out the pressure driven forcing. A body force equal to the pressure gradient required to drive the channel is applied to the flow field. The necessary body force can be calculated using the equation below.

$$(\text{Domain Volume}) * b_x = (\text{Wall Surface Area}) * \tau_w \quad (6.2)$$

Thus in a pure gas flow the desired body force is derived directly. The extension to particle-laden flows however is more complicated. Following the method of Yamamoto et al. (2001), a correction factor may be added to the original balance equation to account for the effect of adding dense particles to the flow [2].

$$(\text{Domain Volume}) * b_x = (\text{Wall Surface Area}) * \tau_w + Nm_p\bar{g} \quad (6.3)$$

The presence of particles is now accounted for by adding in the force of N particles on the flow field. This works well for low mass loading cases. However, there are some unintended consequences at higher mass loadings which cause some difficulty in establishing a desirable flow field, such as achieving a similar mass flow rate. In some ways it brings up the more philosophical issue of what exactly constitutes the same flow field when a variable such as the particle mass loading has been varied.

6.2 Validation of Work

The first case that will be examined is the lowest mass loading (m) case, corresponding to a mass loading of $m = 0.01$. In this case $28 \mu m$ particles with a density (ρ_p) of 700 kg/m^3 , which corresponds to a Stokes number (St) of 0.89 for this flow, are injected into a fully developed single phase flow field to shorten the de-

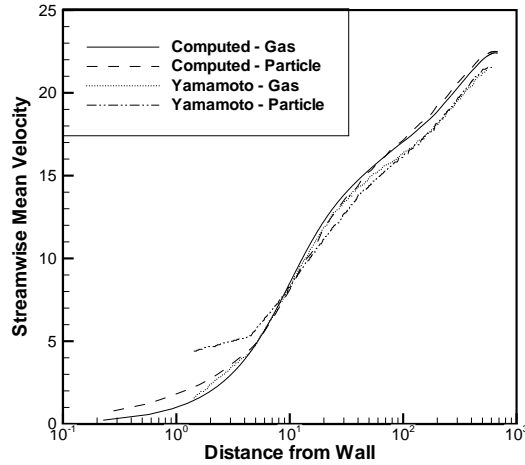


Figure 6.3: *Case 1: Mean Streamwise Gas and Particle Velocities*

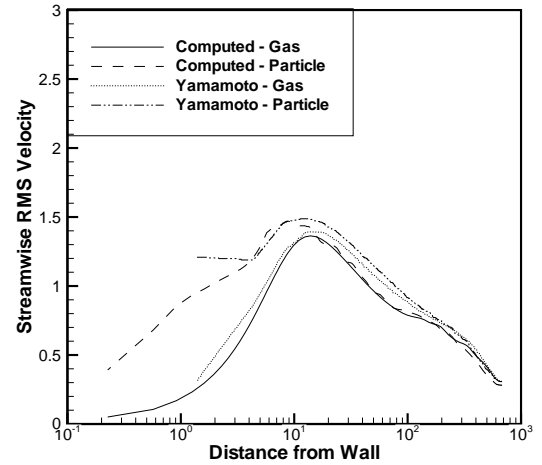


Figure 6.4: *Case 1: RMS Streamwise Gas and Particle Velocities*

velopment time. These particles are meant to reflect the properties of lycopodium particles after the experiments of Kulick et al. (1994) [63]. Flow properties such as streamwise momentum, wall-slip velocity and bulk flow rate are tracked to determine when the new particle-laden flow has become fully developed. These are the smallest Stokes number particles studied and as expected, their behavior very similarly to the carrier phase flow field is obtained. Figure 6.3 shows that there is a slight trend for the particles to have a faster streamwise velocity closer to the channel centerline than the fluid due to the effect of gravity on the particles, since their density is more than two orders of magnitude higher than that of the air. This effect is not pronounced and adds little energy to the particles and produces very little in the way of additional turbulent intensity, as can be seen in figure 6.4. The one deviation from this occurs near the wall where the particle velocities, both

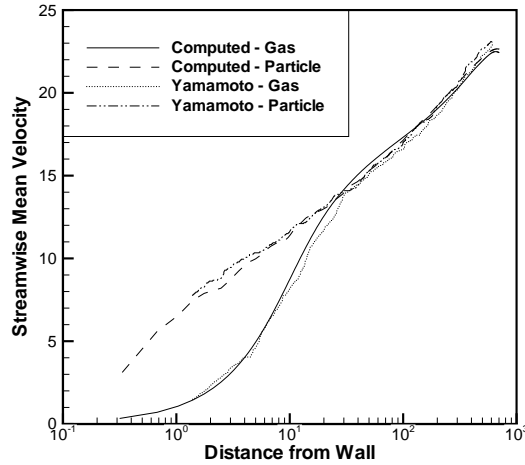


Figure 6.5: Case 2: Mean Streamwise Gas and Particle Velocities

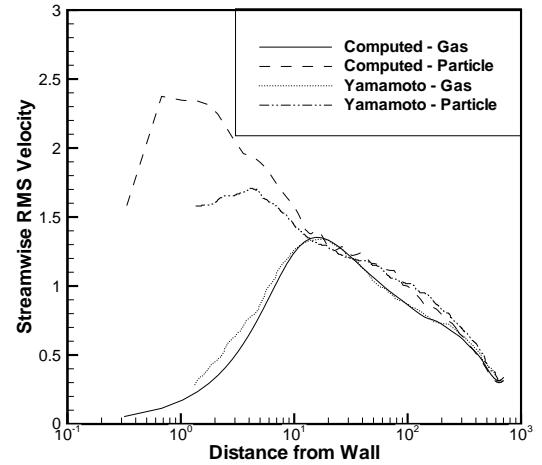


Figure 6.6: Case 2: RMS Streamwise Gas and Particle Velocities

mean and RMS, are higher than that of the surrounding fluid. This is because the particles are not subject to the no-slip condition and as such do not lose all their momentum near the wall. They do lose a substantial amount due to drag from the fluid phase as the fluid phase is much slower than the mean flow.

Similar trends can be seen in the second test case. In this case $50 \mu m$ particles with a density of $2500 \text{ kg}/m^3$ and a Stokes number of 10 are injected into the flow to yield a particle mass loading of 0.2. These particles are made to reflect the properties of glass beads. The main trends in this case are qualitatively the same as the trends in the previous case. The particles still generally reflect the mean flow characteristics but tend to deviate near the wall as is shown in figure 6.5. The particle RMS velocity near the wall, which is shown in figure 6.6 is most likely artificially enlarged in comparison with that of the established results due to an

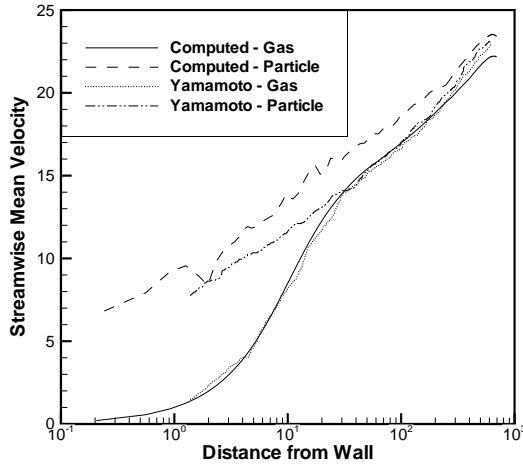


Figure 6.7: Case 3: Mean Streamwise Gas and Particle Velocities

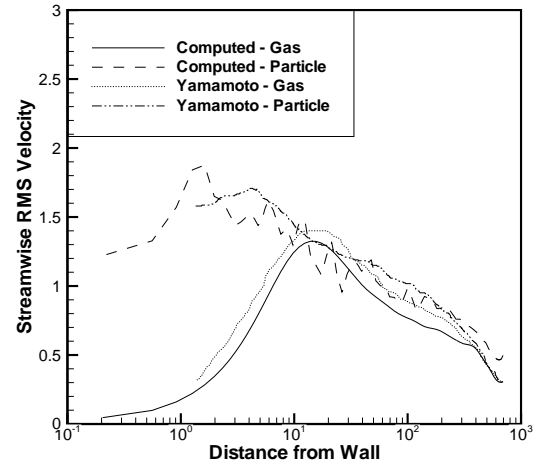


Figure 6.8: Case 3: RMS Streamwise Gas and Particle Velocities

unphysically large repulsion force from the wall. The authors make no mention of their method for handling particle-wall collision in the “collision-free” case, but it seems likely that they implemented an inelastic reflection condition of some sort. The difference in the handling of these properties can lead to significantly different near wall properties. The difference is more pronounced in this case as the particles have larger inertia in comparison to those in the most dilute case. The deviation here is far larger in the wall region, but due to the low volume loading only has a minimal effect on the mean flow profile as will be seen later.

The third case varies only slightly from the second in that the mass loading is kept at 0.2, but the particles are changed (copper) and have a density of 8800 kg/m^3 and a diameter of $70 \text{ }\mu\text{m}$, giving them a Stokes number of 70. The effect of gravity on the particles becomes more pronounced here as we would expect, this is

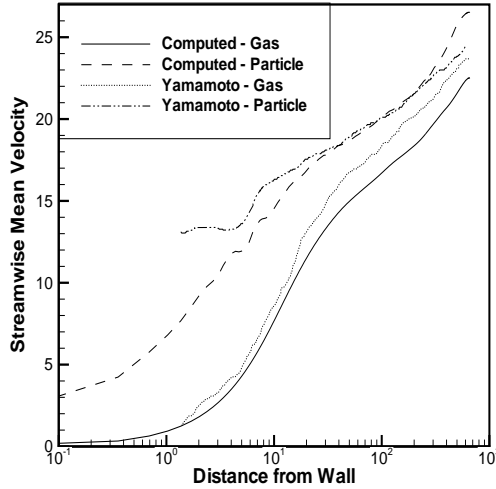


Figure 6.9: *Streamwise Mean Velocity for the case when $m = 1$ and $St = 70$.*

reflected in the mean particle velocity in figure 6.7. Modification to the overall gas phase profile is still relatively weak as is expected, and the particle RMS velocity values are reminiscent of the previous case due to the similar mass loadings and Stokes numbers on the same order of magnitude. See figures 6.6 and 6.8 for this effect.

We see in figure 6.10 the particle volume fractions of the varying cases normalized by their average values. The first thing to note is that the pattern of particle concentrations is very similar in all cases. This is desirable because the mass loading of these cases is not sufficient for the turbulent structure, which is the dominant mechanism of particle transport for all cases of sufficiently low mass loading, to be significantly altered by the presence of the particles. In other words,

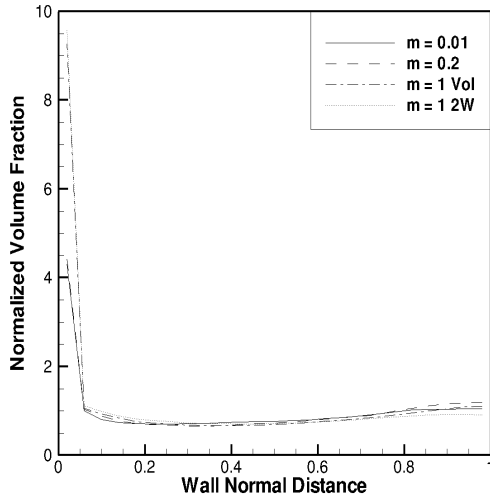


Figure 6.10: *Normalized Particle Volume Fraction vs Wall Normal Distance.*

at these mass loadings the overall turbulent structure is still strongly reminiscent of the clean gas flow. This is important because at higher mass loadings the features change to the point that the mechanisms may change, however at these levels the similarity is strong enough for these results to be sensible. The near wall collecting of particles is a feature observed in many turbulent studies. This gives confidence that the fluid fluid solver is behaving properly and accurately calculating particle motion for the flow.

6.3 Forcing Method

To proceed, a forcing method which allows changing mass loadings and still maintains a constant flow rate is necessary. Until now all flow rates have appeared

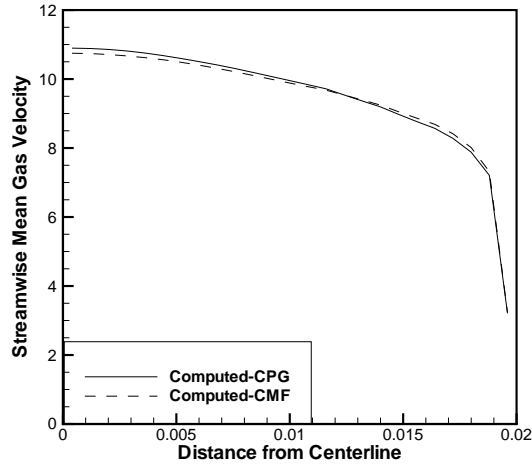


Figure 6.11: *CPG vs. CMF Forcing, Mean Flow Velocity for the case when $m = 0.01$ and $St = 0.89$*

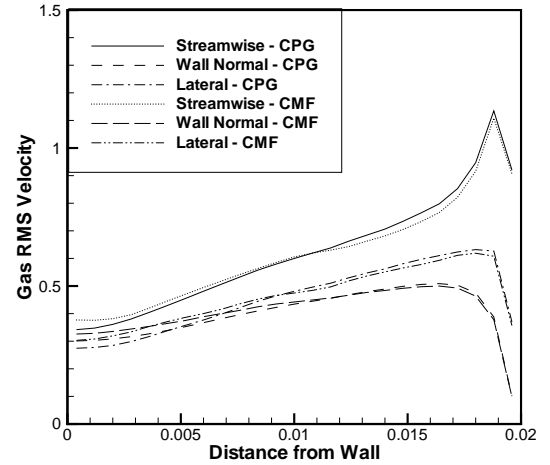


Figure 6.12: *CPG vs CMF Forcing, RMS Velocity for the case when $m = 0.01$ and $St = 0.89$*

relatively constant despite the results from Yamamoto et al. [2] including the additional forcing from the second term in equation 6.3, while the results computed for this work do not. This is because the contribution of the extra term has been negligible thus far. The bulk velocity for the clean air flow, and roughly for the low particle mass loading flows, has been about 9.5 m/s . Two much higher mass loading cases have been used to test the validity of equation 6.3 beyond dilute flows and some issues were found. While the additional term provides a qualitatively proper adjustment to the required body force, it is not quantitatively correct and yields large flow rate errors at higher loadings. The results of a simulation ran with a particle mass loading of 5 showed that the inclusion of the full effect of the second term yields a bulk velocity upwards of 20 m/s from which point it has

easily become intractable by the grid currently being used. If the second term in equation 6.3 is ignored the bulk velocity is brought down to roughly 6 m/s , which is also very undesirable. This means that constant pressure gradient forcing may not be the proper method to proceed with.

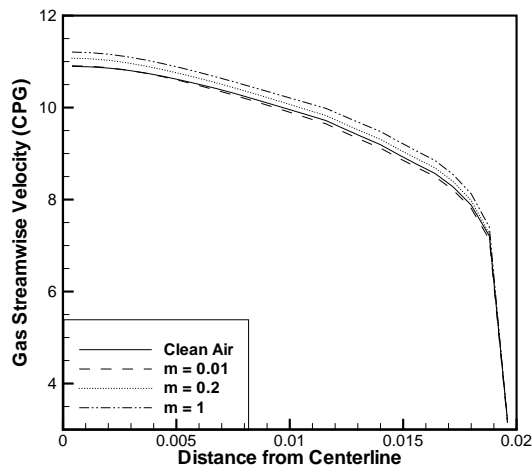


Figure 6.13: *Mass Loading Effect on Mean Velocity Profile (CPG) for the case when $m = 1$ and $St = 70$*

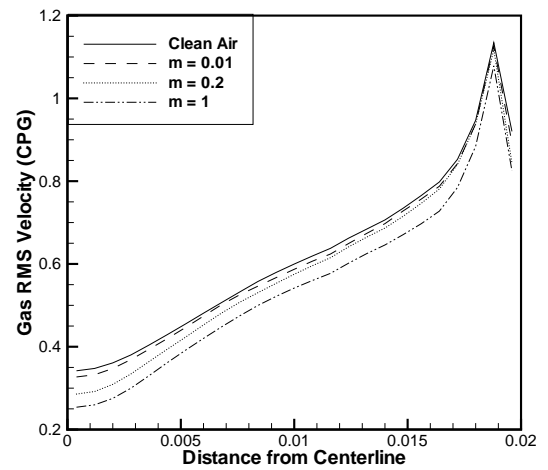


Figure 6.14: *Mass Loading Effect on RMS Velocity Profile (CPG) for the case when $m = 1$ and $St = 70$*

In this next case, the same copper particles from case three are used, but in 5 times the quantity, yielding a mass loading of 1 for this flow. Figure 6.9 shows large discrepancies in the flow field results when two different pressure gradients are used to force the channel. Using the forcing method of equation 6.3 Yamamoto et al. (2001) finds a bulk velocity that is significantly larger than that of the original clean air flow or any of the lower mass loading cases. Figure 6.13 shows a clear discrepancy in bulk velocity between the lower and higher mass loading flows.

Figures 6.13 and 6.14 show a major facet of how constant pressure gradient forcing affects a flow field. In this simulation both the mean flow and gravity are oriented in the same direction, as such they compliment each other. In two-way coupling several things are happening, one of which is very important here. Let us assume we are entering time step n of our simulation and this is the first step in which gravity will be turned on. As step n is entered the velocity of the particles is calculated explicitly from the old carrier phase velocity field information. At this point it is reasonable to assume that the streamwise velocity of the particles will be close to the local streamwise velocity of the gas near the channel centerline. However, if the effects of gravity are included in this time step, the particle will be slightly faster than the surrounding fluid. Once the particle positions are updated based on their new velocities, the two-way coupling force is calculated. This force determines the local momentum transfer from the particles onto the fluid due to the motion of the particle and the no-slip boundary condition around its exterior. This quantity is modeled in this study since the boundary layer surrounding the particle is not resolved. At some point here the effect of particle to fluid momentum transfer begins to produce an enlarged fluid velocity. This continues to accelerate until a balance is reached between the additional drag produced by the accelerated flow and the additional force generated by the falling particles. The intent of 6.3 was to account for effects like these, but it would seem the interaction between the two terms on the right hand side is not very straightforward.

Now a different method is used. To enforce a constant mass flow (CMF) rate the force of drag on the walls is dynamically calculated each time step and that

amount is redistributed among the flow field to maintain the desired flow rate. This has the advantage of guaranteeing the carrier phase flow has the same flow rate for all loadings, however this has some drawbacks as well, although none as problematic as constant pressure gradient forcing.

Using this constant mass flow rate forcing method one of the original test cases is repeated. It should be no surprise that for clean air flow, both methods essentially find the same results. In figures 6.11 and 6.12 the mean and RMS turbulent profiles have been adequately reproduced using the constant mass flow rate method.

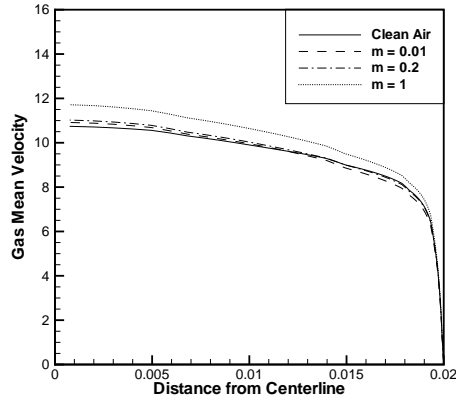


Figure 6.15: Mean streamwise gas velocity for varying mass loadings ran with two-way coupling and neglecting the effect of collisions.

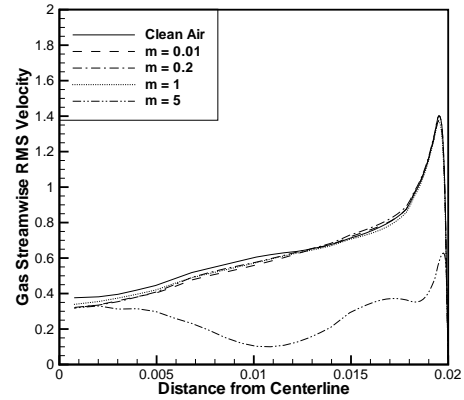


Figure 6.16: Streamwise RMS gas velocity for varying mass loadings ran with two-way coupling and neglecting the effect of collisions.

6.4 Mass Loading

One major feature in turbulence modeling of particle-laden flows is how the mass loading affects the turbulent structures and statistics. This section provides results for cases ran with two-way coupling without a collision model for mass loadings that vary from 0.01, which is essentially the same as clean gas for gas phase statistics, up to 5. Figure 6.15 shows the mean gas velocity profile for the varying cases, the increase in centerline velocity is due to the force of gravity on the particles dragging the gas phase with them. The streamwise gas rms velocity is shown in figure 6.16, the magnitude of the rms velocity dampens with increasing mass loading.

Figures 6.17 and 6.18 show the gas phase wall-normal and lateral rms velocities. Both of these figures show the same features as the streamwise rms velocities, moderate damping at lower mass loadings and significant damping at moderate

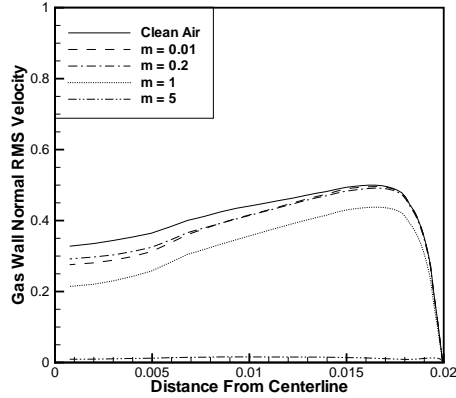


Figure 6.17: *Wall-normal RMS gas velocity for varying mass loadings ran with two-way coupling and neglecting the effect of collisions.*

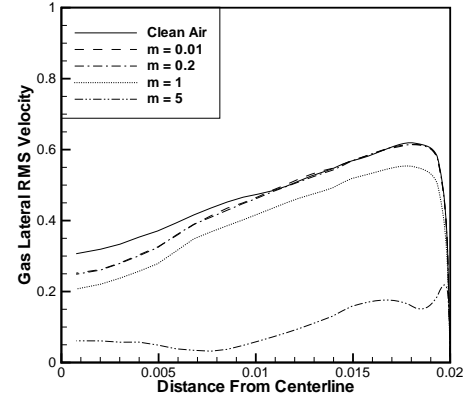


Figure 6.18: *Lateral RMS gas velocity for varying mass loadings ran with two-way coupling and neglecting the effect of collisions.*

mass loadings. The largest attenuation occurs in the wall normal direction. Without collisions the momentum transfer from the streamwise direction to the wall normal direction is absent.

The mean particle velocity is shown in figure 6.19. The increasing centerline velocity with increased mass loading is evident. Increased local volume fraction of particles significantly influences gas phase statistics. The more the gas phase is influenced, the less drag is exerted on the particles, thus they can accelerate to higher velocities. The limit of this process occurs when the mass flow rate must be balanced, so the body force becomes limited to prevent the flow from accelerating too far. Figure 6.20 shows the particle streamwise rms velocities. The particle rms values increase with mass loading, this is likely due to a stricter mean due to the higher particle influence, this yields a larger rms particle velocity. This is true

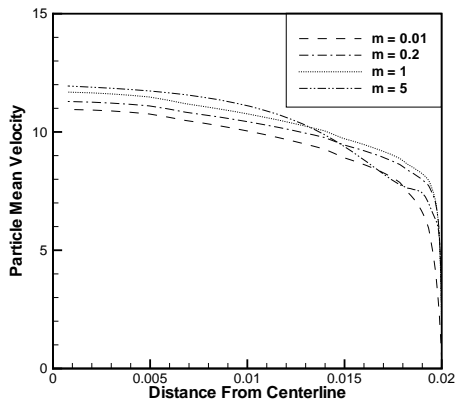


Figure 6.19: Mean streamwise particle velocity for varying mass loadings ran with two-way coupling and neglecting the effect of collisions.

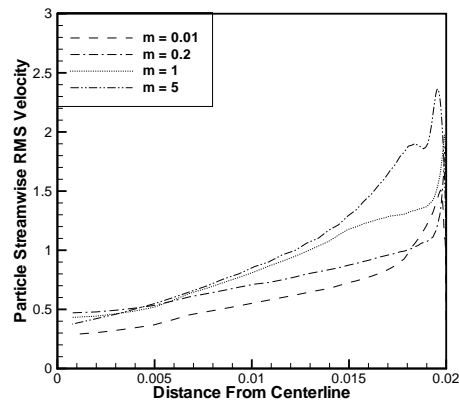


Figure 6.20: Streamwise RMS particle velocity for varying mass loadings ran with two-way coupling and neglecting the effect of collisions.

because of the continuous forcing in the streamwise direction.

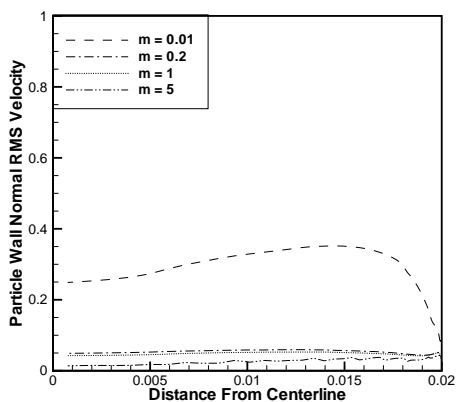


Figure 6.21: Wall-normal RMS particle velocity for varying mass loadings ran with two-way coupling and neglecting the effect of collisions.

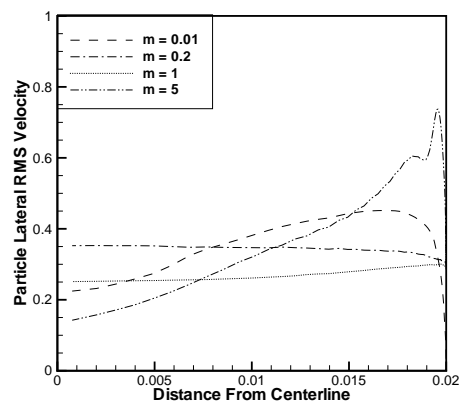


Figure 6.22: Lateral RMS particle velocity for varying mass loadings ran with two-way coupling and neglecting the effect of collisions.

The wall-normal particle rms velocities are shown in figure 6.21. The wall-normal rms velocities are sharply attenuated with mass loading. The reasoning for this is much the same as with the gas phase. The lateral rms velocities are shown in figure 6.22 and show no discernable pattern.

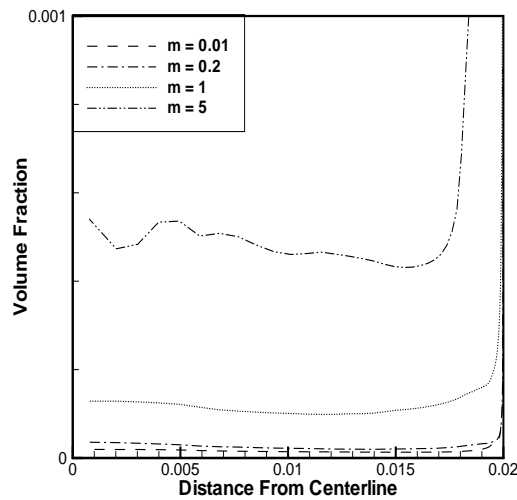


Figure 6.23: *Wall-normal volume fraction profile for varying mass loadings ran with two-way coupling and neglecting the effect of collisions.*

The particle volume fraction is shown in figure 6.23. The distribution pattern is the same in all cases as the dominant mechanism for particle distribution does not change. The only change is the magnitude of the volume fraction which is directly proportional to the mass loading.

6.5 Statistics

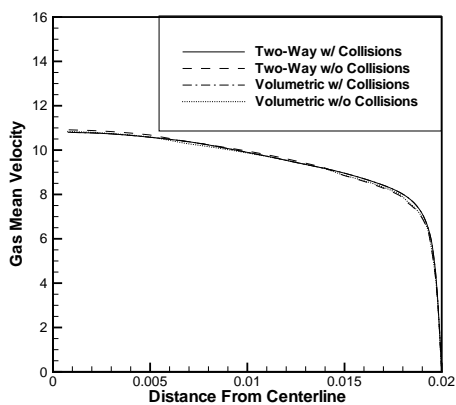


Figure 6.24: Mean streamwise gas velocity for $m = 0.01$, with the coupling and collision method indicated in the legend.

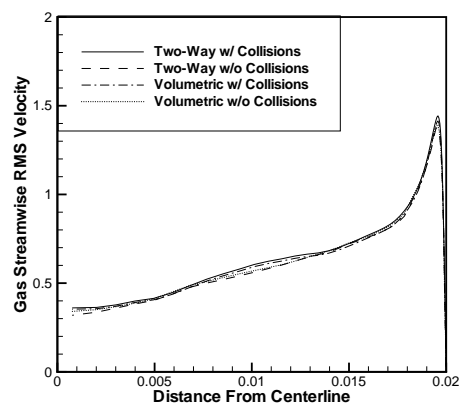


Figure 6.25: Streamwise RMS gas velocity for $m = 0.01$, with the coupling and collision method indicated in the legend.

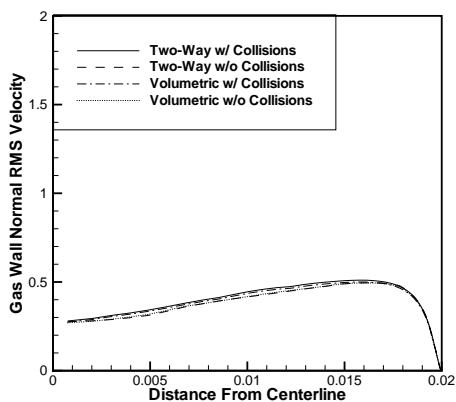


Figure 6.26: Wall-normal RMS gas velocity for $m = 0.01$, with the coupling and collision method indicated in the legend.

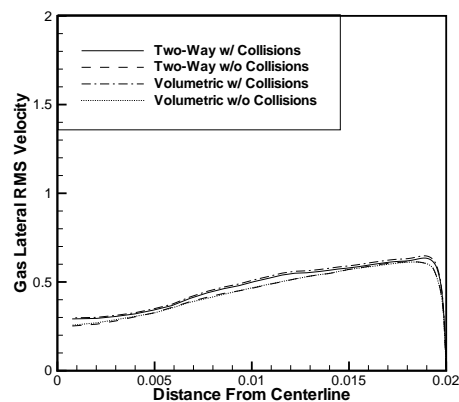


Figure 6.27: Lateral RMS gas velocity for $m = 0.01$, with the coupling and collision method indicated in the legend.

The turbulent gas and particle statistics are the primary method of distin-

guishing the effect of various models or assumptions for particle-laden flows. In this section the results of utilizing two-way and volumetric coupling each with and without collisions models are analyzed for mass loadings of 0.01 and 1. While this is the most common way of analyzing the flow structures, other methods of comparison will be used in the proceeding sections.

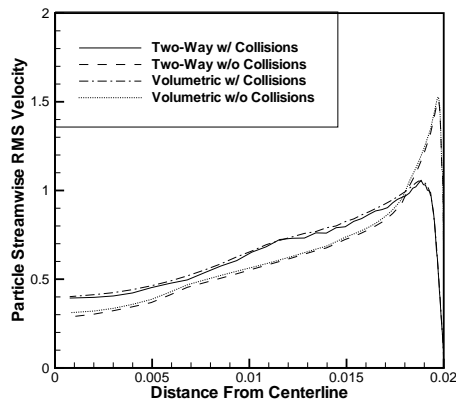


Figure 6.28: *Streamwise RMS particle velocity for $m = 0.01$, with the coupling and collision method indicated in the legend.*

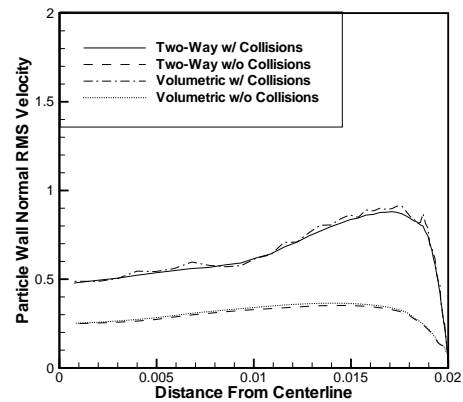


Figure 6.29: *Wall-normal RMS particle velocity for $m = 0.01$, with the coupling and collision method indicated in the legend.*

Figure 6.24 shows the mean streamwise gas velocity using the four combinations of coupling and collision models for the low mass loading case where $m = 0.01$. There is only a negligible difference between the predicted velocities as would be expected. The streamwise gas rms velocity has the same feature, there is virtually no effect from changing the coupling method or the collision model. This is shown in figure 6.25.

Figures 6.26 and 6.27 show the wall-normal and lateral gas phase rms velocities respectively. There would seem to be a slight difference in gas phase rms velocity

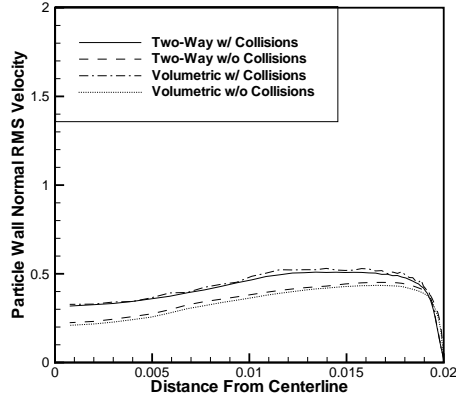


Figure 6.30: *Lateral RMS particle velocity for $m = 0.01$, with the coupling and collision method indicated in the legend.*

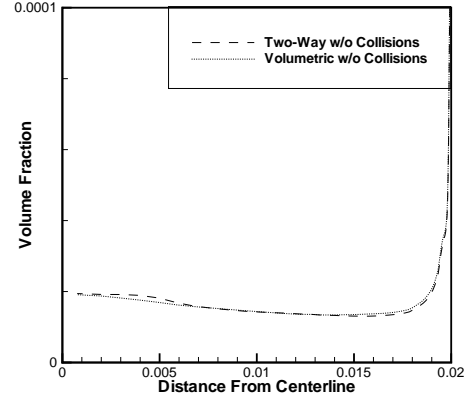


Figure 6.31: *Wall-normal volume fraction profile for $m = 0.01$, with the coupling and collision method indicated in the legend.*

when the collision model is implemented, however no effect is seen. The coupling method does not show any real change in the gas phase.

The streamwise particle rms velocities are shown in figure 6.28. The collision model shows a damped near wall rms velocity but a higher centerline rms velocity in comparison with the case when collisions are neglected. Figure 6.29 shows the wall-normal particle rms velocity. The collision model increases the rms velocity values dramatically in comparison with collisions being neglected. The coupling model once again shows little to no effect.

The same pattern holds in figure 6.30 for the streamwise and wall-normal directions. The lateral particle rms velocities show higher rms velocities. The wall-normal volume fraction profile is shown in figure 6.31, no real difference in particle concentration occurs when the coupling method is changed.

Figure 6.32 shows the streamwise energy spectra for the varying coupling

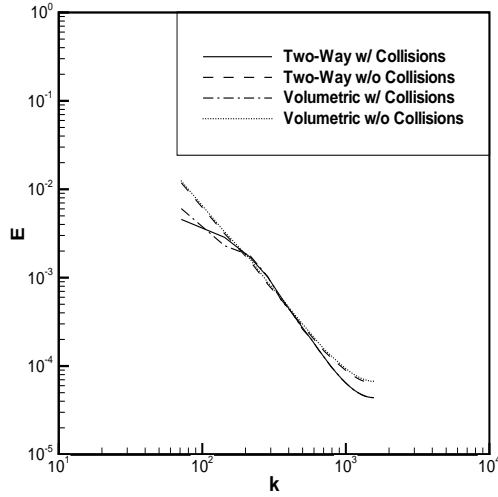


Figure 6.32: *Streamwise energy spectra versus wave number for the case when $m = 0.01$ and $St = 0.89$.*

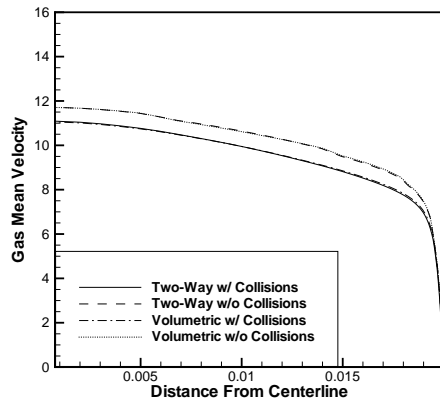


Figure 6.33: *Streamwise mean gas velocity for $m = 1$, with the coupling and collision method indicated in the legend.*

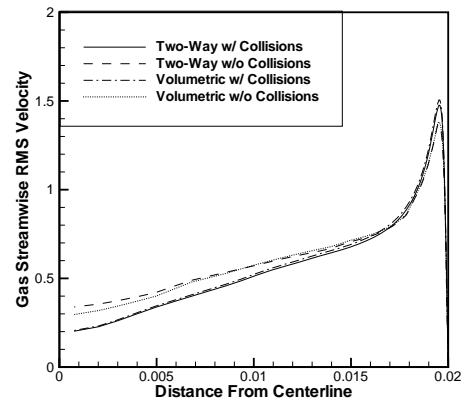


Figure 6.34: *Streamwise RMS gas velocity for $m = 1$, with the coupling and collision method indicated in the legend.*

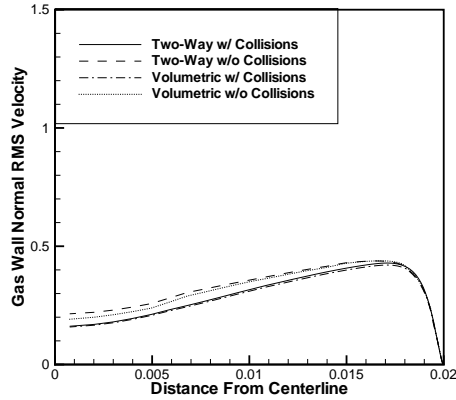


Figure 6.35: Wall-normal RMS gas velocity for $m = 1$, with the coupling and collision method indicated in the legend.

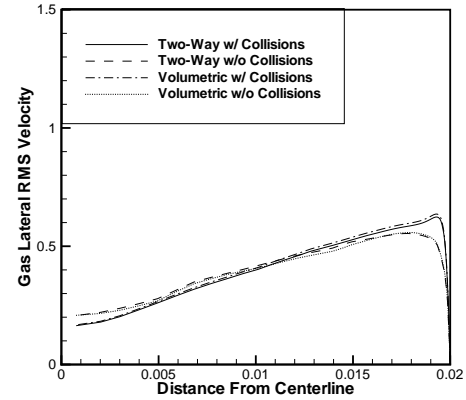


Figure 6.36: Lateral RMS gas velocity for $m = 1$, with the coupling and collision method indicated in the legend.

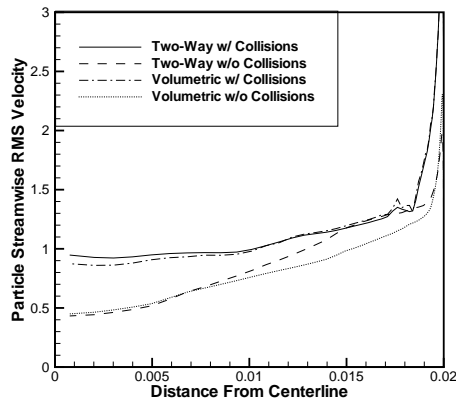


Figure 6.37: Streamwise RMS particle velocity for $m = 1$, with the coupling and collision method indicated in the legend.

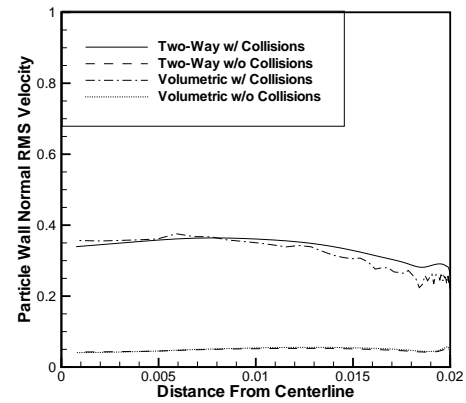


Figure 6.38: Wall-normal RMS particle velocity for $m = 1$, with the coupling and collision method indicated in the legend.

methods with and without collisions. There is a negligible difference in the energy spectra when the coupling method is altered between two-way and volumetric. A slight change occurs when the collision model is employed that appears to ex-

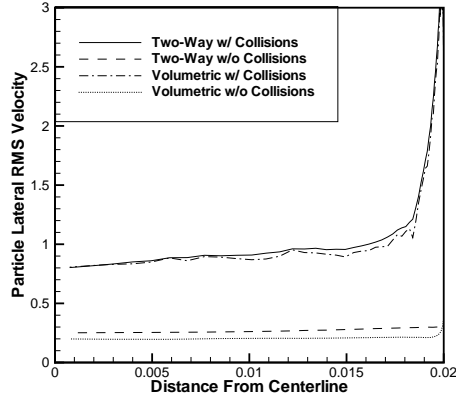


Figure 6.39: Lateral RMS particle velocity for $m = 1$, with the coupling and collision method indicated in the legend.

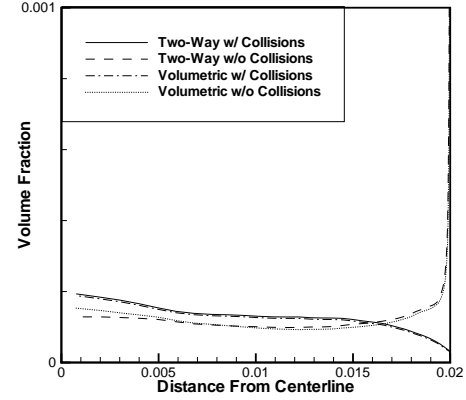


Figure 6.40: Wall-normal volume fraction profile for $m = 1$, with the coupling and collision method indicated in the legend.

tremely slightly dampen the largest scales of motion.

Figure 6.33 shows the mean streamwise gas velocity for the various coupling and collision methods for the case when $m = 1$.

The streamwise gas phase rms velocity is shown in figure 6.34. The coupling method shows no real effect while the collision model decreases the intensity.

Figures 6.35 and 6.36 show the gas phase wall-normal and lateral rms velocities respectively. The inclusion of inter-particle collisions has only a small effect at this mass loading ($m = 1$) and Stokes number ($St = 70$). The differences caused by changing the coupling model also appear negligible.

Figures 6.37 and 6.38 show the streamwise and wall-normal particle rms velocities. The effect of including collisions causes a significant increase in rms velocities in the entire domain, especially near the channel centerline where the increase is roughly five fold in the wall-normal direction.

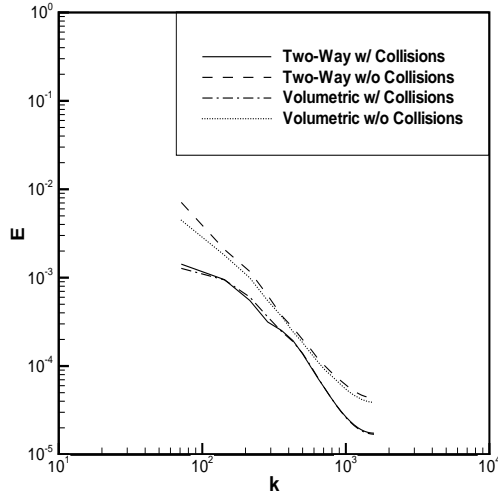


Figure 6.41: *Streamwise energy spectra versus wave number for the case when $m = 1$ and $St = 70$.*

The lateral particle rms velocity profile is shown in figure 6.39. The collision model once again shows a dramatic difference in the entire domain, especially in the near wall region. The choice of coupling method again shows little effect. The collision model redistributes the particles from the near wall region to the middle of the channel. While the collision model made a sizable difference, the choice of coupling method does not change the distribution of particles in the wall-normal direction as seen in figure 6.40. Figure 6.41 shows the streamwise energy spectra for the two coupling methods with and without collisions. The inclusion of collisions seems to universally dampen the flow at all length scales but not to a large degree. The most significant damping occurs at the largest scales as was true in the lower mass loading case.

6.6 Near Wall Structures

In some ways the near wall structures are what ultimately defines the characteristics of a turbulent wall-bounded flow. These structures are dependent on several things, including mass loading, flow rate and Reynolds number among others. Examining patterns in near wall structures and possible correlations with structures of particle positions we can learn some about these.

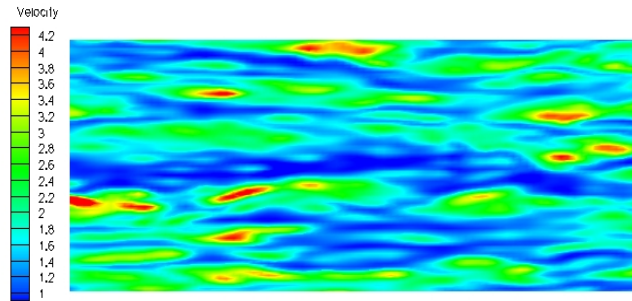


Figure 6.42: *Instantaneous gas velocity profile at a near wall plane corresponding to $y^+ = 4$ for the clean gas case ($m = 0$).*

In figure 6.42 we see the near wall streamwise velocity features. The near wall gas structures in figures 6.42 to 6.52 are taken at a wall normal distance of $y^+ = 4$, particle images are the collection of particles between $y^+ = 0$ and $y^+ = 4$. We can use 6.42 as a basis for comparison for the particle laden cases to see the effect of loading on the flows.

Figures 6.43 and 6.44 show the particle locations and near wall gas phase structure for the case with a mass loading of $m = 0.01$ consisting of $28\mu m$ diameter



Figure 6.43: *Instantaneous particle structures in the near wall region ($0 < y^+ < 4$) for the $m = 0.01$ case using volumetric coupling and neglecting the effects of collisions, with $St = 0.89$.*

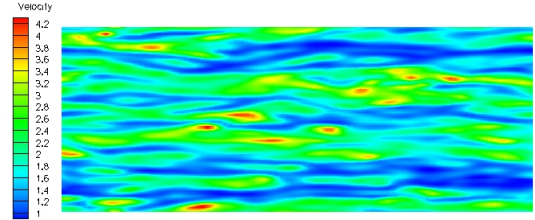


Figure 6.44: *Instantaneous gas velocity profile at a near wall plane corresponding to $y^+ = 4$ for the $m = 0.01$ case using volumetric coupling and neglecting the effects of collisions, with $St = 0.89$.*

particles. As would be expected, the near wall structures compare very well with those of the clean gas flow. The mass loading is sufficiently low to say that near wall structures are relatively unaffected by the presence of particles even when volumetric coupling is taken into account. The particles in this first case have a low Stokes number ($St = 0.7$) and so they are generally subject affected by the main flow and the local structures. Note that the three strongest streamwise particle streaks in figure 6.43 are strongly aligned with three streaks in the gas phase flow.

The possible variation in the streamwise gas phase structure is interesting in figure 6.46. These contour plots do not have the ability to obtain substantial variation from typical states. The same streamwise vortical streaks are evident in this image as they are in the clean gas case but with some modification. The streamwise vortical structures are the mechanism by which the streaks are formed, the streaks can then be strong enough to continue and self-propel or can



Figure 6.45: *Instantaneous particle structures in the near wall region ($0 < y^+ < 4$) for the $m = 0.2$ case using two-way coupling and neglecting the effects of collisions, with $St = 10$.*

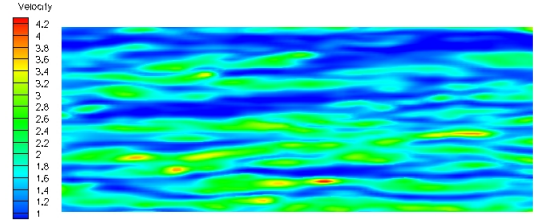


Figure 6.46: *Instantaneous gas velocity profile at a near wall plane corresponding to $y^+ = 4$ for the $m = 0.2$ case with two-way coupling and neglecting the effects of collisions, with $St = 10$.*

be maintained with the help of the momentum transfer from particles due to the effect of gravity. In the same manner as the lowest mass loading case it should be noted that the strongest streamwise streak in the near wall field is strongly aligned with streaks in the gas velocity structure.



Figure 6.47: *Instantaneous particle structures in the near wall region ($0 < y^+ < 4$) for the $m = 0.2$ case using two-way coupling and neglecting the effects of collisions, with $St = 70$.*

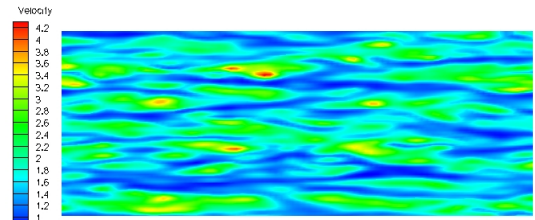


Figure 6.48: *Instantaneous gas velocity profile at a near wall plane corresponding to $y^+ = 4$ for the $m = 0.2$ case using two-way coupling and neglecting the effects of collisions, with $St = 70$.*

There is very little difference in the overall pattern of the structures in figures 6.46 and 6.48. This makes sense because they share a common mass loading with

the only variation being particle size. The reality is that the mass loadings are low enough that their effect is small anyway, and their relative sizes are close enough (less than one order of magnitude apart) that a significant deviation would not be expected. The only difference in the images is in the slight asymmetry in the case with $50\mu m$ diameter particles. The number of particles in this case is small enough that pattern recognition is not straightforward.

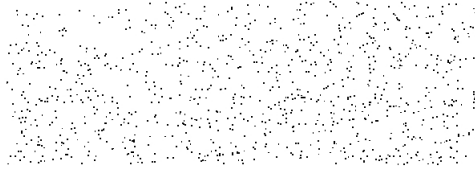


Figure 6.49: *Instantaneous particle structures in the near wall region ($0 < y^+ < 4$) for the $m = 1$ case using two-way coupling and neglecting the effects of collisions, with $St = 70$.*

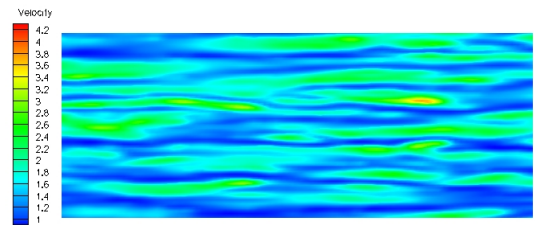


Figure 6.50: *Instantaneous gas velocity profile at a near wall plane corresponding to $y^+ = 4$ for the $m = 1$ case with two-way coupling and neglecting the effects of collisions, with $St = 70$.*

In the higher mass loading cases of $m = 1$ we see slight changes but on the whole the patterns are still the same. The reason is while a mass loading of one makes it seem as though the two phases may be in some sort of competition, this is only true in a limited sense. Since the particle density is $8800kg/m^3$ and the mass loading is 1 we know that the volume fraction of the particles is $1/8800$. This makes it clear that even with some moderate level of clustering the control volumes are still predominantly filled by gas which is being forced. The indication here is that while particle motions and two-way coupling effects can affect the flow, it is

nothing more than an augmentation of the current flow structure, as opposed to the formation of an entirely new structure. The apparently random particle structure shown in figure 6.49 is due to a few factors. The first is the fact that only a handful of particles are really present near the wall, making structure identification fairly difficult. The next reason is the relatively large Stokes numbers ($St = 70$) of the particles make them only weakly dependent on the generally weaker near wall structures. Thus the lack of a strong connection between the particle locations and motion and the near wall structures is fairly sensible.

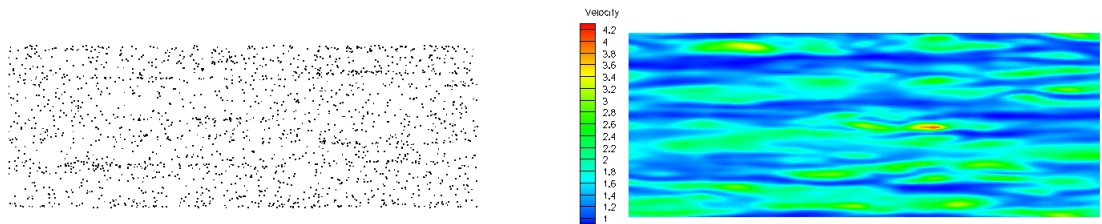


Figure 6.51: *Instantaneous particle structures in the near wall region ($0 < y^+ < 4$) for the $m = 1$ case using volumetric coupling and neglecting the effects of collisions, with $St = 70$.*

Figure 6.52: *Instantaneous gas velocity profile at a near wall plane corresponding to $y^+ = 4$ for the $m = 1$ case with volumetric coupling and neglecting the effects of collisions, with $St = 70$.*

Much as in the case with two-way coupling, the volumetric coupling shows very similar patterns but with slight changes. It seems possible that that the decreased fluid void fraction in the near wall regions, due to the presence of particles and the use of volumetric coupling, strengthens the near wall structures on the instantaneous gas phase contour plot 6.52. Thus large inertia particles are not surprisingly more dispersed, but have more effect when their finite size is included.

Note that in figure 6.51 it appears as if streamwise streaking motions are stronger. The mechanism for this is likely the volumetric coupling aspect which allows for a type of modified approximation to the wake effect, where particles lower local densities, which in turn causes a decrease in resistance to motion in that direction, which gives a stronger preference to the particle motion. The possibility that this visual assessment is correct will be analyzed in section 6.8.

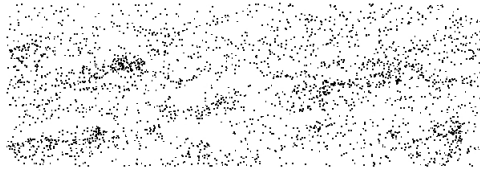


Figure 6.53: *Instantaneous particle structures in the near wall region ($0 < y^+ < 4$) for the $m = 0.01$ case using volumetric coupling and including the effects of collisions, with $St = 0.89$.*

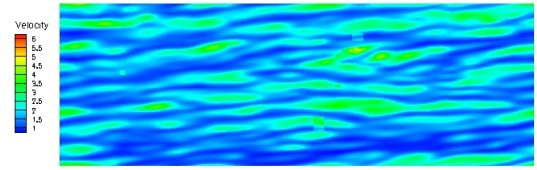


Figure 6.54: *Instantaneous gas velocity profile at a near wall plane corresponding to $y^+ = 4$ for the $m = 0.01$ case with volumetric coupling and including the effects of collisions, with $St = 0.89$.*

Figure 6.53 shows instantaneous view of the near wall particle profile for the low mass loading case. There is a decrease in uniformity of the streamwise streaking structures. No noticeable change is seen in figure 6.54 in comparison with the collision-free case.

Figures 6.55 and 6.57 show snapshots of the instantaneous near wall particle profiles using volumetric and two-way coupling respectively when the effect of collisions are included. There is no noticeable variation between the two suggesting that the coupling method has little to no effect on the formation of near wall structures. The collision model clearly prevents some of the streaking structures

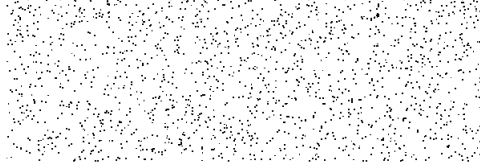


Figure 6.55: *Instantaneous particle structures in the near wall region ($0 < y^+ < 4$) for the $m = 1$ case using volumetric coupling and including the effects of collisions, with $St = 70$.*

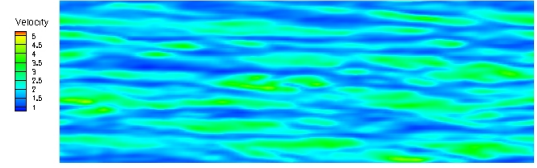


Figure 6.56: *Instantaneous gas velocity profile at a near wall plane corresponding to $y^+ = 4$ for the $m = 1$ case with volumetric coupling and including the effects of collisions, with $St = 70$.*

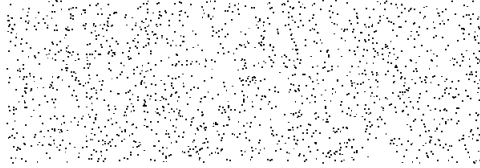


Figure 6.57: *Instantaneous particle structures in the near wall region ($0 < y^+ < 4$) for the $m = 1$ case using two-way coupling and including the effects of collisions, with $St = 70$.*

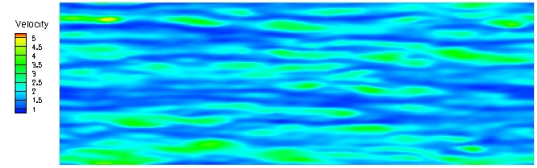


Figure 6.58: *Instantaneous gas velocity profile at a near wall plane corresponding to $y^+ = 4$ for the $m = 1$ case with two-way coupling and including the effects of collisions, with $St = 70$.*

by forcing particles to distance themselves from each other. The gas phase profiles for these two cases are shown in figures 6.56 and 6.58. Again no noticeable change occurs between the two methods.

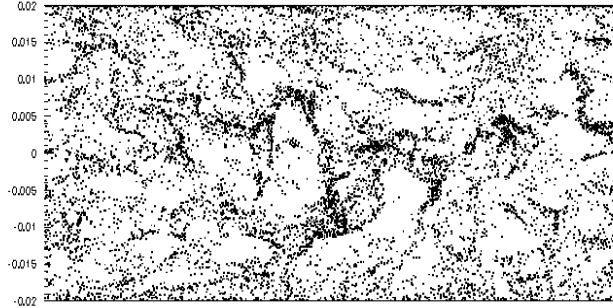


Figure 6.59: *Case 1: Wall Normal Streamwise Particle Structures $m = 0.01$, $d_p = 28\mu m$ - Volumetric Coupling*

6.7 Channel Centerline Particle Structures

Figure 6.59 shows an instantaneous view of a slice of the particle field. The slices shown in figures 6.59 to 6.63 show a slice along the centerline of the channel in the wall normal direction. The first figure has a really interesting profile, the streamwise spatial structures are quite strong. With their low stokes number these particles will be slowly ejected from traveling vortex cores, yielding these areas with higher particle volume fractions and areas with almost no particles.

Figures 6.60 and 6.61 share a common mass loading but have varying degrees in strength of spatial structure. The case using $50\mu m$ diameter particles has roughly ten times the number of particles as the case with $70\mu m$ diameter particles due to the differences in particle size and density. The spatial structures are once again clear in the first case but almost completely lacking in the latter. The reason for the lacking spatial structure in the latter case is the same as before,

an insufficient number of particles in the region of interest to establish a pattern, as well as having only weak structural properties to begin with.

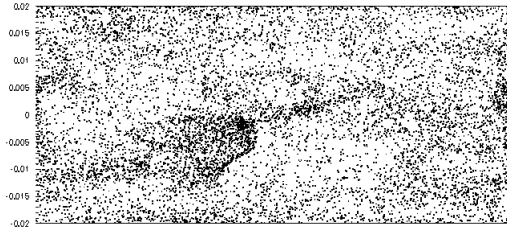


Figure 6.60: *Case 2: Wall Normal Streamwise Particle Structures*

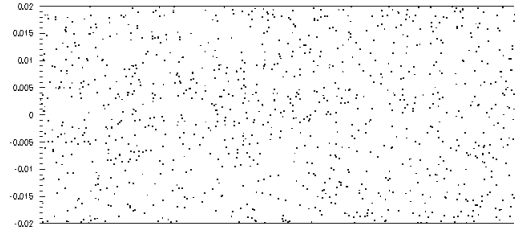


Figure 6.61: *Case 3: Wall Normal Streamwise Particle Structures*

Figures 6.62 and 6.63 show the difference that occurs when volumetric coupling is utilized in contrast to the point-particle approach. We see the same pattern occurring here as in the near wall figures. Volumetric coupling leads to stronger streamwise streak formation than two-way coupling as discussed previously.

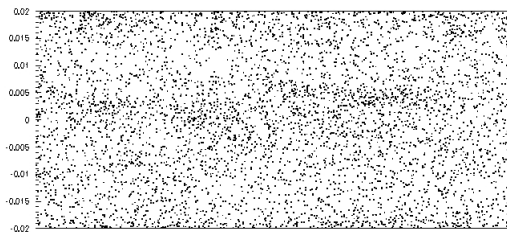


Figure 6.62: *Case 4: Wall Normal Streamwise Particle Structures - Two Way coupling*

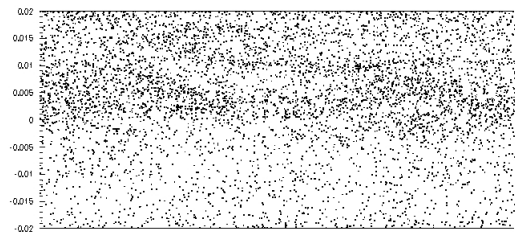


Figure 6.63: *Case 4: Wall Normal Streamwise Particle Structures - Volumetric coupling*

Note the contrast in the way the clustering behaves itself as a function of Stokes number. There is a clear progression of formation from figure 6.59 to 6.60 to 6.63.

The structures become more strongly aligned in the streamwise direction due to their increasing lack of response to the weaker lateral and wall normal forces of the fluid. We find that structure formation is a function of at least three things, the first is the coupling method, which has a large effect on streamwise structures. The second is the volume loading of the flow because significant interaction is required if the particles are not highly responsive to their local flow structures. Lastly, the particle Stokes number, which determines if the flow can reasonably institute particle structures in short periods of time, can occur regardless of mass loading at low Stokes numbers.

Essentially what we have found for large-density-ratio particle-laden flows is that even at a mass loading of one, volumetric coupling gives only slight differences compared to two-way coupling. The gas phase statistics show little response to volumetric coupling, the same is true for the particle phase statistics. The place where the effect of volumetric coupling becomes apparent is in particle clustering. It does not have any mean effect in wall-normal particle volume fraction, but it does increase the presence of flow structures. So the net effect is some streaking and structuring, but little effect on common statistical properties.

Table 6.2: Clustering Measurements ($m = 0.01$, $St = 0.89$)

Case	\hat{D}_g	\hat{D}_{wn}	\hat{D}_{zp}	d_g	d_{wn}	d_{zp}
Two-Way w/o Collisions	0.049	0.0437	0.0449	0.626	0.548	0.580
Two-Way w/ Collisions	0.058	0.0501	0.0471	0.702	0.601	0.664
Volumetric w/o Collisions	0.051	0.0444	0.0458	0.632	0.573	0.591
Volumetric w/ Collisions	0.057	0.0596	0.0468	0.705	0.645	0.662

6.8 Particle Clustering

This section discusses how using an inter-particle collision model and the choice of a coupling method effects particle clustering. Results for mass loadings of 0.01, 1 and 5 will be presented here.

One method of classifying particle clustering is known as the PDF method, or probability density function method. In this method the domain is split into small bins of equal size, the number of particles in each bin are tallied and a probability density function is built for the number of particles per bin. In general this function is most appropriately compared to the Poisson distribution, which represents the PDF that would result from applying this same technique to a purely random group of particles. Particle distributions closer to the Poisson distribution indicate a random distribution of particles in the domain. There are a few variations of this theme used here to analyze particle clustering in these flows. The global distribution refers to the entire domain as the subject of a single PDF, as such as regions within the flow are meshed together, it is not clear that this is an entirely accurate view of particle clustering since two different types of clustering can in

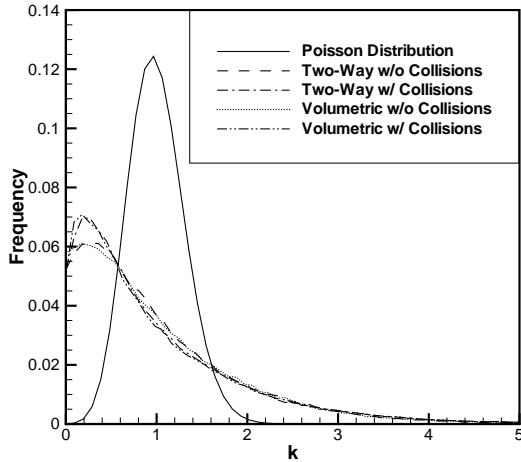


Figure 6.64: *PDF of particle distribution over the entire domain for the case with $m = 0.01$ and $St = 0.89$. The coupling method and inclusion of collisions are indicated in the legend.*

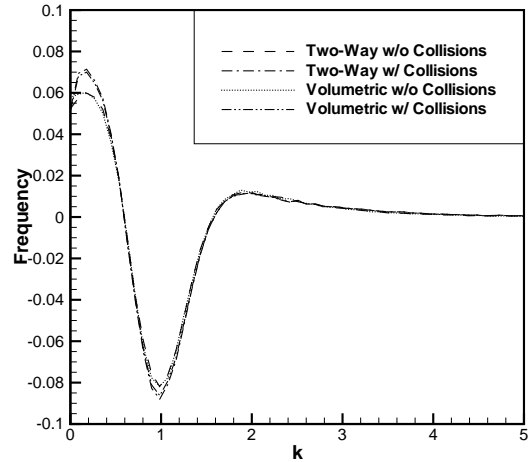


Figure 6.65: *The difference of the actual distribution and the Poisson distribution over the entire domain for the case with $m = 0.01$ and $St = 0.89$. The coupling method and inclusion of collisions are indicated in the legend.*

effect cancel each other. The deviation from the Poisson distribution gives a degree of variation from random.

$$\hat{D}_g = \sum_{n=1}^{\infty} [f_B(n) - f_P]^2 \quad (6.4)$$

In order to obtain more information about spatially non-uniform clustering features the domain is split, in two separate calculations, into slices in the wall normal and lateral direction. The hope is that by slicing the domain in the wall normal direction, any clustering features that are unique to the near wall area will be identified, as well as features unique to the channel centerline. Both of these

sets of results are discussed for the cases with a mass loading of 0.01 and 1.

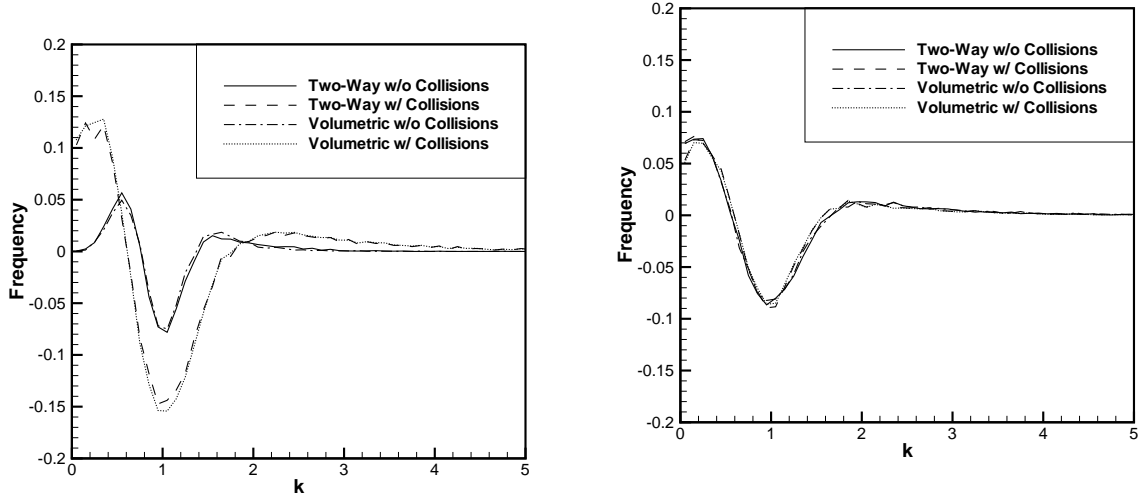


Figure 6.66: *The difference of the actual distribution and the Poisson distribution in a slice 1/20th the thickness of the domain next to the wall for the case with $m = 0.01$ and $St = 0.89$. The coupling method and inclusion of collisions are indicated in the legend.*

Figure 6.67: *The difference of the actual distribution and the Poisson distribution in a slice 1/20th the thickness of the domain taken halfway between the wall and the channel centerline for the case with $m = 0.01$ and $St = 0.89$. The coupling method and inclusion of collisions are indicated in the legend.*

The Poisson distribution is calculated using equation 6.5, where λ is the average number of particles per cell and n is the number of particles that the given probability is being calculated for. A measure of clustering that can be calculated for this type of particle-laden flow is the deviation of the number density from that of a random distribution, \hat{D}_g , which is the deviation over the entire domain [68]. Calculated for each individual slice, \hat{D}_{wn} is the deviation over each wall normal slice averaged and \hat{D}_{zp} is averaged over each lateral slice. A second measure of the

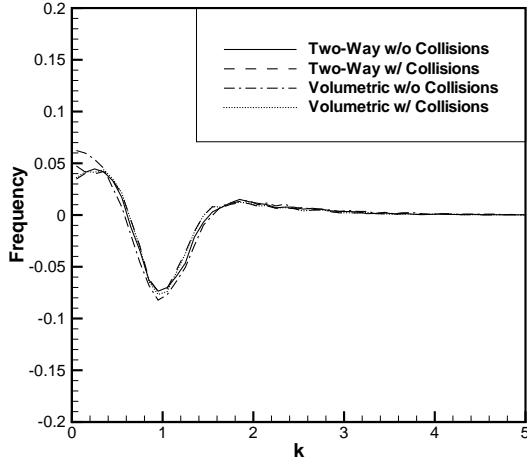


Figure 6.68: *The difference of the actual distribution and the Poisson distribution in a slice 1/20th the thickness of the domain in the channel centerline for the case with $m = 0.01$ and $St = 0.89$. The coupling method and inclusion of collisions are indicated in the legend.*

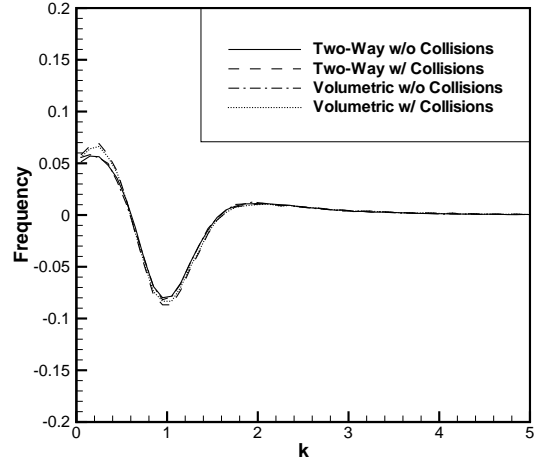


Figure 6.69: *The average difference of the actual distribution and the Poisson distribution in each of the 20 slices of the domain for the case with $m = 0.01$ and $St = 0.89$. The coupling method and inclusion of collisions are indicated in the legend.*

deviation is calculated by dividing the difference between the standard deviation of the actual distribution and the standard deviation of the Poisson distribution by the average number of particles per bin and is denoted by d_g [64]. The same averaging techniques are applied to find d_{wn} and d_{zp} .

$$f_P(n) = \frac{e^{-\lambda} \lambda^n}{n!} \quad (6.5)$$

Figure 6.64 shows the global probability density function for the case of $m = 0.01$ using two-way and volumetric coupling as well as with and without collisions. The variations between two-way and volumetric coupling are extremely

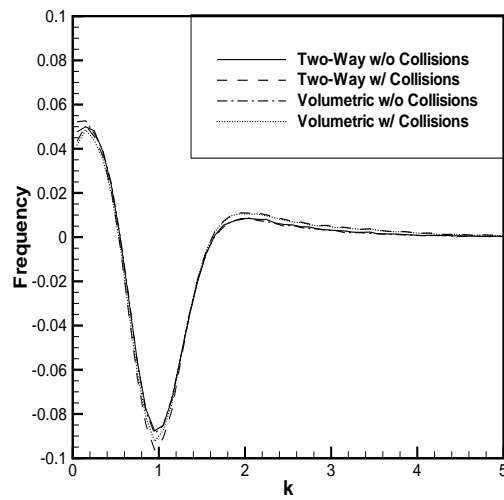


Figure 6.70: The average difference of the actual distribution and the Poisson distribution averaged over 16 slices in the lateral direction for the case with $m = 0.01$ and $St = 0.89$. The coupling method and inclusion of collisions are indicated in the legend.

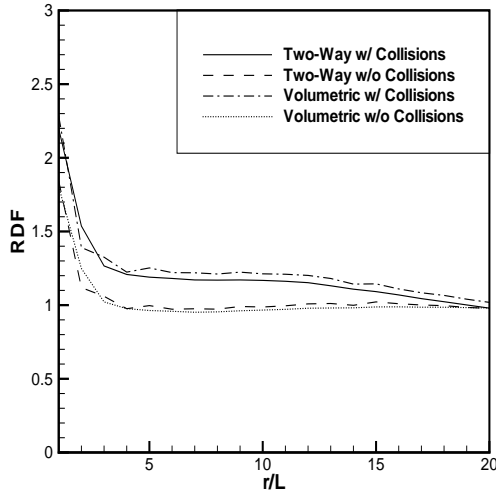


Figure 6.71: Particle radial distribution functions for the indicated coupling method and collision effect for the case where $m = 0.01$ and $St = 0.89$.

small, however a difference can be noticed when the interparticle repulsion force collisions model is employed. Figure 6.65 shows the deviation from the Poisson distribution for the entire domain. This gives a more clear image as to just how closely two-way and volumetric coupling predict particle clustering.

In order to check for differences in the near wall and channel centerline structures the domain was split as previously described. In figure 6.66 a slice with a thickness of one twentieth of the wall normal domain distance is taken next to the wall. This figure shows very little difference between two-way and volumetric coupling approximations. Figure 6.67 is a slice half way between the wall and the centerline of the channel, the properties of this slice are much the same. Little difference is noticed based on coupling method, but there is a significant difference

Table 6.3: Clustering Measurements ($m = 1.0$, $St = 70$)

Case	\hat{D}_g	\hat{D}_{wn}	\hat{D}_{zp}	d_g	d_{wn}	d_{zp}
Two-Way w/o Collisions	0.024	0.0074	0.0422	0.4854	0.1220	0.4333
Two-Way w/ Collisions	0.0095	0.0078	0.0307	0.2072	0.1283	0.1583
Volumetric w/o Collisions	0.0238	0.0118	0.0427	0.4287	0.1529	0.3778
Volumetric w/ Collisions	0.0088	0.0128	0.0302	0.2015	0.1625	0.1520

when the collision model is employed.

Figure 6.68 gives the variation from random of a channel centerline slice. Figure 6.69 shows the average deviation from random for all wall normal slices. Each wall normal slice has it's own Poisson distribution based on its own average number of particles. The average of the slices is a fairly accurate representation of any individual slice.

The same patterns are seen on the average over all lateral slices of the domain. Figure 6.70 shows little variation when varying the coupling method, however significant variation occurs from utilizing the collision model.

Another way to classify clustering is the use of a particle radial distribution function. When doing this the RDF, or radial distribution function, is calculated by finding the distance between each pair of particles in the domain and placing them into bins of distances from the original particle. The number obtained from doing this is divided by the number of particles that would be expected in each bin if the particles were to be distributed either uniformly or randomly throughout the domain, in this case a uniform distribution was used. This tool is generally used in isotropic turbulence because the lack of a preferential direction yields more

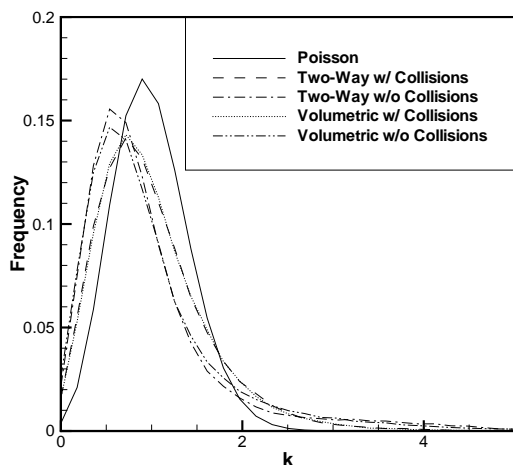


Figure 6.72: *PDF of particle number density over the entire domain plotted against the Poisson distribution for the case when $m = 1$ and $St = 70$. The inclusion of collisions and the coupling method are indicated in the legend.*

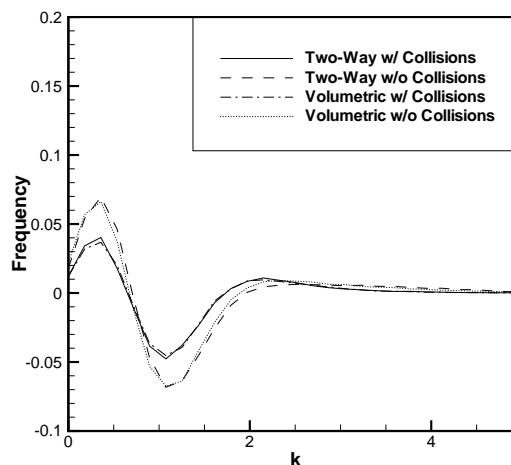


Figure 6.73: *Difference between Poisson distribution and actual distribution of particle number density over the entire domain for the case when $m = 1$ and $St = 70$. The inclusion of collisions and the coupling method are indicated in the legend.*

interesting results. Figure 6.8 shows the RDF for the case when $m = 0.01$ and $St = 0.89$. There is no real difference between the coupling methods but the collisions model clearly affects the preferential accumulation at small distances.

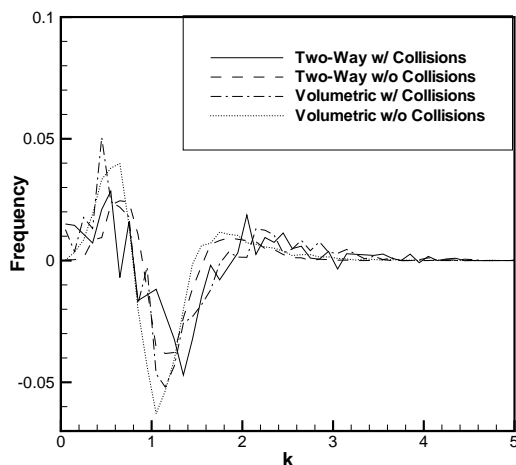


Figure 6.74: Average difference between Poisson distribution and actual distribution of particle number density in a near wall slice with a thickness of one twentieth of the channel width for the case when $m = 1$ and $St = 70$. The inclusion of collisions and the coupling method are indicated in the legend.

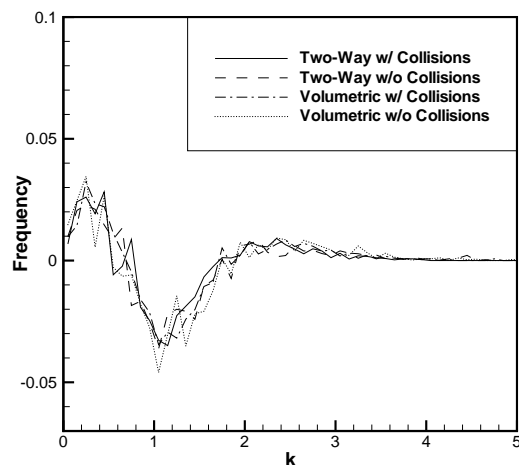


Figure 6.75: Average difference between Poisson distribution and actual distribution of particle number density in a slice taken halfway between the wall and the channel centerplane for the case when $m = 1$ and $St = 70$. The inclusion of collisions and the coupling method are indicated in the legend.

Table 6.2 shows several measures of the deviation for the case where $m = 0.01$. The calculated values show little to no deviation between two-way and volumetric coupling. The differences seen in the applicable figures are well represented here as seen by the differences between the cases ran with and without coupling.

The same results are presented for the case with a mass loading of 1. The global PDF is plotted with the Poisson distribution in figure 6.72 and the difference from the Poisson distribution in 6.73. This case has a mass loading a full $100\times$ higher than the previous, however, globally the same trend exists. The coupling method has an insignificant effect on the particle structure but the collision model

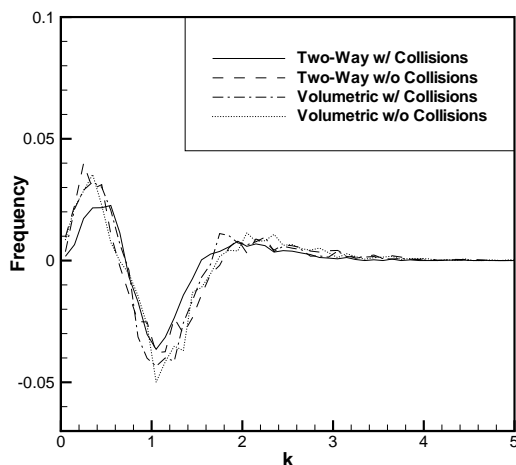


Figure 6.76: Average difference between Poisson distribution and actual distribution of particle number density in a slice at the centerline of the channel for the case when $m = 1$ and $St = 70$. The inclusion of collisions and the coupling method are indicated in the legend.

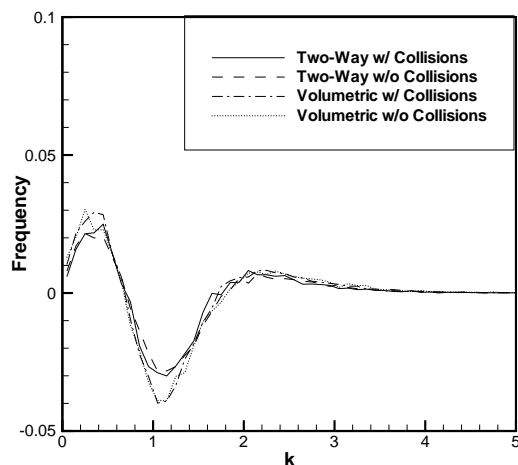


Figure 6.77: Average difference between Poisson distribution and actual distribution of particle number density averaged over ten wall normal slices for the case when $m = 1$ and $St = 70$. The inclusion of collisions and the coupling method are indicated in the legend.

drastically changes the distribution profile.

Even though the global pdf distribution appears to show no sizable difference it is important to see if there are any differences locally. It is possible that volumetric effects alter the clustering in the near wall region compared to near the channel center. Figure 6.74 shows the near wall region pdf for the case with a mass loading of one. The coupling method again shows no difference at a mass loading of one in the near wall region. The quarter-width pdf is shown in figure 6.75 with the same result.

Figures 6.76 and 6.77 show the channel centerline pdf and the average pdf over

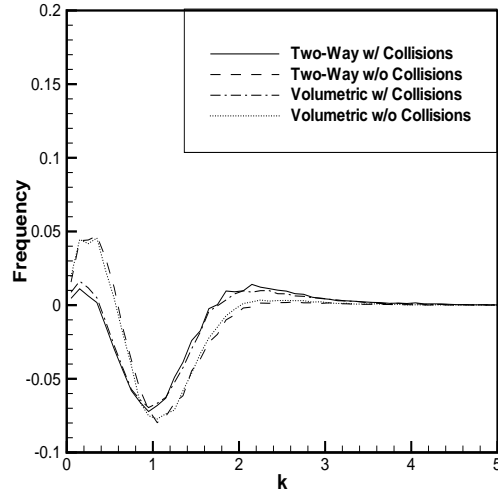


Figure 6.78: Average difference between Poisson distribution and actual distribution of particle number density averaged over 16 lateral slices for the case when $m = 1$ and $St = 70$. The inclusion of collisions and the coupling method are indicated in the legend.

all wall normal slices respectively. There is no noticeable variation in the channel centerline structure, just like the previous cases. The wall normal slice averaged profile shows exactly what is expected, that there is no significant difference.

The lateral slices are averaged since there is no flow feature that varies between the slices, figure 6.78 shows this. No sizable difference is found, the collision model does make a difference once again, as is expected. The data in table 6.3 details the analysis of the case when $m = 1$. The same overall patterns is seen from the lower mass loading case. The results validate the assessment given for figures 6.72 to 6.78.

The features shown in figure 6.8 are not particularly interesting for two reasons.

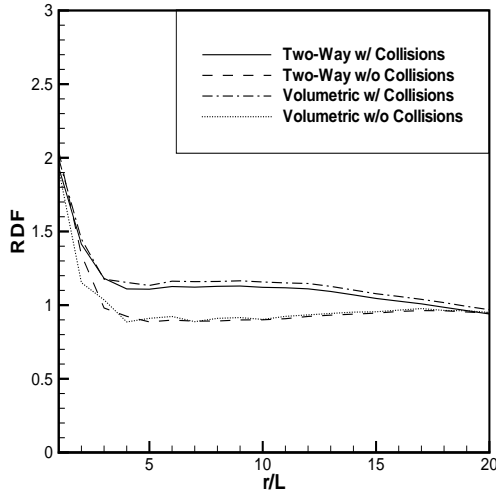


Figure 6.79: Particle radial distribution functions for the indicated coupling method and collision effect for the case where $m = 1$ and $St = 70$.

One is that the scope of the distance is limited by the wall-normal directional limitations. The second reason is that once again little to no difference is found between the coupling methods, however a moderate difference is found when the collision model is employed.

Figures 6.80 and 6.81 show the global particle pdfs for the case where $m =$

Table 6.4: Clustering Measurements ($m = 5.0$, $St = 70$)

Case	\hat{D}_g	\hat{D}_{wn}	\hat{D}_{zp}	d_g	d_{wn}	d_{zp}
Two-Way w/o Collisions	0.0649	0.129	0.197	1.331	0.335	1.27
Two-Way w/ Collisions	0.0116	0.0054	0.0054	0.215	0.147	0.136
Volumetric w/ Collisions	0.0164	0.0061	0.0061	0.248	0.155	0.174

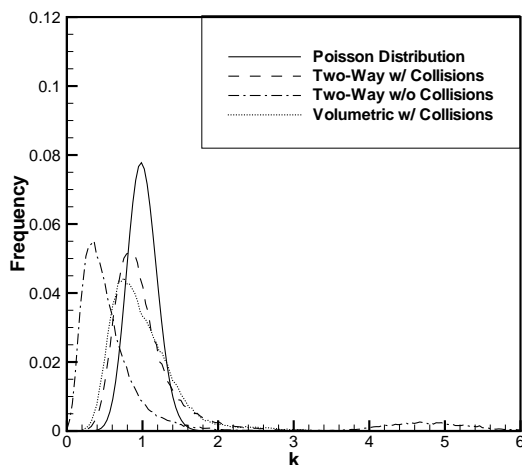


Figure 6.80: Average difference between Poisson distribution and actual distribution of particle number density over the entire domain for the case when $m = 5$ and $St = 70$. The inclusion of collisions and the coupling method are indicated in the legend.

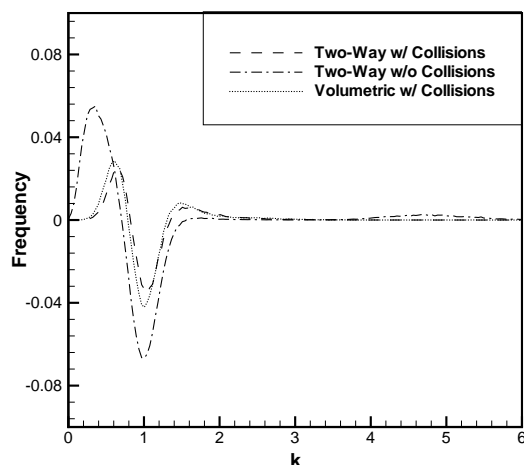


Figure 6.81: Average difference between Poisson distribution and actual distribution of particle number density averaged over 16 wall normal slices for the case when $m = 5$ and $St = 70$. The inclusion of collisions and the coupling method are indicated in the legend.

5. As in the previous cases, the collision model drastically alters the particle distribution, but the choice of coupling method has very little effect. Table 6.4 verifies these observations. Only slight differences are seen when the coupling method is varied, large differences are seen when the collision model is employed.

6.9 Analysis of Coupling Sources

The previous section provided an analysis of particle clustering for the particle-laden channel flow case. Little to no difference was found for the given measures of clustering. It was also shown that there is little variation in gas and particle phase flow statistics for the mass loadings studied. This raises the question of how to quantify the effect of utilizing volumetric coupling. It was hypothesized that the volumetric coupling approximation could become important in the near wall cells because the flux of mass into the cell due to particle motion could be a significant portion of the total cell mass. Since the near wall flow features are in many ways the dominant mechanism for determining the characteristics of a channel flow these effects could be significant. This section seeks to understand why only small changes are seen between coupling methods.

$$\frac{\partial(\rho u_i)}{\partial t} + \frac{\partial}{\partial x_j}(\rho u_j u_i) = -\frac{\partial P}{\partial x_i} + \frac{\partial}{\partial x_j} \left(\mu_f \left(\frac{\partial}{\partial x_j}(u_{c_i}) + \frac{\partial}{\partial x_j}(u_{c_i}^T) \right) \right) + f_i \quad (6.6)$$

Equation 6.6 gives the Navier-Stokes equation with f_i being the two-way coupling source term.

$$\rho = \rho_f \Theta_f \quad (6.7)$$

In this equation ρ is not constant despite the the flow being incompressible, it is found from equation 6.7 to account for the changing volume fraction of the

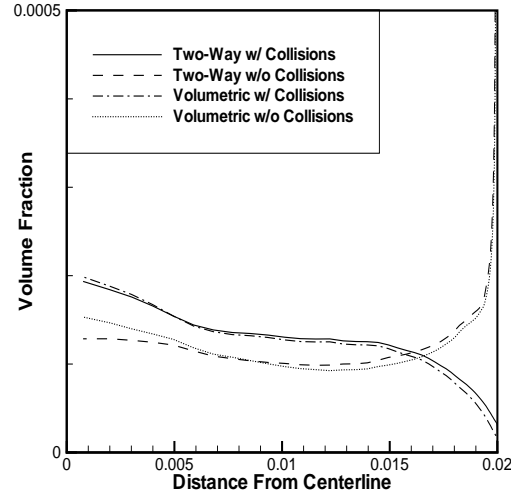


Figure 6.82: Wall-normal particle volume fraction for the case where $m = 1$ and $St = 70$.

particles. After some rearrangement the new form is as follows.

$$\underbrace{u_i \frac{\partial \rho}{\partial t}} + \rho \frac{\partial u_i}{\partial t} + \rho u_j \frac{\partial u_i}{\partial x_j} + \underbrace{u_i \frac{\partial(\rho u_j)}{\partial x_j}} = -\frac{\partial P}{\partial x_i} + \frac{\partial}{\partial x_j} \left(\mu_f \left(\frac{\partial}{\partial x_j} (u_{c_i}) + \frac{\partial}{\partial x_j} (u_{c_i}^T) \right) \right) + f_i \quad (6.8)$$

Utilizing conservation of mass we get:

$$\frac{\partial u_i}{\partial t} + u_j \frac{\partial u_i}{\partial x_j} = -\frac{1}{\rho} \frac{\partial P}{\partial x_i} + \frac{1}{\rho} \frac{\partial}{\partial x_j} \left(\mu_f \left(\frac{\partial}{\partial x_j} (u_{c_i}) + \frac{\partial}{\partial x_j} (u_{c_i}^T) \right) \right) + \frac{1}{\rho} f_i \quad (6.9)$$

The product rule applied to the convective term gives equation 6.10.

$$u_j \frac{\partial u_i}{\partial x_j} = \frac{\partial}{\partial x_j} (u_j u_i) - u_i \frac{\partial u_j}{\partial x_j} \quad (6.10)$$

The final form is found below. The Navier-Stokes equations with the volumetric coupling approximation have been rearranged to make evaluation of the relative source magnitudes possible.

$$\frac{\partial u_i}{\partial t} + \frac{\partial}{\partial x_j} (u_j u_i) = -\frac{1}{\rho} \frac{\partial P}{\partial x_i} + \frac{1}{\rho} \frac{\partial}{\partial x_j} \left(\mu_f \left(\frac{\partial}{\partial x_j} (u_{c_i}) + \frac{\partial}{\partial x_j} (u_{c_i}^T) \right) \right) + \underbrace{\frac{1}{\rho} f_i}_{(1)} + \underbrace{u_i \frac{\partial u_j}{\partial x_j}}_{(2)} \quad (6.11)$$

$$(1) = \text{Source Due to Two-Way Coupling} \quad (6.12)$$

$$(2) = \text{Source Due to Volumetric Coupling} \quad (6.13)$$

Note that when the two-way coupling approximation is used, source term (2) is zero by conservation of mass, i.e. divergence free flow. Comparison of terms (1) and (2) should provide a measure of the relative influence of two-way and volumetric coupling on the gas phase flow.

As was hypothesized before, it seems likely that volumetric coupling effects will be strongest in the near wall region due to the relatively small cell volume and higher particle residence times (loading). The wall-normal volume fractions for the four cases with a mass loading of one are shown in figure 6.82. From this

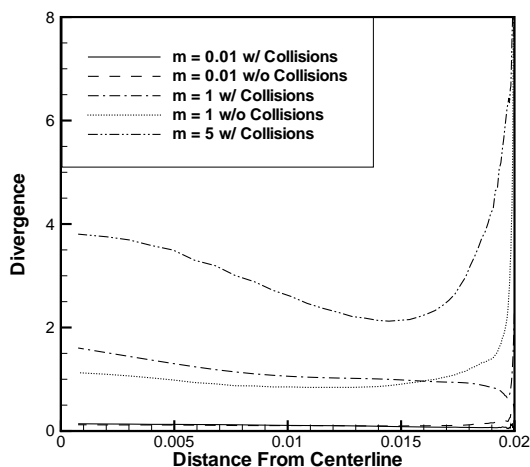


Figure 6.83: Wall-normal average profile of fluid divergence. The wall is at $0.02m$ and the channel centerline is at $0.0m$.

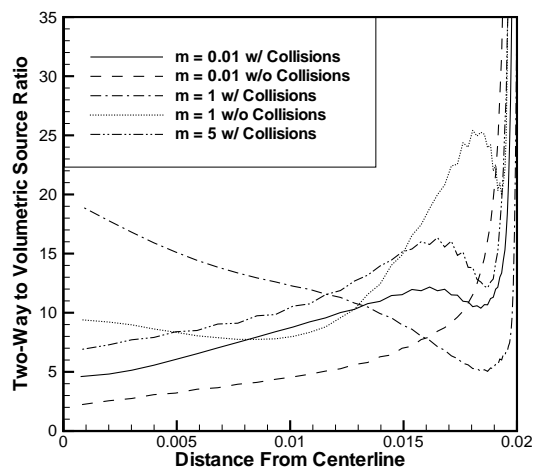


Figure 6.84: Wall-normal average profile of the ratio of two-way coupling forces to volumetric coupling forces. The wall is at $0.02m$ and the channel centerline is at $0.0m$.

figure and the previous assertions it seems likely that the effect would be largest when the effect of collisions is not included since the near wall volume fraction is much higher.

Figure 6.83 shows the wall normal gas phase divergence profile for several cases. As expected the divergence is highly related to the volume fraction. The divergence is caused not just by the presence of particle, but by the motion of particles. The vast majority of this motion is in the streamwise direction. The near-wall streamwise particle velocity is lower than at the channel centerline, but this is balanced by the small grid cell sizes.

Figure 6.84 shows the ratio of the two-way coupling forces to the volumetric coupling forces as a function of wall normal distance for several cases. This shows

Table 6.5: Two-Way to Volumetric Coupling Force Ratios

Case	Global Coupling Ratio
$m = 0.01$ w/o Collisions	9.21
$m = 0.01$ w/ Collisions	9.76
$m = 1$ w/o Collisions	15.02
$m = 1$ w/ Collisions	14.43
$m = 5$ w/ Collisions	13.96

that even in the near wall region, two-way coupling forces still dominate even for a mass loading of 5. Drag and lift forces, which are largest near the wall, are still applied to the same smaller control volumes where the flow divergence effects are large. So while the divergence is larger for the collision free cases, so are the two-way coupling forces. It may seem counter intuitive that the ratio for the case when $m = 0.01$ is on the same order of magnitude to the ratio for the case when $m = 5$. The volumetric coupling effect is indeed small for the low mass loading case due to the small particle sizes, however this yields small two way coupling forces as well. So the ratio here is a ratio of very small numbers, unlike the case when $m = 5$.

The domain-averaged values for the ratio of the two-way coupling to volumetric coupling forces are given in table 6.5. It is just clear that two-way coupling forces are dominant for this type of simulation. This shows that, for the large density ratio particles considered in this work, the volumetric effects are typically small compared to the inter-phase momentum transfer terms. Locally, large divergences are obtained in regions where particle loading and two-way coupling effects are

also large. For lower density ratios (sand in water or bubbles in a fluid), these volumetric effects can be significant, even for dilute loadings, as suggested by previous work [40] [71] [72] [75].

6.10 Summary of Channel Flow Cases

The lowest levels of mass loading showed little to no turbulent attenuation in the gas phase. When the effect of collisions was ignored the wall-normal fluctuations were the only mechanism for particle dispersion, yielding a profile in which the majority of the particles were in the near wall region. These wall-normal fluctuations were also much lower without collisions, as the colliding particles themselves are a source of wall-normal energy transfer. This was also true in the lateral direction, but to a far lesser degree as the wall itself is the largest damper of motion. Without collisions, less energy is taken from the streamwise motion of particles to be transferred to the lateral and wall-normal directions. Significant turbulent attenuation occurs at a mass loading of 1, collisions are a major source of channel centerline turbulent intensity at this mass loading since the volume fraction is much higher than when collisions are ignored. This yields higher rms velocities when collisions are considered which counteracts some of the damping caused by the mass loading. It was suggested in Yamamoto et al. [2] that including the effect of particle presence in an SGS model (see equation 3.7) may help reproduce experimental results, but little effect was found in comparing the turbulent statistics between two-way and volumetric coupling.

The formation of particle structures varied greatly when collisions were considered. Near wall structures show a great deal of streaking without collisions, the streaks seem to correlate well with low velocity regions as was found in previous studies [27] [28] [2]. The streamwise streaking is relatively weak when collisions

are considered, the same result is found at the channel centerline. Visually there is little difference in the structures predicted by two-way and volumetric coupling. Section 6.8 detailed a statistical analysis of these features. An analysis for the lack of change was given in section 6.9, where it was determined that even in the near wall region, two-way coupling forces are roughly one order of magnitude larger than those due to the inclusion of finite-volume effects.

Chapter 7 – Conclusions and Outlook

Large-eddy simulation of particle-laden flows shows promise in its ability to handle higher mass loading flows. In these studies it was shown that a particle-laden slot nozzle jet injected into an ambient fluid was well handled by the LES methodology. These models were able to reproduce the overall jet structure as well as provide excellent gas phase statistics. The results for both phases were adequate to provide the user confidence is that the fundamental physics is being well handled. The turbulent particle-laden channel flow showed excellent agreement with published results using both constant pressure gradient and constant mass flow rate forcing techniques. Higher mass loading cases were studied and the turbulent intensities and velocity spectra were found to have significant turbulent attenuation due to the dampening affect of the heavier particles. It should be concluded that the techniques utilized here would seem to have a high degree of potential for handling more difficult problem in complex geometries with the accuracy needed to maintain predictive capability for either building higher order models or directly simulating the physical situation of interest.

An in depth analysis of how the two-way and volumetric coupling approximations predict the features of a turbulent channel flow was performed. This work was motivated through basic intuition and a series of studies showing how profound an effect the inclusion of a volume displacement model can have in many systems. The systems that show significant differences are not limited to bubbly flows but also include flows with Stokes numbers much larger than one and/or particle to fluid density ratios greater than one. For large density ratios, the coupling method showed no deviation in prediction of the traditional statistical

measures of turbulent flows; i.e. mean velocity, gas and particle rms velocities and volume fraction. Near wall and channel centerline images of instantaneous profiles of gas phase structures and particle profiles also showed little to no variation when the coupling method was changed. A statistical analysis was performed using the probability density function method and the radial distribution function methods to see if particle clustering was affected throughout the domain. These methods showed no discernable difference when the coupling method was changed, only including interparticle collisions using an inter-particle repulsion force model drastically affected the statistical measures of particle clustering, which is to be expected.

While the methods performed well there are a large number of ways in which the results can be improved. As discussed earlier, near wall particle size is very large compared to the wall-normal grid resolution. This motivated the use of volumetric coupling for this work. Alternatively, adjusting the way the particle forces are distributed in the near wall cells may yield significant changes in flow properties when the particles themselves are larger in length than the wall normal grid cells. This should be investigated. It has been suggested in the literature and was shown here that the Saffman lift force can sometimes overpredict the forces of lift on particle greatly and lead to suspicious behavior of the particle phase, they suggest an augmentation that should be implemented to see what adjustments are made [39]. Research of this type has an almost inexhaustible supply of possibilities for improvement, the ones listed here are those that should currently be the highest priority to further the research presented.

APPENDICES

Appendix A – Numerical Formulation

A procedure for the solution of the equations from the previous section will now be outlined. The methodology outlined in this section has developed from the original fractional step method of Kim and Moin (1985) [54], to an updated form in Choi and Moin (1995) [55], to a very similar method detailed by Kim and Choi (2000) [56] and then into the present form.

To begin with an explicit Euler advancement, as shown in equations (A.1) and (A.2), is used to project intermediate values of particle and fluid velocities.

$$u_p^{n+1/2} = u_p^{n+3/2} \quad (\text{A.1})$$

$$u_f^n = u_f^{n+1} \quad (\text{A.2})$$

The particle phase locations are taken and velocities are interpolated from the local control volumes to provide a velocity at the point at which the particle exists. The forces acting on the particle are calculated based on the last time steps fluid flow field. Thus the particle motion is determined explicitly. Once each particle is assigned a velocity, the particle equations of motion (3.10) are solved using third order Runge-Kutta with inter-particle collisions being checked for at each iteration. If a collision takes place it is handled and the forces on the particle are augmented

to reflect this. Once this has occurred the particle motion solution continues. The particle motion is determined from the forces by equation A.3.

$$\mathbf{a}_p = \sum F_p/m_p \quad (\text{A.3})$$

The particle acceleration is the utilized to determine the particle velocity and then position using equations A.4 and A.5.

$$\mathbf{u}_p^{new} = \mathbf{u}_p + \mathbf{a}_p \Delta t_p \quad (\text{A.4})$$

$$\mathbf{x}_p^{new} = \mathbf{x}_p + \mathbf{u}_p \Delta t_p \quad (\text{A.5})$$

Once the particles have been advanced to the next time step, $(n + 1)$, they are once again located using the interpolation function (A.6), their mass is associated with the surrounded control volumes using a Gaussian interpolation kernel (A.7)

$$\Theta_p(\mathbf{x}_{cv}) = \sum_{p=1}^{N_p} \forall_p \mathbf{G}_\sigma(\mathbf{x}_{cv}, \mathbf{x}_p) \quad (\text{A.6})$$

$$G_\sigma(\mathbf{x}_{cv}, \mathbf{x}_p) = \frac{1}{(\sigma\sqrt{2\pi})^3} \exp\left(-\frac{\sum_{k=1}^3 (x_k - x_{p,k})^2}{2\sigma^2}\right) \quad (\text{A.7})$$

In volumetric coupling the particle phase has a finite size, this size displaces a certain amount of fluid in each control volume. The volume that has been interpolated to each control volume is summed to find a particle volume fraction within each control volume. The particle volume fraction is then subtracted from

one to determine the local fluid volume fraction ($\Theta_f = 1 - \Theta_p$). The fluid volume fraction multiplied by the density ρ_f is then set to be the new local operational density of the fluid.

$$\rho^{n+1} = \rho_f \Theta_f \quad (\text{A.8})$$

This augmented density is used in the momentum equation solver, this is where the code has utilized volumetric coupling. Once this is done and the predictors (u_f^n) have been utilized, the equations of motion have been linearized. Gauss-Seidel is then applied using successive over relaxation to iteratively solve the momentum equations (A.9), to find a predicted velocity for the value at time step $n + 1$, this predicted velocity is generally denoted by \hat{u} .

$$\begin{aligned} \frac{\rho^{n+1} \hat{u}_i - \rho^n u_i^n}{\delta t} + \frac{1}{2\mathcal{V}_{cv}} \sum_{\text{faces of } cv} [u_{i,f}^n + \hat{u}_{i,f}] g_N^{n+1/2} A_f = \\ \frac{1}{2\mathcal{V}_{cv}} \sum_{\text{faces of } cv} \mu_f \left(\frac{\partial \hat{u}_{i,f}}{\partial x_j} + \frac{\partial u_{i,f}^n}{\partial x_j} \right) A_f + F_i^n \end{aligned} \quad (\text{A.9})$$

This is why the fractional step method is called semi-implicit, the velocity field is not strictly predicted implicitly, but partially implicitly and partially based on projected values from explicit time steps. In equation (A.9), g_N is the normal momentum flux through a control volume face, so $g_N = \rho u_{f,N}$. In equation (A.9) F_i^n is the interphase momentum transport. At this point the old pressure gradient is removed from the velocity field in order to allow the freedom necessary to apply

a corrector step, the enforcement of continuity.

$$\frac{\rho^{n+1}u_i^{n+1} - \rho^{n+1}\hat{u}_i}{\Delta t} = -\frac{\delta p^n}{\delta x_i} \quad (\text{A.10})$$

$$\frac{\rho^{n+1}u_N^{n+1} - \rho^{n+1}\hat{u}_N}{\Delta t} = -\frac{\delta p^n}{\delta x_N} \quad (\text{A.11})$$

With the old pressure removed the new pressure is determined by applying the incompressibility condition, that of a divergence free velocity field, to find an equation for the new pressure which is required to augment the velocity field such that it satisfies continuity. Once the pressure Poisson equation (A.12) is solved, the corrected u^{n+1} velocity can be calculated directly.

$$\frac{1}{\nabla_{cv}} \sum_{\text{faces of } cv} \frac{\delta p}{\delta x_N} A_f \Delta t = \frac{1}{\nabla_{cv}} \sum_{\text{faces of } cv} \rho_f^{n+1} \hat{u}_{i,f} A_f + \frac{\delta \rho}{\delta t} \quad (\text{A.12})$$

Once u^{n+1} has been found any user specific computations are completed and the cycle begins again by computing particle trajectories based on the now explicit velocity information.

Appendix B – Taylor-Vortex Case

Three validation cases are presented to show that the mathematical models described above as well as the numerical implementation are working properly. The first case is a simple test problem with a known analytical solution, the Taylor vortex case. This case demonstrates the solvers second order spatial accuracy. The second is the turbulent channel flow case on Kim Moin and Moser (1987) [57] which will demonstrate the solvers ability to perform large-eddy simulation and accurately reproduce established turbulent channel flow results.

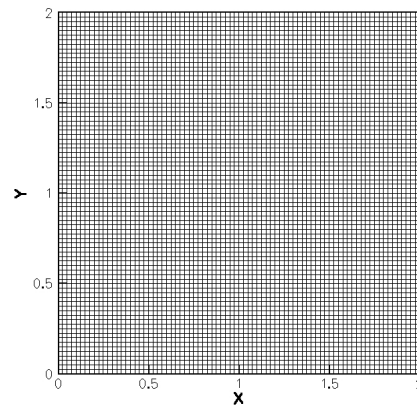
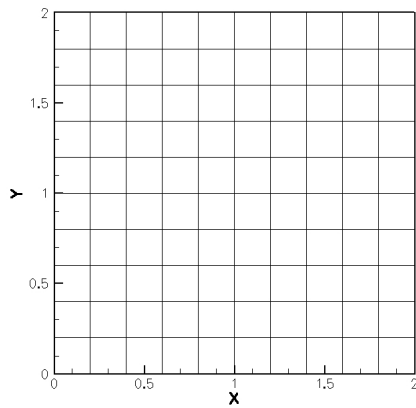


Figure B.1: *Mesh for the coarse grid Taylor-Vortex case.* Figure B.2: *Mesh for the resolved grid Taylor-Vortex case.*

$$u(x, y, t) = -\cos(\pi x)\sin(\pi y)e^{-2\pi^2\nu t} \quad (\text{B.1})$$

$$v(x, y, t) = \sin(\pi x)\cos(\pi y)e^{-2\pi^2\nu t} \quad (\text{B.2})$$

$$p(x, y, t) = -0.25(\cos(\pi x) + \cos(2\pi y))e^{-4\pi^2\nu t} \quad (\text{B.3})$$

The Taylor-Vortex case utilizes a known analytical solution to a simple physical situation for the Navier-Stokes equations. To measure the accuracy of the solver this case is set up and ran in order to measure the error between the computed temporal development of the flow (i.e. eddy decay) versus what is predicted by the analytical solution. The analytic solution is given here in equations (B.1), (B.2) and (B.3).

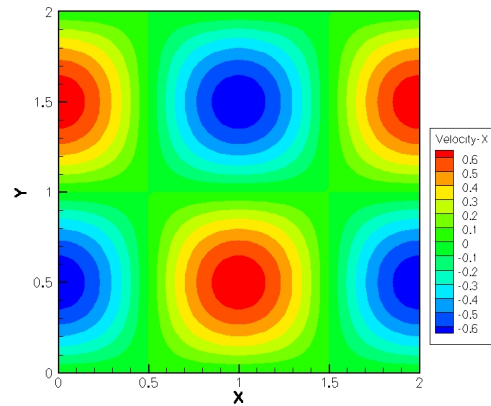
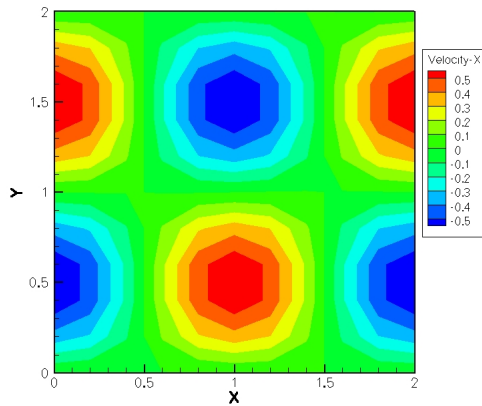


Figure B.3: *Coarse Grid - \hat{x} Velocity.*

Figure B.4: *Resolved Grid - \hat{x} Velocity.*

The exponential term provides an initial condition (at $t = 0s$) and a final solution, which in this case is at $t = 0.2s$. The simulation is ran with four different grid

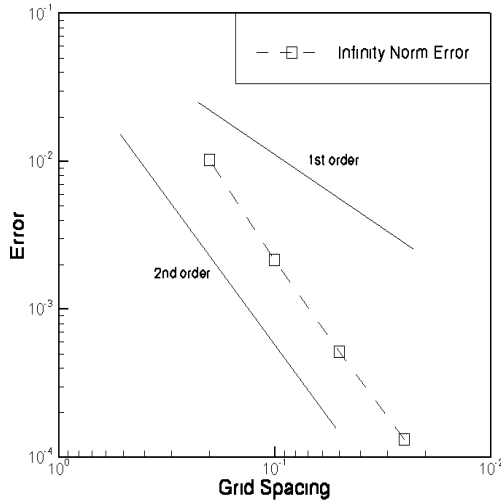


Figure B.5: L_∞ norm error. Lines indicate 1st and 2nd order error for reference.

spacings, each with an appropriate time step in order to keep the CFL (Courant–Friedrichs–Lewy) number constant. The four mesh spacings and time steps are $\Delta x = 0.2, 0.1, 0.05, 0.025$ and $\Delta t = 0.02, 0.01, 0.005, 0.0025$. The various relevant constants are set as follows; $\nu = 0.1$, $\rho = 1$ with a Reynolds number of 10.

The grids used for the least and most resolved cases are shown in figures B.1 and B.2. The refinement difference is clear, this should give the reader a fair idea of what to expect as far as accuracy.

Figures B.3 and B.4 are the \hat{u} velocity components for the least and most resolved cases respectively. The eddy structures are quite apparant in these images. The meat of what we care about though is the overall accuracy of the solver, and its order associated with grid resolution.

Reference lines for *1st* and *2nd* order accuracy are placed on figure B.5. This figure shows the four error values corresponding to the four varying grid resolution cases detailed above. The infinity norm error is used for this, which is the maximum error at any point in the domain over the course of the simulation. The conclusion is that the solver is approximately *2nd* order accurate spatially.

Appendix C – Turbulent Channel Flow

The Taylor-Vortex study showcased the codes ability to accurately solve fluid flow problems under simple circumstances. There is however, something more to be shown here. Somewhere buried within the convective terms of the Navier-Stokes Equations is the mainstay of turbulence, non-linear motion. These facets must interact harmoniously with the viscous terms to create a system where a delicate balance is created. The largest eddys must input energy and transfer them to smaller eddies and so on until ultimately viscous effects take over and win out. There are some numerical issues here that are less straight forward than some other cases, in particular the handling of these nonlinear terms. If there had been some small bungling of these terms it may not have shown up well in the Taylor-Vortex case, however a turbulent channel flow is a more difficult case study for a problem such as this to hide. We compare our results to that of the direct numerical simulation study of Kim, Moin and Moser (1987) [57].

Table C.1: Turbulent Channel Flow - Computational Parameters

Parameter	Value
Computational Domain	$4\pi \times 2 \times 2\pi$
Fluid Viscosity (μ)	0.0070303 kg/ms
Fluid Density (ρ)	1.0 kg/m^3
Reynolds Number (Re_τ)	180

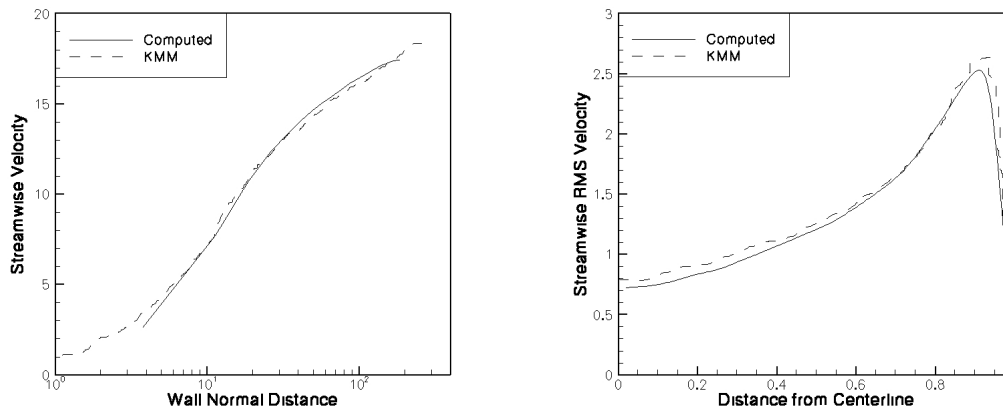


Figure C.1: Mean Streamwise Gas Velocity for the turbulent channel flow case, $Re_\tau = 180$. Figure C.2: Streamwise RMS Velocity for the turbulent channel flow case, $Re_\tau = 180$.

The channel is forced using a constant mass flow rate forcing to maintain a bulk streamwise velocity of $20m/s$. At each time step the body force, which is representing a fictitious pressure gradient, is computed that is needed to achieve this overall bulk velocity, which is directly proportional to the mass flow rate. The flow is ran until it reaches a statistically steady state before statistical data is collected. The determination of when a statistically steady state occurs is based on two features. First the variations in the bulk flow rate become very small, which happens almost immediately. Secondly the wall slip velocity u_τ is also tracked until it reaches its final value for a prolonged period of time.

The first set of figures shows the mean streamwise fluid velocity and the streamwise root mean square velocity. While our simulation is done using large eddy simulation instead of direct numerical simulation, it is shows that the agreement

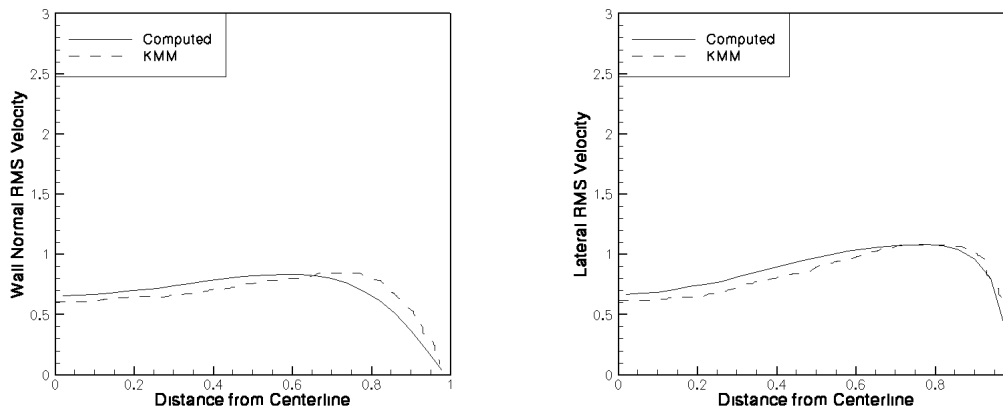


Figure C.3: *Wall Normal RMS Velocity* for Figure C.4: *Lateral RMS Velocity* for the turbulent channel flow case, $Re_\tau = 180$ turbulent channel flow case, $Re_\tau = 180$

is quite good. Most of the perceived error on the graphics is due to the authors inability to trace the validation results concisely.

As with the streamwise root mean square velocities, both the lateral and wall normal rms velocities show good agreement with the provided data. This would seem to indicate that the numerical method given previously can adequately handle the convective terms. This capability of accurately simulating single phase turbulent is key for large eddy simulation to be able to handle particle laden flows as well as oxy-combustion. You may recall that the main reason Reynolds averaged Navier-Stokes models generally fail for particle laden flows within interesting domains is their inability to adequately handle the carrier phase motions, thus leading to physically inaccurate particle motion.

Appendix D – Variation of Reynolds Number

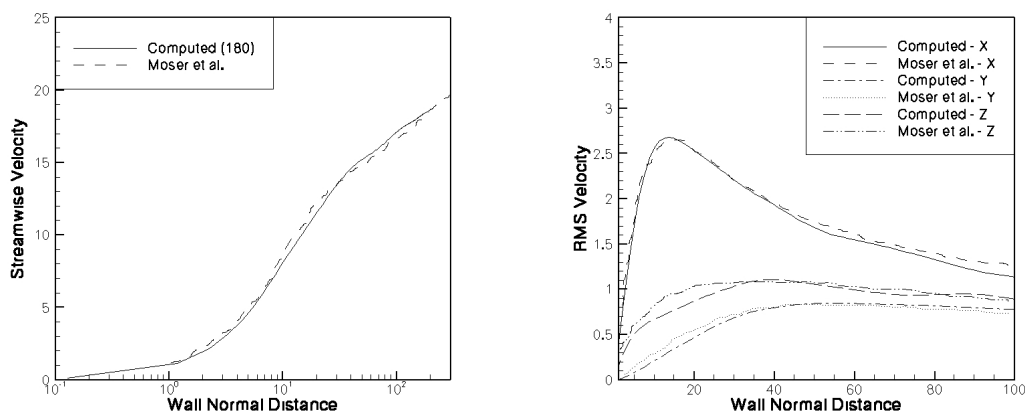


Figure D.1: Mean Streamwise Velocity for the varying Reynolds number case, $Re_\tau = 180$ Figure D.2: Streamwise RMS Velocity for the varying Reynolds number case, $Re_\tau = 180$

Many turbulent flow studies focus on a wall slip Reynolds number of $Re_\tau = 180$. It is important to show that the code is capable of handling higher Reynolds number flows adequately. The fundamental features of turbulent flows can change with Reynolds number, for example how production and dissipation interact and in what quantities. If features such as this are not properly handles inaccurate quantities will be predicted for the turbulent intensity, thus the root-mean-square velocities of the fluid. These cases are interesting because the selection of parameters is somewhat arbitrary as long as the Reynolds number is appropriate. For these studies a viscosity of $\mu = 0.0070303 \text{ kg/ms}$ and a density of $\rho = 1.0$

kg/m^3 were used. A constant pressure gradient forcing is used to enforce the given Reynolds numbers. This is done through a method detailed in the results section in which the pressure gradient needed is supplied as a fictitious body force into each control volume. The needed body force is calculated based on the expected drag at the walls of the channel, this loss must be balanced by the body force. The balance that is struck is the driving force behind the flow rate and flow structure of the domain.

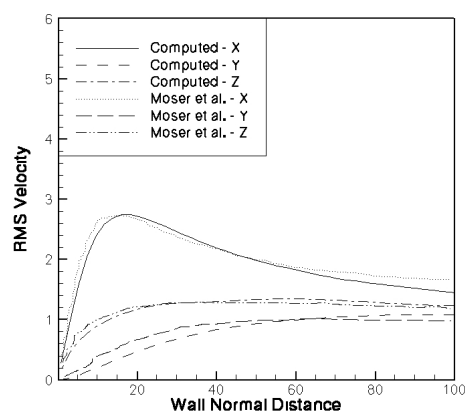
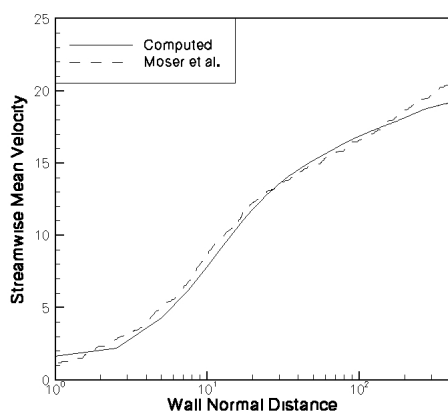


Figure D.3: *Mean Streamwise Velocity* for the varying Reynolds number case, $Re_\tau = 395$

Figure D.4: *Streamwise RMS Velocity* for the varying Reynolds number case, $Re_\tau = 395$

Figures D.1 and D.2 show, similar to the last validation case, that the code can adequately reproduce the features of low Reynolds number turbulence. This is not new. To show that higher Reynolds numbers can be handled we look to the next set of figures. In these figures, D.3 and D.4, we can see that $Re_\tau = 395$ turbulence is handled adequately as well.

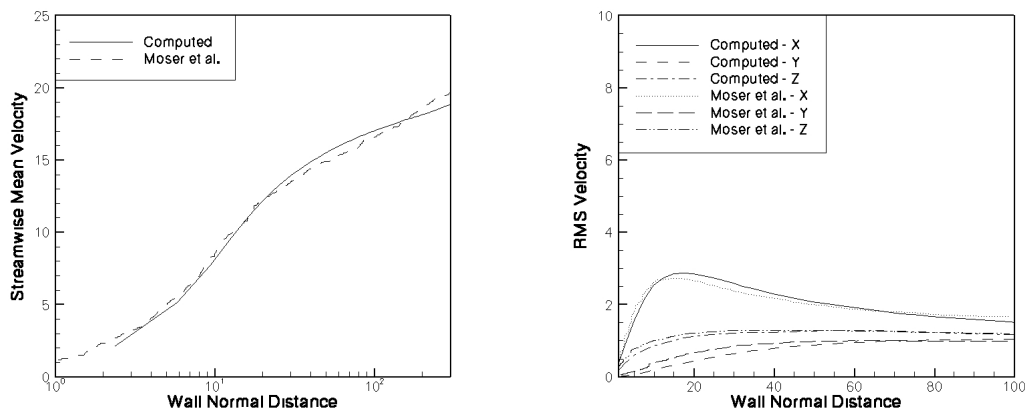


Figure D.5: *Mean Streamwise Velocity* Figure D.6: *Streamwise RMS Velocity*
 for the varying Reynolds number case, for the varying Reynolds number case,
 $Re_\tau = 590$ $Re_\tau = 590$

Lastly we look to figures D.5 and D.6 to demonstrate that the highest Reynolds number turbulence in this study are also handled well. These figures show information for $Re_\tau = 590$. This case is somewhat vital as the turbulent particle-laden channel flow case presented in the results section has a Reynolds number of $Re_\tau = 644$.

Our results seem to agree well with those of Moser et al. (1999) [59]. This is a demonstration that the code scales well with increasing Reynolds number and predicts the proper flow features. The edges and slight jumps in the data are due to the author having trouble ripping the data from the paper with the precision necessary to maintain the smooth curves in the paper.

Appendix E – Crossing Particle Jets

A main case of interest is that of a particle laden jet. Here the inter-particle collision model is validated using a dense particle jet and a dilute particle jet as test cases. This case is examined by Lostec et al. (2008) [58] for various collision models.

Where the Stokes number and Knudsen number are defined as:

$$St = 2\rho_p r_p^2 / 9\mu_f \quad (\text{E.1})$$

$$Kn = 1/4\sqrt{2}ned_p \quad (\text{E.2})$$

In the case of the dilute jet we are expecting to see minimal interaction between the particle jets as both only contain intermittent particles, it would certainly be a stretch to call either a stream. Figure E.1 shows isocontours of particle volume fraction, the contour values themselves are unimportant as the individual particle locations are actually quite clear. Figure E.2 shows a flood contour map of the same features. As was desired we see that there is little to no noticeable variance in the jet path due to the crossing trajectories. This is desirable for obvious reasons, however it was not entirely clear beforehand how well the collision model would perform. The model is designed to handle dense flows, not dilute ones. The inter-

Table E.1: Crossing Particle Jets - Computational Parameters

Parameter	Value
Computational Domain	1 x 1 x 0.2
Stokes Number - Dilute	0.01
Knudsen Number - Dilute	10
Stokes Number - Dense	1.0
Knudsen Number - Dense	0.1
Jet Velocity	1.0 m/s
Jet Width	0.1 m

particle repulsion force applied could have hypothetically derailed the jets even at such a low Knudsen number, however, these worries appear to be unfounded.

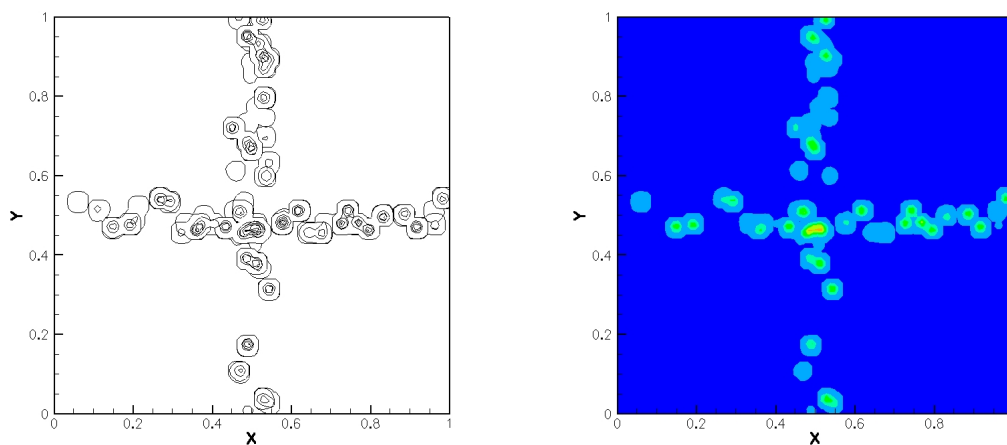


Figure E.1: *Dilute jet case: Particle volume fraction contours* Figure E.2: *Dilute jet case: Particle volume fraction contour flood map*

While its comforting to know that the dilute jet case behaves properly, it is more important that the dense jet behaves properly as the pertinent flows are relatively dense. In this case the set up is the same as before but with a Knudsen

number of 0.1. The desired behavior for this case is that the two jets meet in the middle and form a unified jet.

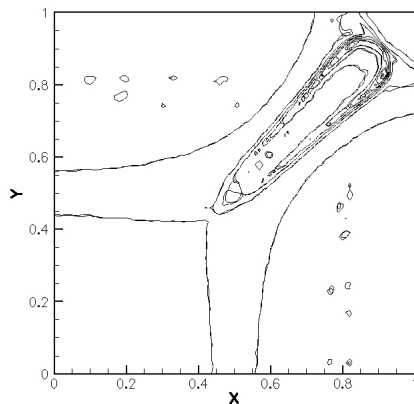


Figure E.3: *Dense jet case: Particle volume fraction contours*

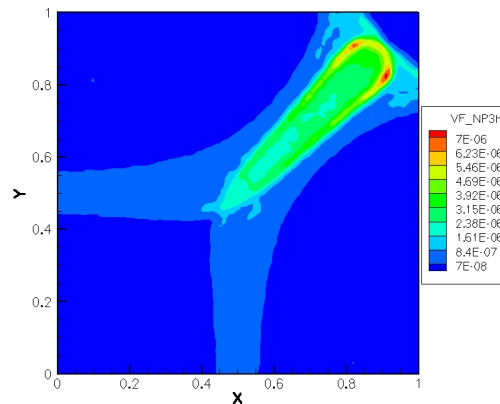


Figure E.4: *Dense jet case: Particle volume fraction contour flood map*

As we can see in both figures E.3 and E.4 the two dense jets have a sufficient concentration that few if any particles escape the crossing, thus all particles are subject to influence from the opposing jet. The mean jet formed slowly expands due to the interparticle repulsion forces and non-uniform collision effects. A few particles stray out of the mean stream when these inter-particle forces become highly unbalanced. Since the particles are injected randomly there will be occasional times and places where the jets aren't quite uniform and cause these lopsided effects.

Bibliography

- [1] Vreman, A.W., 2007, “Turbulence characteristics of particle-laden pipe flow,” *Journal of Fluid Mechanics*, **584**(3&4), pp. 235–279.
- [2] Yamamoto, Y., Potthoff, M., Tanaka, T., Kajishima, T., Tsuji, Y., 2000, “Large-eddy simulation of turbulent gas-particle flow in a vertical channel: effect of considering inter-particle collisions,” *Journal of Fluid Mechanics*, **442**, pp. 303 – 334.
- [3] Lain, S., Sommerfeld, M., 2007, “On Pressure Drop in Horizontal Particle-laden Channel Flow,” *El Hombre y la Maquina*, textbf028, pp. 98 – 107.
- [4] Shirolkar, J.S., Coimbra, C.F.M., Queiroz McQuay, M., 1996, “Fundamental Aspects of Modeling Turbulent Particle Dispersion in Dilute Flows”, *Progress in Energy Combustion Science*, **22**, pp.363–399.
- [5] Sundaresan, S., Eaton, J., Koch, D.L., Ottino, J.L., 2003, “Appendix 2: Report of study group on disperse flow”, *International Journal of Multiphase Flow*, **29**, pp. 1069 – 1087.
- [6] Group Authored , 2006, “Report on Workshop on Multiphase Flow Research”, DOE/NETL-2007/1259 , Morgantown, WV.
- [7] Tsuji, Y., 2007, “Multi-scale modeling of dense phase gas-particle flow,” *Chemical Engineering Science*, **62**, pp. 3410–3418.
- [8] Crowe, C.T., Troutt, T.R., Chung, J.N., 1996, “Numerical Models for Two-Phase Turbulent Flows,” *Annual Review of Fluid Mechanics*, **28**, pp. 11–43.
- [9] Mandli, K.T., 2006, “Multiphase Turbulent Modeling using LES”
- [10] van der Hoef, M.A., van Sint Annland, M., Deen, N.G., Kuipers, J.A.M., 2008, “Numerical Simulation of Dense Gas-Solid Fluidized Beds: A Multiscale Modeling Strategy,” *Annual Review of Fluid Mechanics*, **40**, pp. 47–70.

- [11] Elghobashi, S., 1994, "On Predicting Particle-Laden Turbulent Flows," *Applied Scientific Research*, **52**(3&4), pp. 309–329.
- [12] Elghobashi, S., 1991, "Particle-laden turbulent flows: direct simulation and closure models," *Applied Scientific Research*, **48**, pp. 301–314.
- [13] Pope, S.B., 2004, "Ten Questions concerning the large-eddy simulation of turbulent flows," *New Journal of Physics*, **6**(35), pp. 2–24.
- [14] Patankar, N.A., Joseph, D.D., 2001, "Lagrangian numerical simulation of particulate flows," *International Journal of Multiphase Flow*, **27**, pp. 1685–1706.
- [15] Patankar, N.A., Joseph, D.D., 2001, "Modeling and numerical simulation of particulate flows by the Eulerian-Lagrangian approach," *International Journal of Multiphase Flow*, **27**(10), pp. 1659–1684.
- [16] Prosperetti, A., Zhang, D.Z., 1995, "Finite-Particle-Size Effects in Disperse Two-Phase Flows," *Theoretical and Computational Fluid Dynamics*, **7**(6), pp. 429–440.
- [17] Joseph, D.D., Lundgren, T.S., 1990, "Ensemble Averaged and Mixture Theory Equations for Incompressible Fluid-Particle Suspensions," *International Journal of Multiphase Flow*, **16**(1), pp. 35–42.
- [18] Maxey, M.R., Riley, J.J., 1983, "Equation of motion for a small rigid sphere in a nonuniform flow," *Physics of Fluids*, **26**(4), pp. 883–889.
- [19] Mahesh, K., Constantinescu, G., Moin, P., 2000, "Large-eddy simulation of gas turbine combustors," *Annual Research Briefs, Center for Turbulence Research*, pp. 219-228.
- [20] Apte, S.V., Mahesh, K., Moin, P., Oefelein, J.C., "Large-eddy simulation of swirling particle-laden flows in a coaxial-jet combustor," *International Journal of Multiphase Flow*, **29**, pp. 1311–1331.
- [21] Druzhinin, O.A., Elghobashi, S., 1998, "On the decay rate of isotropic turbulence laden with microparticles," *Physics of Fluids*, **11**(3), pp.602 – 610.
- [22] Yu, Y., Zhou, L., Wang, B., Cai, F., 2005, "A USM- Θ two-phase turbulence model for simulating dense gas-particle flows," *Acta Mechanica Sinica*, **21**, pp. 228-234.

- [23] Rizk, M.A., 1993, "Mathematical Modeling of Densely Loaded, Particle-laden Turbulent Flows," *Atomization and Sprays*, **3**, pp.1 – 27.
- [24] Lun, C.K.K., 2000, "Numerical simulation of dilute turbulent gas-solid flows," *International Journal of Multiphase Flow*, **26**, pp. 1707–1736.
- [25] Zhou, L., Zeng, Z., 2008, "Studies on gas turbulence and particle fluctuation in dense gas-particle flows," *Acta Mechanica Sinica*, **24**, pp.251 – 260.
- [26] Lain, S., Sommerfeld, M., 2003, "Turbulence modulation in dispersed two-phase flow laden with solids from a Lagrangian perspective," *International Journal of Heat and Fluid Flow*, **24**, pp. 616 – 625.
- [27] Wang, Q., Squires, K.D., 1996, "Large eddy simulation of particle-laden turbulent channel flow," *Physics of Fluids*, **8**(5), pp.1207 – 1223.
- [28] Wang, Q., Squires, K.D., 1996, "Large Eddy Simulation of Particle Deposition in a Vertical Turbulent Channel Flow," *International Journal of Multiphase Flow*, **22**(4), pp. 667 – 683.
- [29] Garcia, J., 2001, "Study of the turbulence modulation in particle-laden flows using LES," *Annual Research Briefs, Center for Turbulence Research*, pp. 177 – 184.
- [30] D'Elia, J., Franck, G., Storti, M., Nigro, N., 2004, "Numerical Simulations of a Fully Developed Turbulent Channel Flow by Finite Elements," *Mechanica Computational*, **23**, pp. 2047 – 2064.
- [31] Tang, X., Wu, J., 2007, "An Improved LES on Dense Particle-Liquid Turbulent Flows Using Integrated Boltzmann Equations," *The Canadian Journal of Chemical Engineering*, **85**, pp. 137 – 150.
- [32] Graham, D.I., James, P.W., 1996, "Turbulent Dispersion of Particles Using Eddy Interaction Models," *International Journal of Multiphase Flow*, **22**(1), pp. 157 – 175.
- [33] Uchiyama, T., Fukase, A., 2006, "Vortex simulation of gas-particle two-phase compound round jet," *Powder Technology*, **165**, pp. 83 – 91.

- [34] Deen, N.G., van der Hoef, M.A., van Sint Annaland, M., Kuipers, J.A.M., 2007, "Numerical Simulation of dense gas-particle flows using the Euler-Lagrange approach," *Progress in Computational Fluid Dynamics*, **7**(2-4), pp. 152 – 162.
- [35] Maxey, M.R., Patel, B.K., Chang, E.J., Wang, L.-P., 1997, "Simulations of dispersed turbulent multiphase flow," *Fluid Dynamics Research*, **20**, pp. 143 – 156.
- [36] Kuerten, J.G.M., Vreman, A.W., 2005, "Can Turbophoresis be Predicted by Large-eddy Simulation?," *Physics of Fluids*, **17**, pp.17 – 20.
- [37] Elghobashi, S., 2006, "An Updated Classification Map of Particle-Laden Turbulent Flows," *Proceedings of the IUTAM Symposium on Computational Multiphase Flow*, pp. 3 – 10.
- [38] Armenio, V., Fiorotto, V., 2001, "The importance of forces acting on particles in turbulent flows," *Physics of Fluids*, **13**(8), pp.2437 – 2440.
- [39] Wang, Q., 1997, "On the Role of the Lift Force in Turbulent Simulations of Particle Deposition," *International Journal of Multiphase Flow*, **23**(4), pp. 749 – 763.
- [40] Apte, S.V., Mahesh, K., Lundgren, T., 2008, "Accounting for finite-size effects in simulations of disperse particle-laden flows," *International Journal of Multiphase Flow*, **34**, pp. 260 – 71.
- [41] Squires, K.D., Eaton, J.K., 1990, "Preferential concentration of particles by turbulence," *Physics of Fluids*, **3**(5), pp. 1169 – 1178.
- [42] Ferrante, A., Elghobashi, S., 2003, "On the physical mechanisms of two-way coupling in particle-laden isotropic turbulence," *Physics of Fluids*, **15**(2), pp. 325 – 329.
- [43] Squires, K.D., Simonin, O., 2006, "On Fluid-Particle and Particle-Particle Interactions in Gas-Solid Turbulent Channel Flow," *Proceedings of the IUTAM Symposium on Computational Multiphase Flow*, pp. 11 – 20.
- [44] Limtrakul, S., Chalermwattanatai, A., Unggurawirote, K., Tsuji, Y., Kawaguchi, T., Tanthapanichakoon, W., 2003, "Discrete particle simulation of solids motion in a gas-solid fluidized bed," *Chemical Engineering Science*, **58**, pp. 915 – 921.

- [45] Orme, M., 1997, “Experiments on Droplet Collisions, Bounce, Coalescence and Disruption,” *Progress in Energy Combustion Science*, **23**, pp. 65 – 79.
- [46] Ahmed, A.M., Elghobashi, S., 2000, “On the mechanisms of modifying the structure of turbulent homogenous shear flows by dispersed particles,” *Physics of Fluids*, **12**(11), pp. 2906 – 2930.
- [47] Pope, S.B., 2000, “Turbulent Flows,” Cambridge University Press, The Edinburgh Building, Cambridge, CB2 2RU, UK.
- [48] Moin, P., Squires, K., Cabot, W., Lee, S., 1991, “A dynamic subgrid-scale model for compressible turbulence and scalar transport,” *Physics of Fluids*, **3**(11), pp. 2746 – 2757.
- [49] Germano, M., Piomelli, U., Moin, P., Cabot, W.H., 1991, “A dynamic subgrid-scale eddy viscosity model,” *Physics of Fluids*, **3**(7), pp. 1760 – 1765.
- [50] Armenio, V., Piomelli, U., Fiorroto, V., 1999, “Effect of the subgrid scales on particle motion,” *Physics of Fluids*, **11**(10), pp. 3030 – 3042.
- [51] Darmana, D., Deen, N.G., Kuipers, J.A.M., 2006, “Parallelization of an Euler-Lagrange model using mixed domain decomposition and a mirror domain technique: Application to dispersed gas-liquid two-phase flow,” *Journal of Computational Physics*, **220**, pp. 216 – 248.
- [52] Clift, R., Grace, J.R., Weber, M.E., 1978, “Bubbles, Drop and Particles,” Academic Press.
- [53] Cundall, P.A., Strack, O.D.L., 1979, “A discrete numerical model for granular assemblies,” *Geotechnique*, **29**, pp. 47 – 65.
- [54] Kim, J., Moin, P., 1985, “Application of a fractional step method to incompressible Navier-Stokes equations,” *Journal of Computational Physics*, **59**, pp. 308 – 323.
- [55] Choi, H., Moin, P., 1994, “Effects of computational time step on numerical solutions of turbulent flow,” *Journal of Computational Physics*, **113**, pp. 1 – 4.
- [56] Kim, J., Choi, H., 2000, “A Second-Order Time Accurate Finite Volume Method for Unsteady Incompressible Flow on Hybrid Unstructured Grids,” *Journal of Computational Physics*, **162**, pp. 411 – 428.

- [57] Kim, J., Moin, P., Moser, R., 1987, “Turbulence statistics in fully developed channel flow at low Reynolds number,” *Journal of Fluid Mechanics* **177**, pp. 133 – 166.
- [58] Lostec, N.L., Fox, R.O., Simonin, O., Villedieu, P., 2008, “Numerical description of dilute particle-laden flows by a quadrature-based moment method,” *Annual Research Briefs, Center for Turbulence Research*, pp. 209 – 221.
- [59] Moser, R.D., Kim, J., Mansour, N.N., 1999, “Direct numerical simulation of turbulent channel flow up to $Re_\tau = 590$,” **11**(4), pp. 943 – 945 .
- [60] Yuu, S., Ueno, T., Umekage, T., 2001, “Numerical Simulation of the high Reynolds number slit nozzle gas-particle jet using subgrid-scale coupling large eddy simulation,” *Chemical Engineering Science*, **56**, pp. 4293 – 4307.
- [61] Gutmark, E., Wygnanski, I., 1976, “The planar turbulent jet,” *Journal of Fluid Mechanics*, **73**(3), pp. 465 – 495.
- [62] Gutmark, E., Wolfshtein, M., Wygnanski, I., 1978, “The plane turbulent impinging jet,” *Journal of Fluid Mechanics*, **88**(4), pp. 737 – 756.
- [63] Kulick, J.D., Fessler, J.R., Eaton, J.K., 1994, “Particle response and turbulence modification in fully developed channel flow,” *Journal of Fluid Mechanics*, **277**, pp. 109 – 134.
- [64] Fessler, J.R., Kulick, J.D., Eaton, J.K., 1994, “Preferential concentration of heavy particles in a turbulent channel flow,” *Physics of Fluids*, **6**(11), pp. 3742 – 3749.
- [65] Kurose, R., Makino, H., 2003, “Large eddy simulation of a solid-fuel jet flame,” *Combustion and Flame*, **135**, pp. 1 – 16.
- [66] Baba, Y., Kurose, R., 2008, “Analysis and flamelet modelling for spray combustion,” *Journal of Fluid Mechanics*, **612**, pp. 45 – 79.
- [67] Pozorski, J., Apte, S.V., 2010, “Filtered particle tracking in isotropic turbulence and stochastic modeling of subgrid-scale dispersion,” *In Preparation*.
- [68] Wang, L., Maxey, M.R., 1993 , “Settling velocity and concentration distribution of heavy particles in homogenous isotropic turbulence,” *Journal of Fluid Mechanics*, **textbf256**(27).

- [69] Reade, W.C., Collins, L.R., 2000, "Effect of preferential concentration on turbulent collision rates," *Physics of Fluids*, **12**(10), pp.2530 – 2540.
- [70] Bini, M., Jones, W.P., 2008, "Large-eddy simulation of particle-laden turbulent flows," *Journal of Fluid Mechanics*, **614**, pp. 207 – 252.
- [71] Finn, J., Shams, E., Apte, S.V., 2010, " Modeling and simulation of multiple bubble entrainment and interactions with two-dimensional vortical flows," *Physics of Fluids*, accepted for publication.
- [72] Finn, J., 2010, " A Multiscale Modeling Approach for Bubble-vortex Interactions in Hydro-propulsion Systems, " Oregon State University, M.S. Thesis.
- [73] Sridhar, G., Katz, J., 1999, "Effect of entrained bubbles on the structure of vortex rings, " *Journal of Fluid Mechanics*, **397**, pp. 171 – 202.
- [74] Choi, H.G., Joseph, D.D., 2001, "Fluidization by lift of 300 circular particles in plane Poiseuille flow by direct numerical simulation," *Journal of Fluid Mechanics*, **438**, pp. 101 - 128.
- [75] Shams, E., Apte, S.V., 2007, "Modeling Volumetric Coupling on the Dispersed Phase using the Eulerian-Lagrangian Approach," ILASS Americas 20th Annual Conference on Liquid Atomization and Spray Systems, Chicago, IL, May 2007.

